A Theoretical and Numerical Study of Turbulent Wind–Wave Interaction

A THESIS
SUBMITTED TO THE FACULTY OF THE GRADUATE SCHOOL
OF THE UNIVERSITY OF MINNESOTA
BY

Tao Cao

IN PARTIAL FULFILLMENT OF THE REQUIREMENTS
FOR THE DEGREE OF
DOCTOR OF PHILOSOPHY

Lian Shen, Adviser

December 2020

Acknowledgement

I am always surprised by how fast time can fly! I can still remember the first time I came to UMN six years ago when I was impressed by the quiet environment of campus and beautiful scene of Mississippi river. During my PhD study, I met numerous difficulties and also received a lot of support from others. Without the people around me, this thesis work would not be finished. Here, I express my deep thanks to them.

First I would like to thank especially to my advisor Professor Lian Shen, who has guided me to an interesting research area of fluid mechanics, oceanography. I have learned a lot from him, including finding research topics, doing research, and writing academic papers. Perhaps, the most important thing I learned from my advisor is to be patient and do things of high quality. His enthusiasm, hardworking, and high standard for research have shaped my views of being a scientist.

I am very grateful to the committee members of my preliminary and final exams, Professor Jiarong Hong, Professor Sungyon Lee, and Professor Qi Zhao, for their time and the valuable feedback I received from them, which has inspired me to think more deeply about my research and presentation. I also want to thank my course instructors, Professor Krishnan Mahesh, Professor Joseph W. Nichols, Professor Graham V. Candler, Professor Bernardo Cockburn, and Professor Douglas N. Arnold, for the knowledge I learned from them about fluid mechanics and scientific computing.

During the first two years of my study, I received a lot of help from my labmates, especially Xuanting Hao and Anqing Xuan, who helped me to write programs and introduced the basic knowledge about water waves to me. I am also very lucky to have many friends, who have supported me in a variety of ways when my life was difficult.

At last, I am really indebted to my parents, my girlfriend, Qiaoqiao Lu, and my sister, especially by considering that I have been separated from them for six years. Their sacrifice and support have encouraged me to overcome difficulties in my life and move forward.

Abstract

A deep understanding of turbulent wind–wave interactions is critical for many applications, such as weather modeling in the marine environment, navigation safety of marine vehicles, and offshore wind farm. The present understanding of the fundamental flow dynamics underlying wind–wave interactions is far from enough due to our limited knowledge of turbulence stress in the wind field. However, using the large-eddy simulation (LES) of airflow over water waves and linear analysis, we discover that in certain scenarios, the interactions between turbulent wind and waves can be explained by linear theory without pursuing turbulence stress models. In this thesis, we present two of these scenarios. The first case is the turbulent wind blowing over opposing water waves. We found that the dominant components of opposing wave effects on the overlying airflow exhibit a quasilinear behavior and can be explained by our linear model of wave boundary layer developed in this study, whereas the weak components of opposing wave effects are affected by the turbulence stress. The second case is the turbulent wind following fast-moving water waves, in which the wave phase speed is comparable to or faster than the wind speed. It is discovered that the fast wave effects on the airflow can be entirely explained by our linear models. By further developing split equations for the linear model, we elucidate in detail the physical mechanisms underlying the fast wave effects on the airflow and the wind–wave momentum exchange at the water surface. We believe that our findings can benefit the modeling of turbulent wind–wave interactions in oceanography applications.

Contents

List of Tables

List of Figures

1 Introduction

1.1 Motivations and background

Water waves are ubiquitous on ocean and lake surfaces. After generated by wind, the water wave field can continue to develop through the momentum exchange between the overlying wind and the waves. The presence of water waves can induce significant velocity and pressure perturbations to the airflow, or the wave-induced airflow. The wave-induced airflow can, in turn, cause a force on the water surface and thus a wind–wave momentum exchange. A deep understanding of the wave-induced airflow is the key to the study of turbulent wind–wave interactions, and the resultant predictions of wind and wave fields in the marine environment.

Since the late nineteen fifties, considerable experimental and theoretical studies have been devoted to studying the turbulent wind–wave interactions. The experimental studies (e.g., Shemdin & Hsu, 1967; Hsu *et al.*, 1981; Snyder *et al.*, 1981; Mitsuyasu & Honda, 1982; Plant, 1982; Hsu & Hsu, 1983; Young & Sobey, 1985; Hasselmann & Bsenberg, 1991; Mastenbroek, 1996; Peirson *et al.*, 2003; Donelan *et al.*, 2005; Mitsuyasu & Yoshida, 2005; Donelan *et al.*, 2006; Grare *et al.*, 2013*b*) have been focusing on quantifying the wind–wave momentum exchange. They found that the wind–wave momentum transfer significantly depends on the ratio of wave speed over wind speed and the wave steepness, and this finding forms the basis of the scaling of wave growth rate under various wind–wave conditions. The theoretical studies (e.g., Jacobs, 1987; Van Duin & Janssen, 1992; Belcher & Hunt, 1993; Miles, 1993, 1996; Cohen & Belcher, 1999) were performed to elucidate the fundamental flow dynamics underlying the arising of wave-induced airflow in the wind field and the associated wind–wave momentum exchange. The challenging part of theoretical studies of wave-induced airflow is to model the turbulence stress. The eddy-viscosity and mixing turbulence models have been adopted to model the turbulence stress. Although with these turbulence models, the mechanisms of wave-induced airflow have been understood in a qualitative sense, especially for wind over slow water waves, there still exists a discrepancy in the wave growth rate between theoretical predictions and measurement. More validations of the suitability and accuracy of these turbulence models are needed.

In the recent two decades, with the rising of computer power, high-fidelity simulations, namely LES and direct numerical simulation (DNS), have been playing an increasingly important role in studies of turbulent flows (e.g., Sullivan *et al.*, 2000; Kihara *et al.*, 2007; Yang & Shen, 2010; Druzhinin *et al.*, 2012; Akervik & Vartdal, 2019; Hao & Shen, 2019). LES and DNS solve the first principle of fluid mechanics, namely the Navier-Stokes equations, and can provide 3D detailed descriptions of the turbulent flow field with unprecedented accuracy. With the extensive LES and DNS of turbulent flow over water waves, many important physical processes of the turbulent wind–wave interactions have been revealed. However, the theoretical modeling of the wave-induced airflow has not been improved much, mainly due to the lack of exploration of the turbulence stress models based on high-fidelity simulations. Theoretical analysis in collaboration with high-fidelity simulations is expected to provide valuable insights on the turbulent wind–wave interactions, which is adopted in the present study.

As reviewed above, in most of the previous studies, the turbulence stress is usually taken as an indispensable gradient in the modeling of wave-induced airflow. However, in the present study, we aim to explore the scenarios of wind–wave interactions, in which the wave-induced airflow exhibits a quasilinear behavior and thereby can be theoretically modeled without the pursuit of turbulence models. In other words, the effects of turbulence stress on the wave-induced airflow under these conditions are negligibly small. To identify these scenarios, we need to gain insights from the LES of turbulent airflow over water waves under various wind–wave conditions. Then based on LES data, we derive linear equations of wave boundary layer to describe and explain the observed physical phenomena.

1.2 Thesis overview

In this thesis, we present a study of turbulent wind–wave interactions using high-fidelity simulation and linear analysis. To obtain the turbulent wind field data in the presence of water waves, we adopt LES of airflow over prescribed water waves. Then, the effects of water waves on the airflow are extracted from the LES data. We further derive a set of linear equations to describe the wave effects and thereby elucidate the underlying physical mechanisms. As the turbulent wind–wave interactions can have various conditions, the present study focuses on two typical scenarios, namely the turbulent wind blowing over opposing water waves and the turbulent wind over fast-moving water waves.

In Chapter 2, we investigate the effects of opposing waves on the overlying turbulent wind. The LES results show that opposing waves induce nearly antisymmetric vertical velocity $\widetilde{w}$ in the wind on the two sides of wave crest, while the streamwise velocity $\widetilde{u}$ away from surface and the air pressure $\widetilde{p}$ seem symmetric. To study the mechanisms for the wave-induced airflow, we develop a viscous model by linearising the phase-averaged Navier–Stokes equations in the mapped computational curvilinear coordinate. To illustrate the flow dynamics, we split $\widetilde{w}$ into an antisymmetric component and a symmetric component. The solution of the antisymmetric component of $\widetilde{w}$ from the viscous curvilinear model agrees well with the LES results for different opposing wave conditions. According to the viscous curvilinear model, the large-magnitude antisymmetric component of $\widetilde{w}$ is driven by the wave kinematics at the surface and amplified by the mean shear and viscous stress in the air, and it causes the strong symmetric components of $\widetilde{u}$ and $\widetilde{p}$. In contrast, the small-magnitude symmetric component of $\widetilde{w}$ is forced by the antisymmetric $\widetilde{w}$ through viscous and turbulent stresses near the surface, and it can be described by a further simplified inviscid curvilinear model away from the surface. It is discovered that the weak symmetric $\widetilde{w}$ causes a slight asymmetry in $\widetilde{u}$ and $\widetilde{p}$, and generates a mean wave-coherent stress and the form drag on the wave surface. The wave attenuation rates quantified using the form drag agree with the published experiments.

Chapter 3, we present an explanation of the effects of fast water waves on the overlying turbulent wind. By performing LES of turbulent wind over fast water waves, we observe that the perturbation to wind velocity and pressure by waves, or the wave-induced airflow, is related to the air motion induced by the vertical wave movement. We perform scaling analysis to show that the effects of turbulent stress on the wave-induced airflow are negligibly small. Moreover, we find that the solutions of the non-orthogonal linear model for wave effects on wind developed in Chapter 2 agree well with the LES data. These results demonstrate that the arising of fast wave-induced airflow is a quasilinear process. By developing a new orthogonal linear model, we further show that the behaviour of fast wave effects remains the same using models on different curvilinear coordinates. To elucidate the mechanisms for the wave effects, we split a linear model into two equations corresponding to wave kinematics and forcing by wave elevation, respectively. Using the split equations, we confirm that the vertical component of wave orbital velocity induces a strong airflow perturbation, which produces the dominant components of wave-induced airflow and determines its overall spatial structure. Furthermore, we discover that the weak components of wave-induced airflow are forced by the dominant components via viscous stress and by the forcing induced by wave elevation, and play a central role in the wind–wave momentum exchange through the form drag on the water surface.

Chapter 4 summarizes the major contributions of this thesis and gives potential research topics for future studies. The present linear analysis framework should be extended to more general conditions of wind–wave interactions, including the case in which wind and waves are aligned with an arbitrary angle, the case in which the air density stratification presents, and the scenario where multiple wave components coexist.

2 Wind Blowing Over Opposing Water Waves

2.1 Introduction

The interaction between ocean surface waves and turbulent wind is of significant importance to many applications. Examples range from weather models in marine environments, navigation safety of ocean vehicles, offshore wind energy harvesting, to the forecasting of extreme wind-waves. There is a critical need for a deep understanding of the physical mechanism underlying the turbulent wind–wave interaction, which is currently far from adequate given the complexity of the problem.

In the past few decades, considerable attention has been paid to the scenario of wind and waves in the same direction, which is related to the problem of how the waves are generated by the wind. The effects of the critical layer and wave-induced turbulent stress have been identified and extensively studied. The critical layer, defined as the height at which the mean wind speed equals to the celerity of a wave, drew people's attention and has been shown to be one of the key mechanisms governing the energy flux from the wind to the wave (e.g., Miles, 1957; Lighthill, 1962; Hristov *et al.*, 2003). The wave-induced turbulent stress, defined as the difference between the phase- and ensemble-averaged turbulent stress, has become another research focus later. Some theoretical studies have adopted the eddy viscosity or mixing-length models to relate the wave-induced turbulent stress to the wave-induced velocity (which is the difference between the phase- and ensemble-averaged air velocity) to quantify the contribution of turbulent stress to the energy flux between wind and waves (e.g., Jacobs, 1987; Van Duin & Janssen, 1992; Belcher & Hunt, 1993; Miles, 1993, 1996). Meanwhile, experimental and numerical studies have also examined the structures and effects of wave-induced turbulent stress in the wave boundary layer (e.g., Hsu, Hsu & Street, 1981; Rutgersson & Sullivan, 2005; Kihara *et al.*, 2007; Yousefi & Veron, 2020; Yousefi, Veron & Buckley, 2020). While there still exists discrepancy in the wave growth rate between theoretical predictions and measurements (see the review by Sullivan & McWilliams, 2010), the physical processes in the wind-following-wave case are relatively well understood, at least in a qualitative sense (Belcher & Hunt, 1998).

On the contrary, the scenario of wind blowing oppositely to the waves has received less attention in previous research compared to the wind-following-wave case and is less understood, but is also an important problem. Such scenario can happen in the conditions of hurricanes where the direction of the wind changes rapidly (Wright *et al.*, 2001), storms (Bowers *et al.*, 2000), or even normal wind sea (Ardhuin *et al.*, 2007). Below, we briefly summarize the main findings in the previous studies on wind opposing waves.

There have been a number of measurements of air pressure in laboratory and field to quantify the momentum flux at the air–sea interface, such as Shemdin & Hsu (1967), Snyder *et al.* (1981), Young & Sobey (1985), Banner (1990), Hasselmann & Bsenberg (1991), Donelan *et al.* (2006), and Grare *et al.* (2013*b*), amongst others, which are summarized in detail by Peirson, Garcia & Pells (2003) and Grare *et al.* (2013*b*). Among those studies, Snyder *et al.* (1981) and Hasselmann & Bsenberg (1991) showed that the opposing wave-induced air pressure is nearly anti-phase with the wave elevation in the field conditions. This feature of air pressure induced by opposing waves is also reflected in the laboratory measurement by Young & Sobey (1985) and the numerical simulation using the Reynolds-averaged Navier–Stokes (RANS) equations by Al-Zanaidi & Hui (1984). However, because measurements are usually performed only at several heights above the wave surface, the detailed spatial structures of the opposing wave-induced pressure and velocity have not been fully accessed, with the opposing wave effects on the turbulence statistics studied even less. Therefore, a comprehensive study on the interaction of turbulent wind with opposing waves is called for.

In addition, the physical mechanisms underlying the opposing wave effects on the airflow have not been fully understood. On one hand, it can be inferred from some previous studies that the wave-induced turbulent stress is unimportant for the main feature of wave-induced airflow. For instance, Wen & Mobbs (2015) performed two-dimensional coupled air–water laminar flow simulation for progressive waves opposing wind without considering the turbulence effect, and they obtained a similar phase difference between the wave-induced air velocity and the wave surface as that measured in the turbulent wind by Young & Sobey (1985), implying the dominance of linear dynamics of wave-induced airflow. On the other hand, Young & Sobey (1985) discovered that the linear potential flow theory of Lamb (1932) is inadequate in explaining the opposing wave-induced air motions, especially their magnitude. Note that the potential flow theory of Lamb (1932) neglects the viscous stress, the mean wind shear, and the elevation of the wave surface. A more sophisticated model with these effects incorporated is critically needed, which is developed in the present study.

Moreover, there exist different opinions among previous studies on the wave attenuation rate for the opposing waves and the underlying mechanisms. In their field studies, Snyder *et al.* (1981) and Hasselmann & Bsenberg (1991) measured the correlation between the air pressure and wave slope, and showed that the wave attenuation rate is very small. However, the laboratory measurement of the pressure-slope correlation by Donelan (1999) showed that the air pressure can induce appreciable wave attenuation, and this result is also reflected in the numerical simulations using the RANS equations (e.g., Al-Zanaidi & Hui, 1984; Mastenbroek, 1996; Harris *et al.*, 1995; Cohen, 1997). Based on the measured air velocity and pressure above opposing waves in the laboratory, Young & Sobey (1985) proposed another mechanism for the wave attenuation based on the self correlation of the wave-induced streamwise velocity, which was however contradicted by Hasselmann & Bsenberg (1991).

As pointed out by Peirson *et al.* (2003), the pressure-slope correlation at the wave surface is difficult to measure directly and is usually extrapolated from the measurement above the surface, which might be affected by the complex airflow behaviour very close to the surface. For example, Grare *et al.* (2013*b*) performed a thorough measurement of the pressure-slope correlation above the wave surface and found that its vertical gradient has a significant change near the surface. With this factor considered, Peirson *et al.* (2003) performed measurement of the evolution of surface waves, which showed higher wave attenuation rate for the waves opposing the wind direction than the previous experimental and numerical studies. Mitsuyasu & Yoshida (2005) also directly measured the evolution of waves opposing the wind direction and obtained a wave attenuation rate smaller than Peirson *et al.* (2003). Mitsuyasu & Yoshida (2005) stated that more data on the wind-induced current in the wind-wave tank are needed to examine the discrepancy of the wave decay rate due to wave–current interaction between these two studies.

Based on the review above, the present study aims to study the opposing wave-induced airflow velocity, pressure, and turbulence statistics. The focus of our study is the physical mechanisms underlying the wave-induced airflow, especially the effects

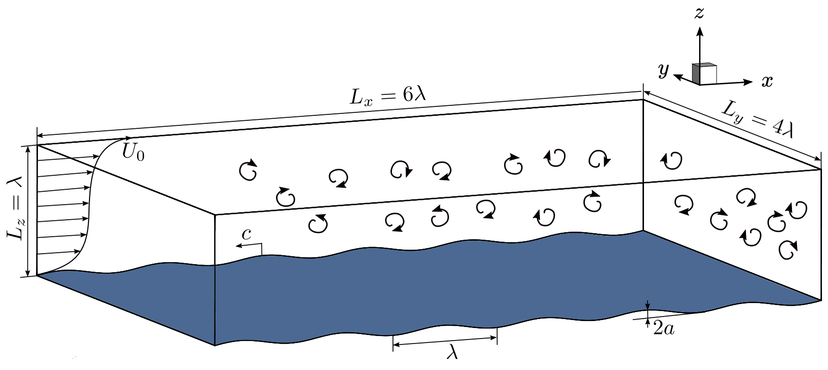

Figure 1: Sketch of the computational configuration of LES of wind opposing water wave. The turbulent wind field is driven by a constant velocity U_0 at the top of the computational domain, with the Dirichlet boundary condition applied at the wave surface and periodic boundary condition applied in the horizontal directions. The surface wave propagates in $-x$ direction, with a wavelength λ, an amplitude a, and a phase speed c.

of the nonlinear forcing, e.g. the turbulent stress, and the linear forcing, e.g. the viscous stress. We also aim to examine the relationship between the wave-induced airflow and wind–wave momentum flux, and quantify the resulting wave attenuation rate.

In this study, we carry out wall-resolved large-eddy simulation (LES) of the turbulent wind field with the surface wave propagating in the opposite direction of the wind as sketched in figure 1. In the recent two decades, because of their high fidelity, direct numerical simulation (DNS) and LES have been playing an increasingly important role in the study of turbulent wind–wave interaction (e.g., Sullivan *et al.*, 2000; Sullivan *et al.*, 2008; Yang & Shen, 2009; Yang & Shen, 2010; Druzhinin, Troitskaya & Zilitinkevich, 2012, 2016; Jiang *et al.*, 2016; Yang & Shen, 2017; Akervik & Vartdal, 2019; Hao & Shen, 2019; Wang *et al.*, 2020). The advantage of the wall-resolved LES is that it allows for a Reynolds number higher than the DNS, but still resolves viscous sublayer near the wave surface, without the parameterizations of surface roughness and surface stress (Pope, 2000). From the wall-resolved LES, the three dimensional turbulent wind field in the presence of the opposing water waves is obtained, and the wave-induced air motions are extracted and examined. To explain the arising of the wave-induced airflow, we also perform a theoretical analysis of the linearised viscous momentum equation for the wave-induced air motions in a mapped computational curvilinear coordinate in the presence of wind shear, for the first time.

The remainder of § 2 is organized as follows. The configuration of simulation and the methodology for the statistical analysis are shown in § 2.2. The features of the wave-coherent airflow are illustrated in § 2.3. The derivation of the viscous linearised equation is provided in § 2.4, and the physical mechanisms underlying the wave-induced airflow are discussed in § 2.5. In § 2.6, we perform a comparison of the wave attenuation rate between the present study and the previous studies. At last, conclusions and discussion are given in § 2.7.

2.2 Configuration of simulation and methodology for data analysis

2.2.1 Configuration of simulation

To solve for the turbulent wind field following or opposing waves, we perform LES of wind turbulence over waves. The filtered Navier–Stokes (NS) equations for the air motions are given as

$$
\begin{aligned}
\frac{\partial u_j}{\partial x_j} &= 0, && (1)\\
\frac{\partial u_j}{\partial t} + u_m \frac{\partial u_j}{\partial x_m} &= -\frac{1}{\rho_a}\frac{\partial p}{\partial x_j} - \frac{\partial \tau^d_{jm}}{\partial x_m} + \nu \frac{\partial^2 u_j}{\partial x_m \partial x_m}, && (2)
\end{aligned}
$$

where x, y, and z denote the coordinates (figure 1) in the streamwise, spanwise, and vertical directions, respectively, $u_j (j = 1, 2, 3) = (u, v, w)$ is the filtered velocity in LES at the grid scale, p is the filtered modified pressure, τ^d_{jm} is the trace-free part of the subgrid-scale (SGS) stress tensor, ρ_a is the density of air, and ν is the kinematic viscosity of air.

The progressive waves are imposed as a Dirichlet boundary condition for the air velocity at the water surface, $u_i(z = \eta) = (u_s, v_s, w_s)$, where η is the surface wave elevation and (u_s, v_s, w_s) is the orbital velocity of the wave at the surface, given as

$$
\begin{aligned}
\eta(x, y, z, t) &= a \sin k(x - ct), && (3)\\
u_s(x, y, z, t) &= akc \sin k(x - ct), && (4)\\
v_s(x, y, z, t) &= 0, && (5)\\
w_s(x, y, z, t) &= -akc \cos k(x - ct), && (6)
\end{aligned}
$$

where a is the amplitude of the surface wave, $k = 2\pi/\lambda$ is the wavenumber, λ is the wavelength, and c is the phase speed. Here, an Airy wave solution is adopted. In the case of a Stokes wave, the effect of nonlinearity by the higher harmonics is of $O((ak)^2)$. In our derivation and analysis of the linearised equations in the following sections, the $O((ak)^2)$ terms in the governing equations are neglected. Therefore, we only consider the dominant Fourier component in the water wave solution to be consistent.

To accurately capture the effects of the surface wave geometry and motions on the turbulent wind field, the LES solver utilizes a boundary-fitted grid that follows the instantaneous wave surface at each time step. For discretizing the governing equations, we transform the irregular physical domain (x, y, z, t) above the wave to a rectangular computational domain (ξ, ψ, ζ, τ) using the following algebraic mapping,

$$\tau = t, \qquad \xi = x, \qquad \psi = y, \qquad \zeta = z + g(\zeta)\eta, \qquad \text{where } g(\zeta) = \frac{\zeta}{H} - 1. \tag{7}$$

Here, H is the mean physical domain height and $g(\zeta)$ denotes the transformation function. We use the index notation to denote the physical and computational coordinates as $x_j (j = 1, 2, 3) = (x, y, z)$ and $\xi_j (j = 1, 2, 3) = (\xi, \psi, \zeta)$, respectively. The Jacobian matrix corresponding to the above transformation is

$$\boldsymbol{J} = \begin{bmatrix} \dfrac{\partial \xi}{\partial x} & \dfrac{\partial \xi}{\partial y} & \dfrac{\partial \xi}{\partial z} \\ \dfrac{\partial \psi}{\partial x} & \dfrac{\partial \psi}{\partial y} & \dfrac{\partial \psi}{\partial z} \\ \dfrac{\partial \zeta}{\partial x} & \dfrac{\partial \zeta}{\partial y} & \dfrac{\partial \zeta}{\partial z} \end{bmatrix} = \begin{bmatrix} 1 & 0 & 0 \\ 0 & 1 & 0 \\ \dfrac{g\eta_\xi}{1 - g_\zeta \eta} & \dfrac{g\eta_\psi}{1 - g_\zeta \eta} & \dfrac{1}{1 - g_\zeta \eta} \end{bmatrix}, \tag{8}$$

where $g_\zeta = \mathrm{d}g/\mathrm{d}\zeta$. Because of the surface wave motions, the transformation (7) varies with time, resulting in a transformation of time derivative between the computational space and the physical space

$$\frac{\partial}{\partial t}=\frac{\partial}{\partial \tau}+\frac{\partial \xi_j}{\partial t}\frac{\partial}{\partial \xi_j}=\frac{\partial}{\partial \tau}+\frac{\partial \zeta}{\partial t}\frac{\partial}{\partial \zeta}, \quad \text{where } \frac{\partial \zeta}{\partial t}=\frac{g\eta_\tau}{1-g_\zeta \eta}. \tag{9}$$

The transformed LES equations in the computational space read

$$\begin{aligned} J_{pj}\frac{\partial u_j}{\partial \xi_p} &= 0, &(10)\\ \frac{\partial u_j}{\partial \tau}+\delta_{p3}\frac{\partial \zeta}{\partial t}\frac{\partial u_j}{\partial \xi_p}+J_{lp}\frac{\partial (u_j u_p)}{\partial \xi_l} &= -\frac{J_{lj}}{\rho_a}\frac{\partial p}{\partial \xi_l}+J_{lp}\frac{\partial \tau^d_{jp}}{\partial \xi_l}+\nu J_{np}\frac{\partial}{\partial \xi_n}\Big(J_{lp}\frac{\partial u_j}{\partial \xi_l}\Big), &(11) \end{aligned}$$

where J_{lp} is the (l,p) entry of the mapping matrix $\boldsymbol{J}$ and δ_{lp} is the Kronecker delta.

Equations (10) and (11) are discretized and solved in the rectangular computational space. A Fourier-series-based pseudo-spectral method is used for the (ξ,ψ) plane discretization with evenly spaced grid points in both directions. A second-order finite difference method is employed for the discretization in the ζ direction with grid points clustered near the upper and lower boundaries. For the filtering operators in the LES, a two-dimensional spectral cutoff filter in the (ξ,ψ) plane is adopted. In the momentum equation, the SGS stress tensor is calculated using the dynamic Smagorinsky model (Smagorinsky, 1963; Germano *et al.*, 1991; Lilly, 1992). To integrate the momentum equations in time, we use a fractional-step method. First, the advection and viscous terms are advanced in time with the second-order Adam–Bashforth scheme. Second, a non-linear Poisson equation is solved using iteration to obtain the pressure field, which is used to correct the velocity field such that the continuity equation is satisfied. The detailed numerical procedure and the validation of our numerical method can be found in Yang & Shen (2011a). The present LES solver simulates the system in a time-dependent domain. The solver was developed for turbulent airflows over complex wave field (Yang & Shen, 2011*a*,*b*). The conservation of momentum is examined in appendix A. The present solver has been extensively utilized to study turbulent wind field in the presence of monochromatic water waves (Yang & Shen, 2009, 2010, 2017) and broadband water wave fields (Yang, Meneveau & Shen, 2013, 2014*a*,*b*; Hao & Shen, 2019), with extensive validations performed in the references cited above. We note that for monochromatic waves, it is also feasible to perform the simulation in the frame travelling with the wave, where the domain geometry does not change in time (e.g., Sullivan *et al.*, 2000; Druzhinin *et al.*, 2012).

As sketched in figure 1, the turbulent wind is driven by a fixed velocity at the top of the simulation domain: $(u,\ v,\ w)$=$(U_0,\ 0,\ 0)$, and periodic boundary condition is applied in the horizontal directions on the lateral boundaries. This canonical setup has been extensively used in the previous simulations of turbulent air flows over surface waves (e.g., Sullivan *et al.*, 2000; Druzhinin *et al.*, 2012, 2016). In the present study, the wave age c/U_0 of the waves varies between -0.8 and 0.1. Two wave steepness values are considered, $ak = 0.08$ and 0.15 (table 1). Here, a negative wave age denotes the surface wave propagating against the wind direction, while a positive wave age denotes the following-wind surface wave. The wave steepness in the present study is comparable to the typical values adopted in the previous studies of wind opposing waves, e.g. $ak = 0.06-0.19$ in Peirson *et al.* (2003) and $ak \approx 0.06-0.13$ in Mitsuyasu & Yoshida (2005). The Reynolds number based on the wavelength of the surface wave and the driving velocity at the top, $U_0\lambda/\nu$, is 30 000, which is higher than the previous DNS of wind over water waves, e.g., 8 800 in Sullivan *et al.* (2000), 10 000 in Yang & Shen (2010), and 15 000 in Druzhinin *et al.* (2012), but is one to two orders of

Case	c/U_0	Direction	ak	$u_\tau \times 10^2$	$u_\tau \lambda/\nu$	$\left(\Delta\xi^+, \Delta\psi^+, \Delta\zeta^+_{\min}\right)$
WFW01	0.1	Following	0.15	2.89	867	$(20.32, 13.55, 0.18)$
WOW01	-0.1	Opposing	0.15	2.77	831	$(19.48, 12.98, 0.17)$
WOW01L	-0.1	Opposing	0.08	2.67	802	$(18.79, 12.52, 0.16)$
SWOW01L	-0.1	Opposing	0.08	2.67	802	$(14.09, 9.39, 0.12)$
WOW015L	-0.15	Opposing	0.08	2.66	797	$(18.68, 12.45, 0.16)$
WOW02L	-0.2	Opposing	0.08	2.63	790	$(18.52, 12.34, 0.16)$
WOW03L	-0.3	Opposing	0.08	2.68	803	$(18.82, 12.55, 0.16)$
WOW04	-0.4	Opposing	0.15	2.83	849	$(19.90, 13.27, 0.17)$
WOW04L	-0.4	Opposing	0.08	2.56	767	$(17.98, 11.98, 0.15)$
WOW08	-0.8	Opposing	0.15	2.98	893	$(20.93, 13.95, 0.18)$
WOW08L	-0.8	Opposing	0.08	2.60	781	$(18.31, 12.21, 0.15)$

Table 1: List of LES cases for turbulent wind opposing and following progressive water waves. In the table, WFW stands for wind following wave, and WOW for wind opposing wave. The bulk Reynolds number $U_0\lambda/\nu$ is prescribed as 30 000 for all the wave cases, while $u_\tau\lambda/\nu$ and the grid resolution are quantified *a posterior*. In case SWOW01L, the wind field is discretized with $(N_x, N_y, N_z) = (512, 512, 257)$ grid points in the (ξ, ψ, ζ) directions, respectively, while in all of the other cases in the table, $(N_x, N_y, N_z) = (384, 384, 193)$.

magnitude lower than the laboratory studies of wind opposing waves (Young & Sobey, 1985; Peirson *et al.*, 2003; Mitsuyasu & Yoshida, 2005) as limited by the computation cost of the wall-resolved LES. However, as reviewed by Sullivan & McWilliams (2010), despite the lower Reynolds number, DNS and LES are capable of revealing many key physical processes in the turbulent wind–wave interaction. The corresponding Reynolds number based on the friction velocity $u_\tau\lambda/\nu$ varies slightly from case to case, but is around 800 for all cases as summarized in table 1. Here, u_τ is defined as the friction velocity $u_\tau = \sqrt{\tau_s/\rho_a}$, where τ_s is the mean viscous shear stress at the top of the simulation domain, which equals to the mean total stress at any given height in the wave surface layer and the summation of viscous shear stress and form drag at the wave surface.

To fully capture the wave-coherent motions in the wind field, a simulation domain of the size $(L_x, L_y, H) = (6\lambda, 4\lambda, \lambda)$ is adopted. The same domain size has been employed in the previous studies (e.g., Sullivan *et al.*, 2000; Druzhinin *et al.*, 2012, 2016). The turbulent flow field is discretized in the computational space with $384^2 \times 192$ grid points, providing a resolution of $\Delta\xi^+ \simeq 21$, $\Delta\psi^+ \simeq 14$, and $\Delta\zeta^+_{\mathrm{min}} \simeq 0.2$, where $\Delta\zeta^+_{\mathrm{min}}$ denotes the minimum grid space near the boundary in the ζ direction. The superscript '+' indicates normalisation by the viscous length scale ν/u_τ. The grid resolution is sufficient for wall-resolved LES according to the criterion given in Choi & Moin (2012), and we have confirmed the grid convergence with tests described in appendix B. The parameters and resolution of the wave cases considered in this study are summarized in table 1.

For data sampling, the simulations of all cases evolve for approximately 120 times of the largest eddy turn-over time, i.e. $120H/u_\tau$. Snapshots of three dimensional instantaneous velocity field were output every $0.17H/u_\tau$, corresponding to 150 viscous time units, i.e. $150\nu/u_\tau^2$, with a total number of 200 snapshots for the statistical analysis in this study.

2.2.2 Methodology for data analysis

To extract the effects of the progressive water waves on the overlying turbulent wind field, we apply a triple decomposition to the instantaneous flow field (Hussain & Reynolds, 1970)

$$f(x,y,z,t) = \overline{f}(\xi,\zeta) + f'(x,y,z,t) = \langle f\rangle(\zeta) + \widetilde{f}(\xi,\zeta) + f'(x,y,z,t), \tag{12}$$

where f denotes an arbitrary physical quantity in the wind field, $\overline{f}$ is its phase-averaged part, $\langle f\rangle$ is its mean value, which is obtained through the average in time and over the (ξ,ψ) plane, $\widetilde{f}$ is its wave-induced fluctuation, and f' is its turbulent fluctuation. The phase-averaged quantify $\overline{f}$ is calculated using the snapshots of the turbulent flow field with two steps: first, because the wave phase is known at each time step from the prescribed surface elevation information (3) with $k(\xi - ct)$ quantified, each instantaneous flow field is averaged along the spanwise direction and then shifted to the same phase with respect to the surface wave; then an ensemble average of the shifted velocity fields is performed

$$\overline{f}(\xi,\zeta) = \frac{1}{N_t}\frac{1}{N_y}\sum_{p=1}^{N_t}\sum_{m=1}^{N_y} f(\xi(l) - ct(p), \psi(m), \zeta(n)), \tag{13}$$

where the indices l, m, n, p denote the discrete points in ξ, ψ, ζ, and t, respectively, and N_t and N_y are the total number of the snapshots employed and the number of the grid points in the spanwise direction, respectively. Then the turbulent fluctuation is calculated by subtracting the phase-averaged part from the instantaneous part, i.e. $f'(x, y, z, t) = f(x, y, z, t) - \overline{f}(\xi, \zeta)$, and the wave-induced part is obtained by subtracting the mean value from the phase-averaged quantity, i.e. $\widetilde{f}(\xi, \zeta) = \overline{f}(\xi, \zeta) - \langle f\rangle(\zeta)$.

In (12), $\widetilde{f}$ is the Cartesian wave-coherent quantity, with the physical coordinate (x, y, z) transformed to the mapped curvilinear coordinate (ξ, ψ, ζ). Although performing average in the (x, y, z) coordinate has the advantage of being independent of the mapped computational curvilinear grid, $\widetilde{f}$ is not defined for all of the region below the wave crest and above the wave trough. Moreover, for theoretical analysis, because the boundary conditions imposed by the wave elevation and kinematics for the airflow are applied on a curved surface, it is challenging to derive the boundary conditions for $\widetilde{f}$ in the (x, y, z) coordinate. Therefore, many previous experimental, numerical, and theoretical studies conducted averaging in the mapped curvilinear coordinates (e.g., Hsu *et al.*, 1981; Hsu & Hsu, 1983; Belcher & Hunt, 1993; Sullivan *et al.*, 2000; Yang & Shen, 2010; Hara & Sullivan, 2015; Buckley & Veron, 2016; Akervik & Vartdal, 2019). Using the various forms of mapped coordinates employed in previous studies, the underlying physical mechanisms revealed are the same (see, e.g., Yang & Shen, 2010; Hara & Sullivan, 2015).

Previous studies showed that $\widetilde{f}$ is dominated by its fundamental mode, i.e. the Fourier coefficient $\widehat{f}$ corresponding to the wavenumber k (Hussain & Reynolds, 1970),

$$\widetilde{f} = \widehat{f}\mathrm{e}^{\mathrm{i}k\xi} + \widehat{f}^{*}\mathrm{e}^{-\mathrm{i}k\xi} + \text{harmonics}, \tag{14}$$

where $\widehat{f}^*$ is the complex conjugate of $\widehat{f}$. The phase difference between $\widetilde{f}$ and $\widetilde{\eta}$ is quantified according to

$$\widetilde{f} = 2\,\mathrm{Re}\left[\widehat{f}\right]\cos(k\xi) - 2\,\mathrm{Im}\left[\widehat{f}\right]\sin(k\xi) = 2|\widehat{f}|\sin\Big(k\xi - \phi_{\widetilde{f}\widetilde{\eta}}\Big) + \text{harmonics}. \qquad (15)$$

Here, '$|\cdot|$' is the modulus operator for complex numbers and $\phi_{\widetilde{f}\widetilde{\eta}} = \arctan\Big(\mathrm{Re}[\widehat{f}]/\,\mathrm{Im}[\widehat{f}]\Big)$ is the phase difference from the wave surface $\widetilde{\eta} = a\sin(k\xi)$. For the analyses in §§ 2.4 and 2.5, we focus on the fundamental mode of the wave-induced quantity, following the previous studies (e.g., Miles, 1957; Hsu *et al.*, 1981; Hsu & Hsu, 1983; Belcher & Hunt, 1993; Kihara *et al.*, 2007). The real and imaginary parts of $\widehat{f}$ have different spatial structures and different physical meanings. Specifically, $\mathrm{Re}[\widehat{f}]$ corresponds to a cosinusoidal perturbation, which is $\pi/2$ out-of-phase with the wave surface, while $\mathrm{Im}[\widehat{f}]$ corresponds to a sinusoidal perturbation, which is in-phase with the wave surface. In other words, $\mathrm{Re}[\widehat{f}]$ is antisymmetric about the surface wave crest, while $\mathrm{Im}[\widehat{f}]$ has a symmetric spatial distribution.

It is noted that the phase average is adopted to extract the wave-induced quantity $\widetilde{f}$ in the triple decomposition (12), which has been widely employed in studies where the effects of a monochromatic wave or the dominant wave component of the wind waves are considered (e.g., Hsu *et al.*, 1981; Hsu & Hsu, 1983; Sullivan *et al.*, 2000; Kihara *et al.*, 2007; Yang & Shen, 2010; Druzhinin *et al.*, 2012; Hara & Sullivan, 2015; Buckley & Veron, 2016; Yang & Shen, 2017; Akervik & Vartdal, 2019). The wave-coherent quantity can also be identified through the correlation with the wave elevation (Hristov, Friehe & Miller, 1998; Hristov & Ruiz-Plancarte, 2014) or through the spectral method (Grare, Lenain & Melville, 2013*a*, 2018). For the monochromatic wave form considered in the present study, the difference among these methods is small as wave-induced quantity is dominated by the fundamental mode. However, the latter two methods have the advantage of being able to extract the wave-coherent quantity above a broadband wave field.

In the following sections, we first show the opposing wave effects on the velocity, pressure, and turbulence statistics in the airflow (§ 2.3). In § 2.4, we present a physical model to explain the opposing wave-induced airflow. The underlying physical mechanisms and the wave attenuation rate are examined in §§ 2.5 and 2.6, respectively. We note that in §§ 2.3 and 2.5, we focus on four representative wave cases in table 1, namely WFW01 ($c/U_0 = 0.1$, $ak = 0.15$), WOW01 ($c/U_0 = -0.1$, $ak = 0.15$), WOW01L ($c/U_0 = -0.1$, $ak = 0.08$), and WOW04 ($c/U_0 = -0.4$, $ak = 0.15$), to show the effects of wave propagation direction, wave steepness, and wave speed. The other wave cases have consistent results as the four wave cases and thus are not presented in these two sections for space and clarity consideration. In § 2.6, we present the wave attenuation rates in all of the wave cases listed in table 1 to compare with previous studies.

2.3 Features of opposing wave effects in the airflow

In this section, we show the wave-coherent velocity (§ 2.3.1), wave-coherent stress $-\widetilde{u}\widetilde{w}$ and pressure $\widetilde{p}$ (§ 2.3.2), and wave-coherent turbulence variance $\widetilde{u'u'} + \widetilde{w'w'}$ and turbulent stress $-\widetilde{u'w'}$ (§ 2.3.3) in the wall-resolved LES. Here, we note that in the expressions of the wave-coherent stress and turbulent stress used here, the constant air density is omitted.

2.3.1 Wave-induced velocity

The propagation of a surface wave can induce velocity perturbation in the airflow travelling at the same speed as the surface wave celerity, which is usually referred to as the 'wave-coherent' or 'wave-induced' velocity in the literature. For a plane progressive gravity wave, the wave-induced velocity also exhibits a two-dimensional pattern. In the instantaneous fields, the perturbations by the wave are more pronounced in the vertical velocity than in the streamwise velocity owing to the mean shear in the latter. Therefore, we use the instantaneous vertical velocity to illustrate the effects of water waves. Figure 2 shows snapshots of the vertical velocity for the four wave conditions: WFW01, WOW01, WOW01L, and WOW04 (table 1). For the same wave speed, both the following wave case WFW01 (figure 2a) and the opposing wave case WOW01 (figure 2b) display a structure of alternating positive and negative vertical velocity w, which corresponds to upward and downward airflow along the wave crest, respectively, with the magnitude in the opposing wave case being slightly larger especially near the wave surface. The strength of this flow structure varies with wave steepness and speed. Compared with case WOW01 (figure 2b), the velocity perturbation becomes weaker for a less steep opposing wave in case WOW01L (figure 2c), while it is strengthened for a faster opposing wave in case WOW04 (figure 2d).

To show the statistical results of the structure of the upward and downward wave-coherent airflows, we present the wave-induced vertical velocity $\widetilde{w}$ in figure 3. It is noted that in figure 3, the contours are plotted up to $z/\lambda = 0.4$, because the magnitudes of wave-induced quantities are small above this height, which is also the case for the other figures in §§ 2.3 and 2.5. In general, the opposing wave cases (figure 3b–d) show a positive $\widetilde{w}$ at the windward face and a negative $\widetilde{w}$ at the leeward side with a

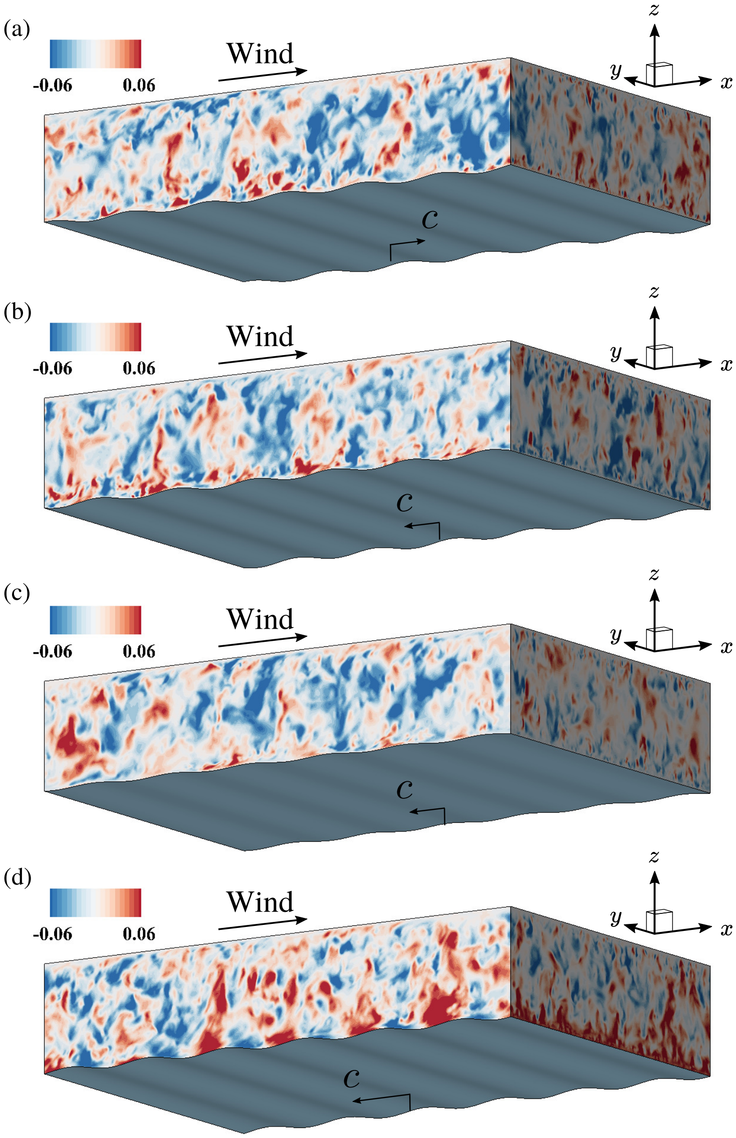

Figure 2: Instantaneous field of the vertical velocity w, normalised by the top-driven velocity U_0, for the simulation cases: (a) WFW01, $c/U_0 = 0.1$, $ak = 0.15$; (b) WOW01, $c/U_0 = -0.1$, $ak = 0.15$; (c) WOW01L, $c/U_0 = -0.1$, $ak = 0.08$; (d) WOW04, $c/U_0 = -0.4$, $ak = 0.15$. For positive wave age, the surface wave travels in the $+x$ direction, while for negative wave age, the surface wave travels in the $-x$ direction. The wind is along with the $+x$ direction in all cases.

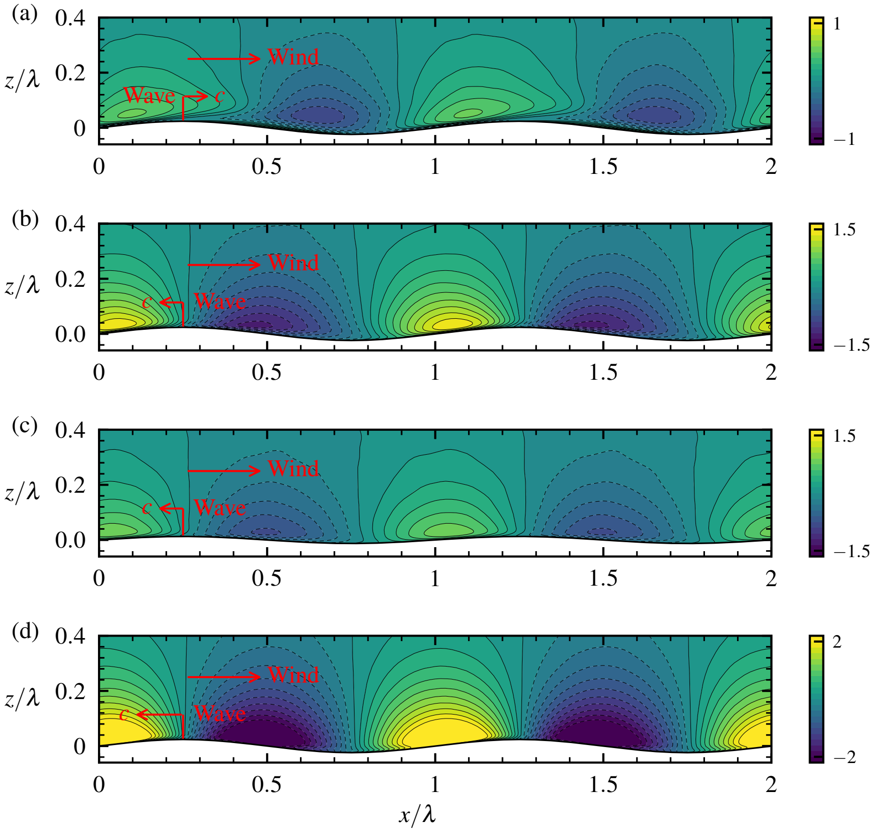

Figure 3: Spatial distribution of the wave-induced vertical velocity $\widetilde{w}$ for the wave conditions: (a) WFW01, $c/U_0 = 0.1$, $ak = 0.15$; (b) WOW01, $c/U_0 = -0.1$, $ak = 0.15$; (c) WOW01L, $c/U_0 = -0.1$, $ak = 0.08$; (d) WOW04, $c/U_0 = -0.4$, $ak = 0.15$. The results are normalised by u_τ.

nearly antisymmetric structure throughout the wave boundary layer, indicating that its phase difference from the wave profile $\widetilde{\eta}$ is roughly $\pi/2$. In the following wave case (figure 3a), although $\widetilde{w}$ is positive at the windward face and negative at the leeward face as in the opposing wave cases, it does not display antisymmetry. Near the wave surface, $\widetilde{w}$ is tilted because of the effect of wave orbital velocity at the surface, which induces a negative $\widetilde{w}$ at the windward side below the critical height (which is comparable to the viscous sublayer thickness in case WFW01 which has $c/u_\tau < 5$). Hence the region corresponding to negative $\widetilde{w}$ transits sharply from the windward face to the leeward face across the critical height, resulting in the tilting of $\widetilde{w}$ near the wave surface. As the Reynolds number increases, the viscous sublayer becomes thinner compared to the wavelength and correspondingly the transition of $\widetilde{w}$ occurs in an thinner region in the airflow, which causes the tilting of $\widetilde{w}$ to be less obvious as shown in the case $(c/u_\tau,\ ak) = (3.7,\ 0.13)$ in Buckley & Veron (2016). This phenomenon does not happen in the opposing wave cases, as the pattern of $\widetilde{w}$ induced by the wave kinematics at the wave surface is the same as the behaviour of $\widetilde{w}$ away from the wave surface. Also is shown in figure 3 is that, not only the spatial structure but also the magnitude of $\widetilde{w}$ is affected by the wave conditions. A comparison of the magnitude of $\widetilde{w}$ between cases WFW01 (figure 3a) and WOW01 (figure 3b) shows that the wave propagating against the wind induces stronger $\widetilde{w}$ than that induced by the wave following the wind. Additionally, compared with case WOW01, a less steep opposing wave causes a weaker $\widetilde{w}$ (figure 3c), while a faster opposing wave results in a larger magnitude of $\widetilde{w}$ (figure 3d), which is consistent with the observation in figure 2.

Figure 4 shows the spatial distribution of the wave-induced streamwise velocity

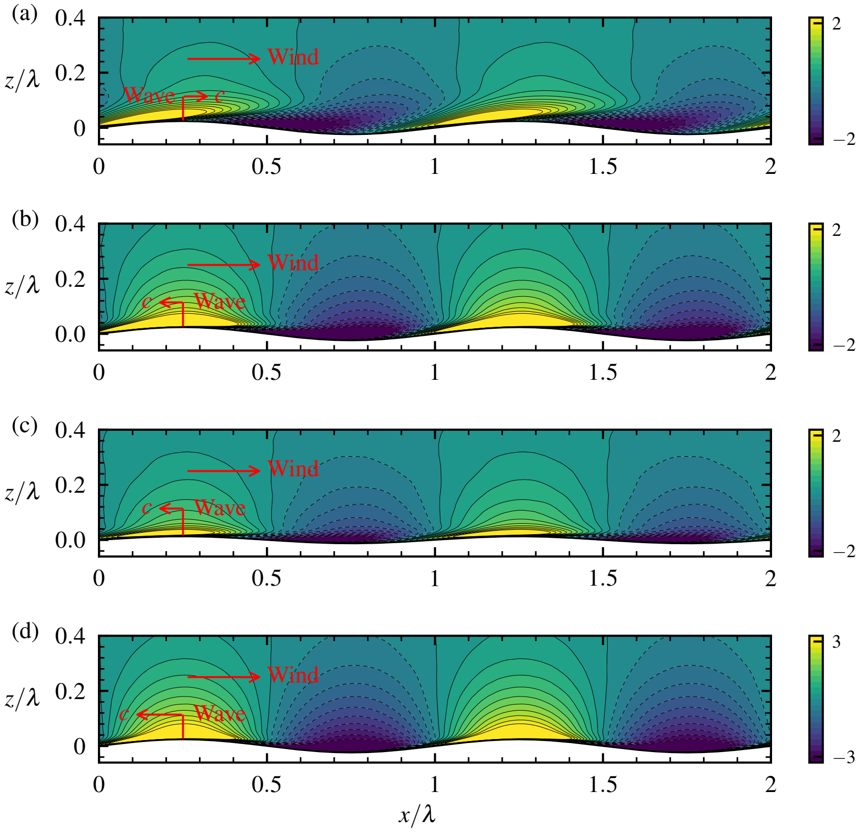

Figure 4: Spatial distribution of the wave-induced streamwise velocity $\widetilde{u}$ for the wave conditions: (a) WFW01, $c/U_0 = 0.1$, $ak = 0.15$; (b) WOW01, $c/U_0 = -0.1$, $ak = 0.15$; (c) WOW01L, $c/U_0 = -0.1$, $ak = 0.08$; (d) WOW04, $c/U_0 = -0.4$, $ak = 0.15$. The results are normalised by u_τ.

$\widetilde{u}$ for the wave conditions corresponding to figure 3. For the opposing waves, on the contrary to the antisymmetric distribution of $\widetilde{w}$, $\widetilde{u}$ displays nearly symmetric spatial distribution about the wave crest away from the wave surface (figure 4b–d), which is not exhibited in the following wave case (figure 4a). However, near the opposing wave surface, $\widetilde{u}$ deviates from the symmetric distribution noticeably and reaches its maximum on the windward side near the wave crest, which is similar to the following wave case. While the spatial structure of $\widetilde{u}$ is similar among different opposing wave cases, its magnitude varies with the opposing wave parameters. Similar to $\widetilde{w}$, the magnitude of $\widetilde{u}$ increases with the wave speed and wave steepness.

We note that although a strong negative $\widetilde{u}$ is present near the surface at the leeward face in all of the four wave cases, no apparent flow separation is observed in the mean flow. While the flow separation past a steady sinusoidal wavy surface was found to cause a recirculation zone downstream the wave crest (e.g., Buckles *et al.*, 1984), the feature and criterion for the occurrence of airflow separation over water waves are still not fully understood, especially when the waves do not break, as pointed by Buckley & Veron (2016). For the non-breaking following waves, airflow separation has been found to happen only sporadically in the instantaneous field, and is difficult to visualize in the mean field. For instance, in their experimental studies, Veron *et al.* (2007) and Buckley & Veron (2016) only visualized the airflow separation in individual detachment events. In DNS, Yang & Shen (2010) and Druzhinin *et al.* (2012) found that although airflow separation presents occasionally in the instantaneous flow field, no apparent separation in the mean flow is observed. For opposing waves, the study on airflow separation is even less in the literature and requires data of turbulent wind opposing waves with the wave steepness and Reynolds numbers systematically varied, which should be considered in future studies with a large number of simulation cases conducted.

As a summary of this subsection, the LES results illustrate the key features of the wave-induced vertical velocity $\widetilde{w}$ and streamwise velocity $\widetilde{u}$ under the opposing wave condition. The $\widetilde{w}$ appears antisymmetric throughout the wave boundary layer while $\widetilde{u}$ is symmetric away from the surface, which has led some previous studies to use potential flow theory to explain their arising. However, near the wave surface, $\widetilde{u}$ is no longer symmetric, suggesting that the potential flow theory is inadequate to describe the flow dynamics. The detailed physical mechanisms for $\widetilde{w}$ and $\widetilde{u}$ are investigated in § 2.5.1 and § 2.5.2, respectively.

2.3.2 Wave-induced stress and pressure

The proceeding subsection shows that the wave direction is a key factor in determining the pattern of wave-induced velocity. Consequently, the wave-coherent stress, $-\widetilde{u}\widetilde{w}$, also reflects the impact of the wave direction, which is shown in figure 5. In the following wave case WFW01 (which has $c/u_\tau = 3.46$), $-\widetilde{u}\widetilde{w}$ is mostly negative, especially near the wave surface (figure 5a), which is consistent with the results of the case $(c/u_\tau,\ ak) = (3.7,\ 0.13)$ in Buckley & Veron (2016), but is different from the pattern in the case $(c/u_\tau,\ ak) = (6.27,\ 0.07)$ in Yousefi *et al.* (2020) because the latter used curvilinear coordinate variables to define the wave-coherent stress. The corresponding opposing wave (figure 5b) results in alternating positive and negative $-\widetilde{u}\widetilde{w}$ along the wave surface, which displays an antisymmetric distribution away from the surface. This feature of $-\widetilde{u}\widetilde{w}$ is also exhibited by the other two opposing wave cases (figure 5c and d), and is caused by the nearly antisymmetric $\widetilde{w}$ and symmetric

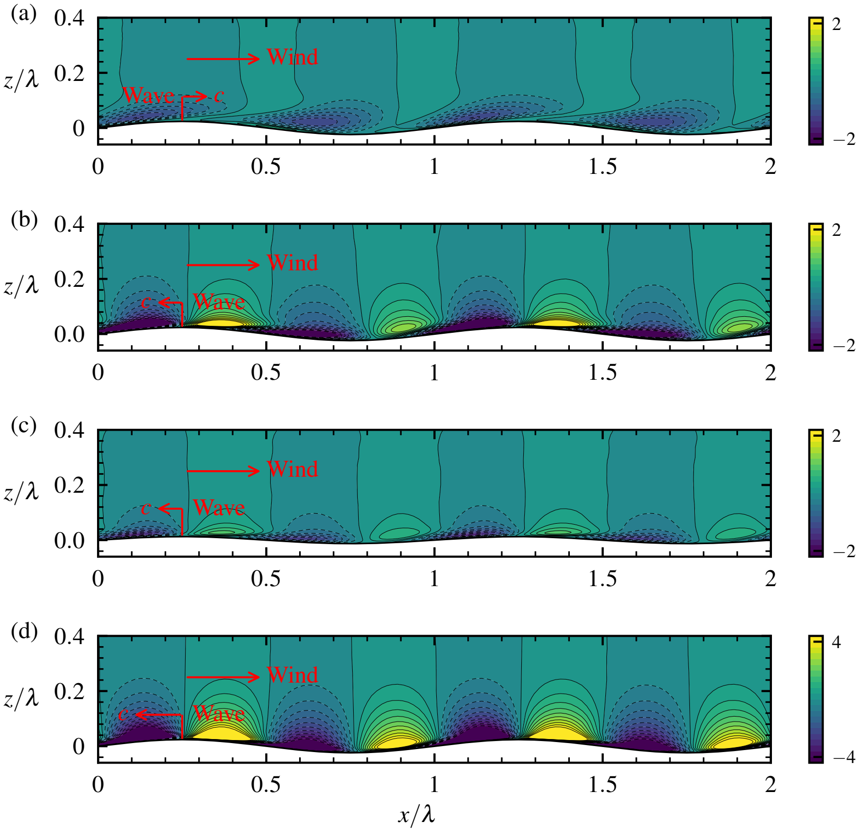

Figure 5: Spatial distribution of the wave-induced stress $-\widetilde{u}\widetilde{w}$ for the wave conditions: (a) WFW01, $c/U_0 = 0.1$, $ak = 0.15$; (b) WOW01, $c/U_0 = -0.1$, $ak = 0.15$; (c) WOW01L, $c/U_0 = -0.1$, $ak = 0.08$; (d) WOW04, $c/U_0 = -0.4$, $ak = 0.15$. The results are normalised by u_τ^2.

$\widetilde{u}$ (figures 3 and 4). Near the wave surface, because $\widetilde{u}$ deviates from the symmetric distribution, $-\widetilde{u}\widetilde{w}$ no longer exhibits antisymmetry there.

In addition to $-\widetilde{u}\widetilde{w}$, surface waves also induce pressure perturbation in the airflow to impact the momentum flux. Previous laboratory and field measurements have reported that the pressure induced by opposing waves is nearly symmetric about the surface wave crest (Snyder *et al.*, 1981; Young & Sobey, 1985; Hasselmann & Bsenberg, 1991), which is also reflected in the present LES results. In figure 6, we plot the spatial distribution of $\widetilde{p}$ for the four wave conditions. It is obvious that for the same wave parameters, the pressure induced by the opposing wave (figure 6b) is much stronger and more symmetric about the wave crest compared with that induced by the following wave (figure 6a). In the latter case, the pressure distribution is mostly positive on the windward face of the wave and negative on the leeward side. The seemingly symmetric distribution of $\widetilde{p}$ induced by opposing waves is also present with a lower wave steepness (figure 6c) and a faster wave speed (figure 6d).

In this subsection, the LES results show that the opposing waves induce nearly antisymmetric wave-coherent stress $-\widetilde{u}\widetilde{w}$ away from the wave surface, and nearly symmetric wave-coherent pressure $\widetilde{p}$ throughout the wave boundary layer. Similar to $\widetilde{w}$ and $\widetilde{u}$, the pattern of $-\widetilde{u}\widetilde{w}$ and $\widetilde{p}$ are similar among the different opposing wave cases, but with their magnitudes varying. The detailed physical mechanisms for $-\widetilde{u}\widetilde{w}$ and $\widetilde{p}$ are investigated in § 2.5.3.

2.3.3 Wave-induced turbulence variance and turbulent stress

In this subsection, we examine the modulation of turbulence variance $u'u' + w'w'$ and turbulent stress $-u'w'$ by the opposing waves. In the present study, the tur-

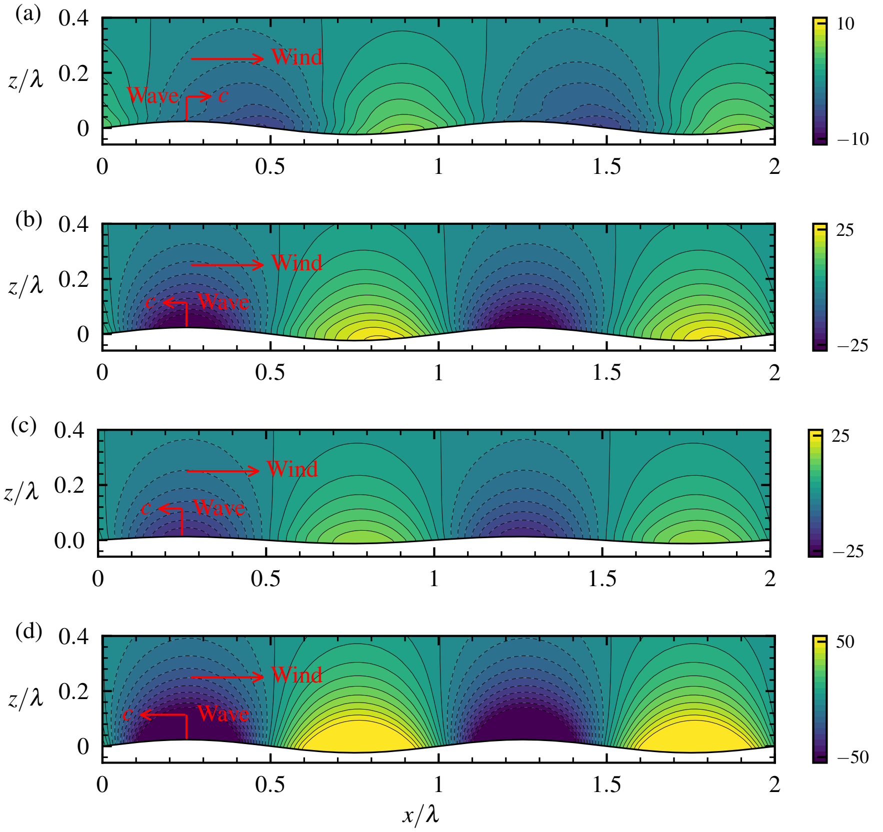

Figure 6: Spatial distribution of the wave-induced pressure $\widetilde{p}$ for the wave conditions: (a) WFW01, $c/U_0 = 0.1$, $ak = 0.15$; (b) WOW01, $c/U_0 = -0.1$, $ak = 0.15$; (c) WOW01L, $c/U_0 = -0.1$, $ak = 0.08$; (d) WOW04, $c/U_0 = -0.4$, $ak = 0.15$. The results are normalised by $\rho_a u_\tau^2$.

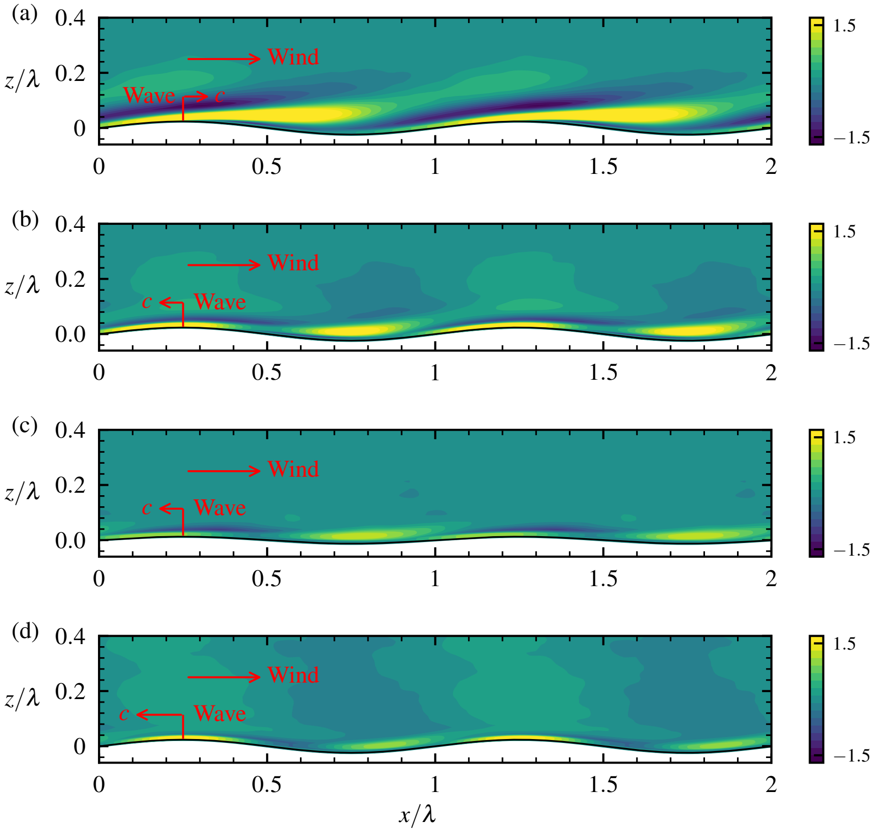

Figure 7: Spatial distribution of the wave-induced turbulence variance $\widetilde{u'u'}+\widetilde{w'w'}$ for the wave conditions: (a) WFW01, $c/U_0 = 0.1$, $ak = 0.15$; (b) WOW01, $c/U_0 = -0.1$, $ak = 0.15$; (c) WOW01L, $c/U_0 = -0.1$, $ak = 0.08$; (d) WOW04, $c/U_0 = -0.4$, $ak = 0.15$. The results are normalised by u_τ^2.

bulence variance and turbulent stress are defined using the variables in the Cartesian coordinate. Adopting definitions based on the curvilinear coordinate variables may result in different appearance, as discussed in Yousefi *et al.* (2020). Figure 7 presents the spatial distribution of the wave-induced turbulence variance $\widetilde{u'u'}+\widetilde{w'w'} = \overline{u'u'} - \langle u'u' \rangle + \overline{w'w'} - \langle w'w' \rangle$ (see § 2.2.2 for definitions of averaging) for different wave conditions, to illustrate how the turbulence intensity is affected by the presence of surface waves. It is shown that in the following wave case WFW01 (figure 7a), there is a strong positive $\widetilde{u'u'}+\widetilde{w'w'}$ above the leeward face of the wave. In the corresponding opposing wave case WOW01 (figure 7b), the region for the intensified turbulence variance moves further downstream towards the wave trough. More importantly, in the opposing wave case WOW01, the region for strong $\widetilde{u'u'}+\widetilde{w'w'}$ is concentrated in a much thinner region compared with the following wave case WFW01. In the less steep wave case WOW01L (figure 7c), the pattern of $\widetilde{u'u'}+\widetilde{w'w'}$ is similar to case WOW01 but with a smaller magnitude. In the fast opposing wave case WOW04 (figure 7d), $\widetilde{u'u'}+\widetilde{w'w'}$ is much weaker and is confined within an even thinner region compared with case WOW01.

In figure 8, we plot the spatial distribution of the wave-induced turbulent shear stress $-\widetilde{u'w'} = -\overline{u'w'} - \langle -u'w' \rangle$ for different wave conditions, which quantifies how the turbulent shear stress $-u'w'$ is modulated by the presence of surface waves. The comparison between cases WFW01 (figure 8a) and WOW01 (figure 8b) shows that, near the wave surface, both the following wave and opposing wave induce a negative $-\widetilde{u'w'}$ at the windward side and a positive $-\widetilde{u'w'}$ further downstream. However, the strong $-\widetilde{u'w'}$ is limited to a much thinner region in the opposing wave cases, which is similar to the behaviour of $\widetilde{u'u'}+\widetilde{w'w'}$ shown in figure 7. Furthermore, the

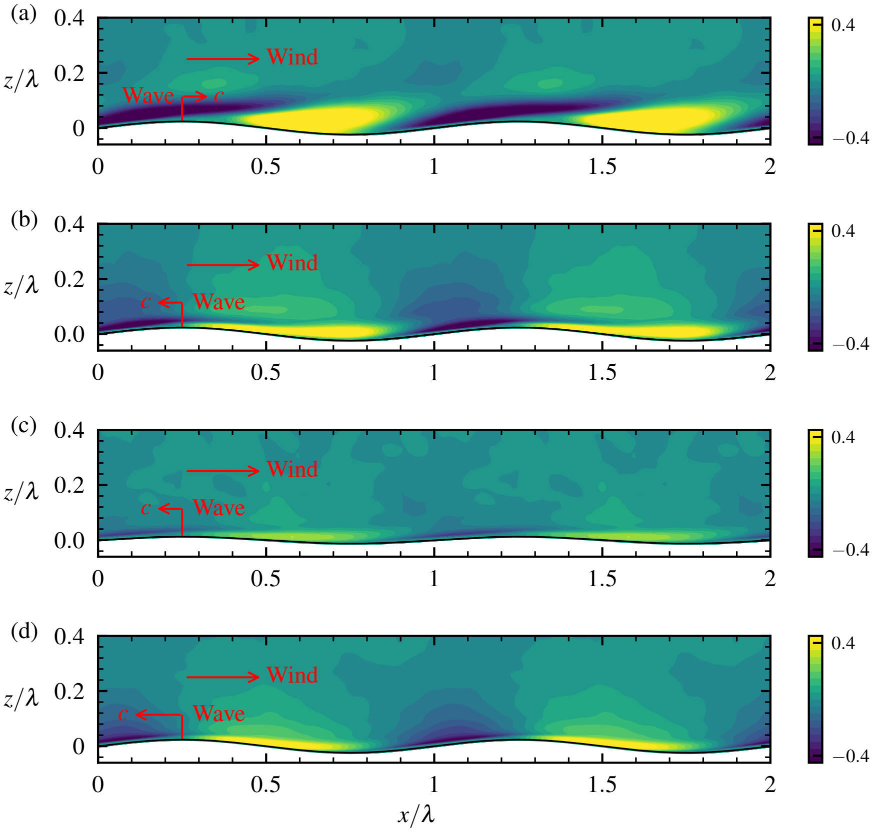

Figure 8: Spatial distribution of the wave-induced turbulent stress $-\widetilde{u'w'}$ for the wave conditions: (a) WFW01, $c/U_0 = 0.1$, $ak = 0.15$; (b) WOW01, $c/U_0 = -0.1$, $ak = 0.15$; (c) WOW01L, $c/U_0 = -0.1$, $ak = 0.08$; (d) WOW04, $c/U_0 = -0.4$, $ak = 0.15$. The results are normalised by u_τ^2.

region of strong $-\widetilde{u'w'}$ becomes even thinner as the opposing wave becomes faster in case WOW04 (figure 8d). Away from the wave surface, $-\widetilde{u'w'}$ is relatively weak and exhibits a quasi-antisymmetric spatial distribution about the wave crest for the opposing wave cases WOW01 and WOW04, which is not observed in the following wave case WFW01 for the same wave steepness.

To summarize this subsection, we have observed that the strong opposing wave-induced turbulence variance and turbulent stress is limited to a much thinner region in the airflow, compared with the wind over slow following wave case. This result is consistent with the conclusion we obtain in § 2.5.1 below that the region where the in-phase component of $\widetilde{w}$ is affected by the wave-induced turbulent stress is much thinner for the opposing wave than the corresponding following wave.

To conclude § 2.3, we have investigated the features of wave-induced velocity, pressure, and turbulence statistics in the opposing wave condition. Next, we present a viscous linearised model for $\widetilde{w}$ in the mapped computational curvilinear coordinate in § 2.4, based on which the physical mechanisms underlying the arising of the opposing wave-induced airflow $\widetilde{w}$, $\widetilde{u}$, $-\widetilde{u}\widetilde{w}$, and $\widetilde{p}$ shown in § 2.3 are explained in § 2.5.

2.4 Viscous linearised model for the opposing wave effects

In § 2.3, we have shown the key characteristics of the opposing wave effects on the velocity, pressure, and turbulence statistics in the airflow based on the LES data. To investigate the mechanisms underlying the opposing wave effects, in this section, we develop a new viscous model for the wave-induced velocity by linearising the phase-averaged Navier–Stokes equations for the mean wind velocity in the mapped computational curvilinear coordinate.

The transformation between the physical coordinate (x, y, z) and mapped computational curvilinear coordinate (ξ, ψ, ζ) given by (7) is non-orthogonal and follows the form of Hsu *et al.* (1981) and Hsu & Hsu (1983), which has been widely adopted in the literature to study the wave-induced quantities using a variety of mapping functions (e.g., Snyder *et al.*, 1981; Young & Sobey, 1985; Mastenbroek, 1996; Yang & Shen, 2010; Hara & Sullivan, 2015; Akervik & Vartdal, 2019). As suggested by Hsu *et al.* (1981), in principle, any function g can be considered if it satisfies $g(0) = -1$ and increases monotonically to zero at the top of the boundary layer. A function satisfies this condition guarantees that the transformation is one to one but may result in sampling points that are not at the ideal offset, e.g. constant distance, from the wave surface, and the resulting transformed coordinate is not necessarily aligned with the mean streamlines. The use of the transformation of the form (7) has been able to reveal important results of the turbulent wind–wave interaction (see the above-mentioned studies). In the following derivation, we assumes the transformation follows the form of (7), but we do not specify a particular transformation function g.

To derive the viscous linearised model, we use the LES equations in the mapped computational curvilinear coordinate in the strongly conservative form (e.g., Hara & Sullivan, 2015)

$$\frac{\partial(J^{-1}u_j)}{\partial t} + \frac{\partial}{\partial \xi_m}\Big(u_j U_m + J^{-1} p \frac{\partial \xi_m}{\partial x_j} + J^{-1}\sigma_{jl}\frac{\partial \xi_m}{\partial x_l} + J^{-1}\tau_{jl}^{d}\frac{\partial \xi_m}{\partial x_l}\Big) = 0, \quad (16)$$

$$\frac{\partial U_j}{\partial \xi_j} = 0, \quad (17)$$

where J is the determinant of the transformation matrix $\boldsymbol{J}$, and $\sigma_{jm} = -2\nu S_{jm}$ is the viscous stress tensor with $S_{jm} = (\partial u_j/\partial x_m + \partial u_m/\partial x_j)/2$ being the deformation tensor, τ^d_{jm} is the SGS stress tensor in (2), and $U_j = J^{-1}u_m\partial\xi_j/\partial x_m$ is the velocity in the curvilinear coordinate system. Physically, U_j is the velocity component perpendicular to the constant ξ_j surface and quantifies the volume flux in the curvilinear coordinate. In (16), u_iU_j represents the flux of the x_i-component momentum across a constant ξ_j plane caused by the advection velocity U_j (Chou & Fringer, 2010; Sullivan *et al.*, 2000; Hara & Sullivan, 2015).

The equations governing the phase-averaged flow field are obtained by the phase average of (16) and (17) in the reference frame travelling with the surface wave $\xi - ct$,

$$\frac{\partial}{\partial\xi_m}\Big(\overline{u}_j\overline{U}_m + \overline{\tau}_{jm} + \overline{\tau}^p_{jm} + \overline{\tau}^v_{jm}\Big) = 0, \tag{18}$$

$$\frac{\partial\overline{U}_j}{\partial\xi_j} = 0, \tag{19}$$

where $\tau_{jm} = u'_jU'_m + J^{-1}\tau^d_{jl}\partial\xi_m/\partial x_l$, $\tau^p_{jm} = J^{-1}p\partial\xi_m/\partial x_j$, and $\tau^v_{jm} = J^{-1}\sigma_{jl}\partial\xi_m/\partial x_l$ are the turbulent stress, pressure stress, and viscous stress, respectively. Here, τ_{ij} is the sum of the resolved turbulent stress and SGS stress, both of which represent the turbulence effect.

The mean momentum and continuity equations can be obtained by applying the triple decomposition (12) to each term in (18) and (19), and then performing spatial average in the (ξ, ψ) plane, which yields

$$\frac{\partial}{\partial\zeta}\Big(\langle\tau^w_{j3}\rangle + \langle\tau_{j3}\rangle + \langle\tau^p_{j3}\rangle + \langle\tau^v_{j3}\rangle\Big) = 0, \tag{20}$$

$$\frac{\partial\langle W\rangle}{\partial\zeta} = 0, \tag{21}$$

where $\tau^w_{jm} = \widetilde{u}_j\widetilde{U}_m$ is the wave-induced stress, resulting from the correlation between the components of the wave-induced velocity. In (21), $\partial\langle U\rangle/\partial\xi = 0$ because $\langle U\rangle$ is averaged over the (ξ, ψ) plane and thus its derivative with respect to ξ is zero.

Next, we extract the momentum equations governing the wave-coherent air motions by subtracting the mean equations (20) and (21) from the phase-averaged equations (18) and (19), respectively,

$$\frac{\partial}{\partial \xi_m}\left(\widetilde{u}_j\langle U_m\rangle + \langle u_j\rangle \widetilde{U}_m + \widetilde{\tau}^w_{jm} + \widetilde{\tau}^p_{jm} + \widetilde{\tau}_{jm} + \widetilde{\tau}^v_{jm}\right) = 0, \tag{22}$$

$$\frac{\partial \widetilde{U}_j}{\partial \xi_j} = 0, \tag{23}$$

where $\widetilde{\tau}^w_{jm}$, $\widetilde{\tau}^p_{jm}$, $\widetilde{\tau}_{jm}$, and $\widetilde{\tau}^v_{jm}$ are the wave-induced fluctuations of τ^w_{jm}, τ^p_{jm}, τ_{jm}, and τ^v_{jm} (18), respectively.

Inspired by Young & Sobey (1985) that the opposing wave-induced airflow may be dominated by the linear dynamics, in this study, we first neglect the nonlinear forcing in (22), i.e. $\widetilde{\tau}_{jm}$ and $\widetilde{\tau}^w_{jm}$, to investigate the linear dynamics in the generation of wave-induced velocity. Equations (22) and (23) are complex owing to the introduction of curvilinear coordinate velocity U_j to the various stress terms and also owing to the correlation between the velocity and the grid transformation terms. To better illustrate the physical processes therein, we simplify (22) and (23) using the primitive variables in the physical space based on the properties of the wave-induced quantities. The simplification of the wave-induced velocity $\widetilde{U}_j$, the pressure stress $\widetilde{\tau}^p_{jm}$, and the wave-induced viscous stress $\widetilde{\tau}^v_{jm}$ is presented in appendix C. The resulting momentum and continuity equations for the wave-induced air motions are

$$\begin{aligned}
(\langle u\rangle - c)\frac{\partial \widetilde{u}}{\partial \xi} + (\widetilde{w} + (\langle u\rangle - c) g\widetilde{\eta}_\xi)\frac{\mathrm{d}\langle u\rangle}{\mathrm{d}\zeta} + \frac{\partial \widetilde{p}}{\partial \xi} &= \nu\Big(\frac{\partial^2 \widetilde{u}}{\partial \zeta^2} - \frac{\partial^2 \widetilde{w}}{\partial \xi \partial \zeta}\Big) \\
&\quad + \nu\frac{\mathrm{d}}{\mathrm{d}\zeta}\Big(\frac{\mathrm{d}\langle u\rangle}{\mathrm{d}\zeta} g_\zeta\Big)\widetilde{\eta} + O((ak)^2) + n.l.f., \qquad (24) \\
(\langle u\rangle - c)\frac{\partial \widetilde{w}}{\partial \xi} + \frac{\partial \widetilde{p}}{\partial \zeta} &= \nu\Big(\frac{\partial^2 \widetilde{w}}{\partial \xi^2} + \frac{\partial^2 \widetilde{w}}{\partial \zeta^2}\Big) + O((ak)^2) + n.l.f., \qquad (25) \\
\frac{\partial \widetilde{u}}{\partial \xi} + \frac{\partial \widetilde{w}}{\partial \zeta} + \frac{\mathrm{d}\langle u\rangle}{\mathrm{d}\zeta} g\widetilde{\eta}_\xi &= 0 + O((ak)^2), \qquad (26)
\end{aligned}$$

where $O((ak)^2)$ denotes the neglected second and higher -order terms, and the '*n.l.f.*' represents the neglected nonlinear forcing, i.e. $\widetilde{\tau}_{ij}$ and $\widetilde{\tau}^w_{ij}$.

Equations (24)–(26) can be combined into the following equation governing the wave-coherent vertical velocity,

$$\begin{aligned}
-\frac{\nu}{\mathrm{i}k}\left[\frac{\mathrm{d}^4}{\mathrm{d}\zeta^4} - 2k^2\frac{\mathrm{d}^2}{\mathrm{d}\zeta^2} + k^4\right]\widehat{w} + \left[(\langle u\rangle - c)\Big(\frac{\mathrm{d}^2}{\mathrm{d}\zeta^2} - k^2\Big) - \frac{\mathrm{d}^2\langle u\rangle}{\mathrm{d}\zeta^2}\right]\widehat{w} \\
= \nu\widehat{\eta}\frac{\mathrm{d}^2}{\mathrm{d}\zeta^2}\left[g\frac{\mathrm{d}^2\langle u\rangle}{\mathrm{d}\zeta^2}\right] + O((ak)^2) + n.l.f, \qquad (27)
\end{aligned}$$

where $\widehat{w}$ is the Fourier coefficient of $\widetilde{w}$. The left hand side of (27) has the same form as the Orr–Sommerfeld equation (e.g., Lin, 1955; Orszag, 1971), with the first bracket representing the viscous effect and the second bracket associated with the advection effect (note that the present formulation is in the mapped computational coordinate), while the right hand side has a source term. We remark that (27) is derived based on the strongly conservative equations (16) and (17), which can be obtained from the weakly conservative equations (10) and (11) by rearranging all of the terms into the forms of the derivatives of the curvilinear coordinate quantities with respect to (ξ, ψ,

ζ, τ) (e.g., Anderson, Tannehill & Pletcher, 1984). The strongly conservative equations induce simplifications in the derivation process, as the derivatives of different quantities with respect to the same variable are grouped together. Nevertheless, in appendix D, we show that (27) can also be derived from (10) and (11).

Equation (27) can be solved to obtain the Fourier coefficient of $\widetilde{w}$, i.e. $\widehat{w}$, given the Dirichlet boundary condition for $\widehat{w}$

$$\widehat{w}\big|_{\zeta=0} = \widehat{w}_s, \qquad \widehat{w}\big|_{\zeta=\infty} = 0, \tag{28}$$

where $\widehat{w}_s$ is the Fourier coefficient of the vertical wave orbital velocity and also the boundary condition for $\mathrm{d}\widehat{w}/\mathrm{d}\zeta$, which is obtained from the continuity equation (26)

$$\left.\frac{\mathrm{d}\widehat{w}}{\mathrm{d}\zeta}\right|_{\zeta=0} = -\mathrm{i}k\widehat{u}_s - \mathrm{i}k\widehat{\eta}\left.\left(g\frac{\mathrm{d}\langle u\rangle}{\mathrm{d}\zeta}\right)\right|_{\zeta=0}, \qquad \left.\frac{\mathrm{d}\widehat{w}}{\mathrm{d}\zeta}\right|_{\zeta=\infty} = 0. \tag{29}$$

With (27)–(29), we see that the water wave affects the airflow in two ways. First, the wave elevation $\widehat{\eta}$ leads to a source term on the right hand side of (27). Second, the wave kinematics impose the velocity boundary condition for (27).

Next, it is instructive to examine how $\mathrm{Re}[\widehat{w}]$ and $\mathrm{Im}[\widehat{w}]$ arise in (27). With (28) and (29) and using (4) and (6), the real and imaginary parts of $\widehat{w}$ and $\mathrm{d}\widehat{w}/\mathrm{d}\zeta$ at the wave surface can be obtained as

$$\mathrm{Re}[\widehat{w}]\big|_{\zeta=0} = -\frac{1}{2}akc, \qquad \left.\frac{\mathrm{d}\,\mathrm{Re}[\widehat{w}]}{\mathrm{d}\zeta}\right|_{\zeta=0} = -\frac{1}{2}ak^2c - \frac{1}{2}ak\left.\left(g\frac{\mathrm{d}\langle u\rangle}{\mathrm{d}\zeta}\right)\right|_{\zeta=0}, \tag{30}$$

$$\mathrm{Im}[\widehat{w}]\big|_{\zeta=0} = 0, \qquad \left.\frac{\mathrm{d}\,\mathrm{Im}[\widehat{w}]}{\mathrm{d}\zeta}\right|_{\zeta=0} = 0. \tag{31}$$

Hence, through affecting the values of $\mathrm{Re}[\widehat{w}]$ and $\mathrm{d}\,\mathrm{Re}[\widehat{w}]/\mathrm{d}\zeta$ at the wave surface, the wave orbital velocity impacts the arising of $\mathrm{Re}[\widehat{w}]$ throughout the wave boundary layer. On the contrary, $\mathrm{Im}[\widehat{w}]$ and $\mathrm{d}\,\mathrm{Im}[\widehat{w}]/\mathrm{d}\zeta$ have homogeneous boundary conditions at the wave surface, and thus the generation of $\mathrm{Im}[\widehat{w}]$ are not directly affected by the wave orbital velocity at the surface.

Although not driven by the motions of the surface waves, $\mathrm{Im}[\widehat{w}]$ can still arise in the viscous equation (27) through the interaction with $\mathrm{Re}[\widehat{w}]$, which is triggered by the viscous stress therein. This physical process can be shown by taking the imaginary part of (27) with respect to the advection term

$$\frac{\nu}{k}\left[\frac{\mathrm{d}^4}{\mathrm{d}\zeta^4} - 2k^2\frac{\mathrm{d}^2}{\mathrm{d}\zeta^2} + k^4\right]\mathrm{Re}[\widehat{w}] + \left[(\langle u\rangle - c)\left(\frac{\mathrm{d}^2}{\mathrm{d}\zeta^2} - k^2\right) - \frac{\mathrm{d}^2\langle u\rangle}{\mathrm{d}\zeta^2}\right]\mathrm{Im}[\widehat{w}]$$
$$= -\nu\frac{1}{2}a\frac{\mathrm{d}^2}{\mathrm{d}\zeta^2}\left[g\frac{\mathrm{d}^2\langle u\rangle}{\mathrm{d}\zeta^2}\right] + O((ak)^2) + n.l.f., \qquad (32)$$

where $\mathrm{Re}[\widehat{w}]$ and $\mathrm{Im}[\widehat{w}]$ are present in the viscous and advection terms, respectively, indicating that a nonzero $\mathrm{Re}[\widehat{w}]$ can lead to the arising of $\mathrm{Im}[\widehat{w}]$. This mechanism expressed by (32) illustrates how viscous stress induces $\mathrm{Im}[\widehat{w}]$ to cause $\widetilde{w}$ to deviate from the perfect antisymmetry.

Outside of the viscous layer, the viscous equation (27) reduces to the inviscid equation, which is obtained by neglecting the terms related to viscosity in (27)

$$\left[\left(\frac{\mathrm{d}^2}{\mathrm{d}\zeta^2} - k^2\right) - \frac{1}{\langle u\rangle - c}\frac{\mathrm{d}^2\langle u\rangle}{\mathrm{d}\zeta^2}\right]\widehat{w} = 0 + O((ak)^2) + n.l.f. + v.i.s., \qquad (33)$$

where the '*v.i.s.*' represents the neglected viscous terms. To solve (33), only the boundary condition for $\widehat{w}$ given in (28) is needed.

The key feature of (33) is that in the absence of turbulent stress and viscous effect, the behaviour of $\widetilde{w}$ does not depend on the geometric transformation function, i.e. g, which transforms the physical coordinate to the mapped computational curvilinear coordinate as shown in (7) and appears in the viscous equation (27). In other words, using the transformation (7), $\widetilde{w}$ follows the general form given by (33) away from the wave surface, where the advection of the wave-coherent airflow dominates the nonlinear stress and viscous stress. Under the wind-opposing-wave condition, due to the large magnitude of $\langle u\rangle - c$ away from the wave surface caused by the negative wave celerity, the dynamic effect of the second term in (33) is small. Asymptotically, for sufficiently fast opposing waves, the inviscid linear equation (33) reduces to a Laplacian equation

$$\Big(\frac{\mathrm{d}^2}{\mathrm{d}\zeta^2} - k^2\Big)\widehat{w} = 0, \tag{34}$$

which gives a solution with an exponential decay rate $\mathrm{e}^{-k\zeta}$. This result provides a perspective on the exponential decay of the opposing wave-induced vertical velocity away from the wave surface in the previous laboratory measurement by Young & Sobey (1985) (not plotted here for space consideration).

In summary of this section, we present a new viscous linearised model formulated in the mapped computational curvilinear coordinate to incorporate several key effects neglected in the potential flow theory, including the viscous stress, mean wind shear, and the wave elevation. Next, in § 2.5, the solutions of the linearised equations are compared with the LES results to show the physical dynamics underlying the opposing wave-induced flow field.

2.5 Physical mechanisms underlying opposing wave-induced airflow

In § 2.4, we have obtained the viscous (27) and inviscid (33) linearised equations for the wave-induced airflow. In this section, we numerically solve (27) using the mean wind velocity $\langle u \rangle$ from the LES. Through the comparison between the linear solutions and LES results, we analyse the mechanisms for the arising of $\widetilde{w}$ (§ 2.5.1), $\widetilde{u}$ (§ 2.5.2), $-\widetilde{u}\widetilde{w}$ and $\widetilde{p}$ (§ 2.5.3), and explain their spatial structures observed in § 2.3.

2.5.1 Wave-induced vertical velocity $\widetilde{w}$

We first investigate the wave-induced vertical velocity, $\widetilde{w}$, which can be directly solved from (27). With (15), $\widetilde{w}$ is represented as

$$\widetilde{w} = 2|\widehat{w}| \sin\bigl(k\xi - \phi_{\widetilde{w}\widetilde{\eta}}\bigr), \tag{35}$$

where $2|\widehat{w}|$ is the magnitude of $\widetilde{w}$ and $\phi_{\widetilde{w}\widetilde{\eta}}$ is the phase difference between $\widetilde{w}$ and $\widetilde{\eta}$. Figure 9 presents the comparison of $|\widehat{w}|$ (figure 9a), $\mathrm{Re}[\widehat{w}]$ (figure 9b), $\mathrm{Im}[\widehat{w}]$ (figure 9c), and $\phi_{\widetilde{w}\widetilde{\eta}}$ (figure 9d) between the LES results and solutions of the viscous linearised equation (27) for the four representative wave conditions. As shown, for opposing waves, the magnitude of $|\widehat{w}|$ is close to $\mathrm{Re}[\widehat{w}]$, and for both of them the solutions of (27) agree well with the LES results (figure 9a and b), while $\mathrm{Im}[\widehat{w}]$ does not change the behaviour of $|\widehat{w}|$ significantly because of its small magnitude, and is underestimated by the present viscous model (figure 9c). Because $|\,\mathrm{Im}[\widehat{w}]| \ll |\,\mathrm{Re}[\widehat{w}]|$, $\phi_{\widetilde{w}\widetilde{\eta}} \approx \pi/2$ in both the linear solutions and the LES results (figure 9d). This result indicates that $\widetilde{w}$ is dominated by its out-of-phase component $\mathrm{Re}[\widehat{w}]$ and is thus nearly

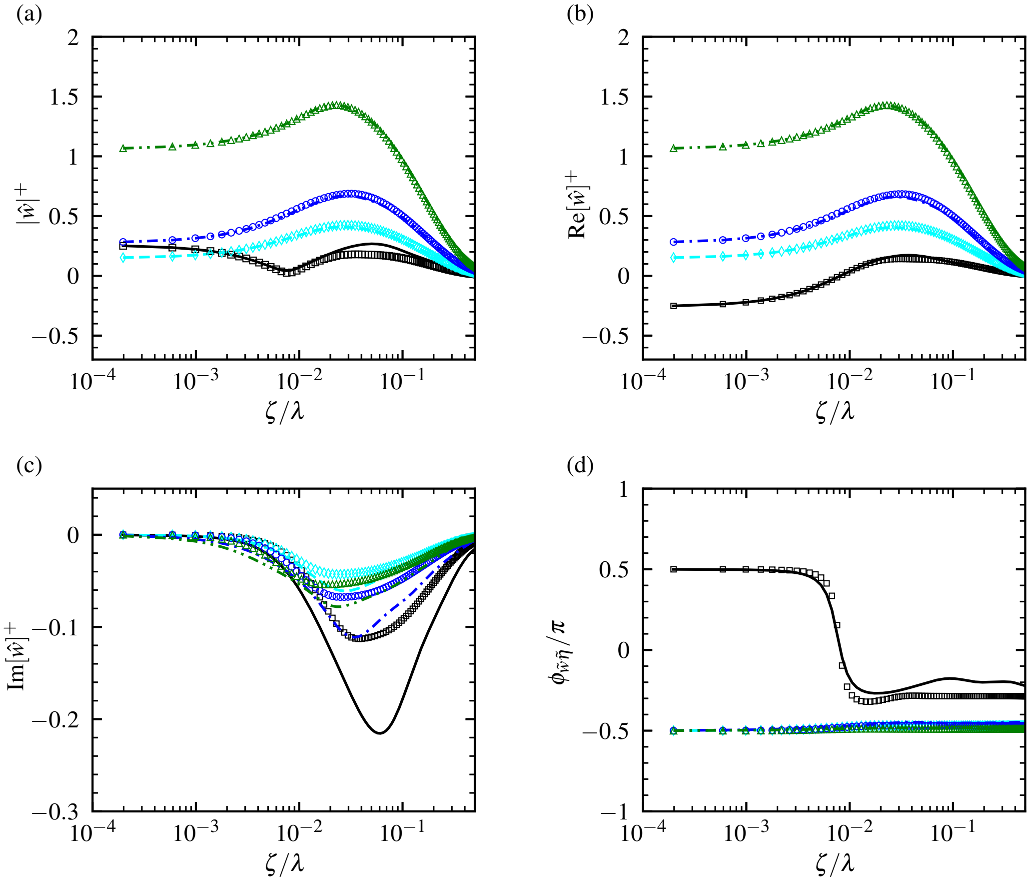

Figure 9: Comparison of (a) $|\widehat{w}|$, (b) $\mathrm{Re}[\widehat{w}]$, (c) $\mathrm{Im}[\widehat{w}]$, and (d) $\phi_{\widetilde{w}\widetilde{\eta}}$ between the LES results: WFW01 (—), WOW01 (-·-), WOW01L (- - -), and WOW04 (-··-); and the solutions of the viscous linearised equation (27): WFW01 (□), WOW01 (○), WOW01L(◇), and WOW04 (△). The superscript '+' denotes normalisation by u_τ. Note the scale difference between (b) and (c).

antisymmetric as shown in figure 3. On the contrary, in the following wave case WFW01, $\mathrm{Im}[\widehat{w}]$ is comparable to $\mathrm{Re}[\widehat{w}]$ throughout the wave boundary layer, and thus both of them affect $\widetilde{w}$. In addition, there exists a sharp change of $\phi_{\widetilde{w}\widetilde{\eta}}$, from approximately 0.5π for $\zeta < 0.006\lambda$ to about -0.2π for $\zeta > 0.012\lambda$, which is related to the effect of the critical height located at $\zeta \approx 0.008\lambda$ and causes the tilting of $\widetilde{w}$ in figure 3(a). Note that the present $\phi_{\widetilde{w}\widetilde{\eta}}$ difference across the critical height may not be quantified by the inviscid Rayleigh equation of the critical layer theory because $c/u_\tau < 5$ (Miles, 1957, 1993); at intermediate c/u_τ, the Rayleigh equation predicts a near $\pi/2$ difference of $\phi_{\widetilde{w}\widetilde{\eta}}$ (Miles, 1957; Hristov *et al.*, 2003), which is reflected in field observations (Hristov *et al.*, 2003; Grare *et al.*, 2013*a*).

Linear dynamics for $\mathrm{Re}[\widehat{w}]$ **induced by wave kinematics** As shown above, the behaviour of $\widetilde{w}$ in the wind opposing waves depends mostly on its strong out-of-phase component $\mathrm{Re}[\widehat{w}]$, which is antisymmetric about the wave crest. In general, $\mathrm{Re}[\widehat{w}]$ corresponds to the alternating upward and downward air motions across the wave crest, which can be seen from its contribution to $\widetilde{w}$ in the physical space (15)

$$\widetilde{w} = 2\,\mathrm{Re}[\widehat{w}]\cos(k\xi) = 2\frac{\mathrm{Re}[\widehat{w}]}{ak}\frac{\mathrm{d}\widetilde{\eta}}{\mathrm{d}\xi}, \tag{36}$$

where the last equality holds because $\widetilde{\eta} = a\sin(k\xi)$, and $\mathrm{d}\widetilde{\eta}/\mathrm{d}\xi$ is the slope of the wave surface. When the wind blows from left to right, because $\mathrm{d}\widetilde{\eta}/\mathrm{d}\xi > 0$ on the windward side and $\mathrm{d}\widetilde{\eta}/\mathrm{d}\xi < 0$ on the leeward side, we see that a positive $\mathrm{Re}[\widehat{w}]$ corresponds to an upward airflow on the windward face while a downward airflow at the leeward face, and vice versa for a negative $\mathrm{Re}[\widehat{w}]$. At the wave surface, $\mathrm{Re}[\widehat{w}]$ is driven by the wave kinematics through the boundary condition (30).

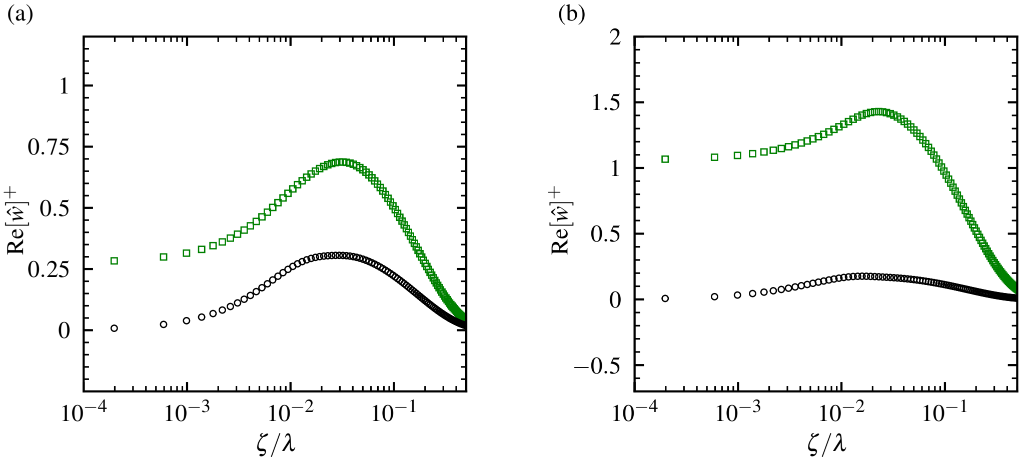

Figure 10: Comparison of $\mathrm{Re}[\widehat{w}]$ solved from the viscous linearised equation (27) with (□) and without (○) the effect of the wave kinematics for the opposing wave cases: (a) WOW01 and (b) WOW04. The superscript '+' denotes normalisation by u_τ.

Figure 9(b) shows that the arising of $\mathrm{Re}[\widehat{w}]$ can be accurately described by the viscous linearised equation (27), suggesting the negligible effect of the nonlinear forcing, i.e. the wave-correlated turbulence stress $\widetilde{\tau}_{ij}$ and the wave-correlated wave-induced stress $\widetilde{\tau}_{ij}^w$ (22), compared with the wave-induced advection and viscous stress, in affecting $\mathrm{Re}[\widehat{w}]$. While the arising of $\mathrm{Re}[\widehat{w}]$ is a quasi-linear process, it exhibits rather different behaviours between the opposing and following wave conditions: in the following wave case, $\mathrm{Re}[\widehat{w}]$ is weak and alternates its sign across the critical height, while in the opposing wave cases, $\mathrm{Re}[\widehat{w}]$ has a large magnitude and maintains a positive value throughout the wave boundary layer (figure 9b).

We found that for the opposing waves, the wave kinematics play an important role in generating the large-magnitude $\mathrm{Re}[\widehat{w}]$. Figure 10 depicts a comparison of $\mathrm{Re}[\widehat{w}]$ solved from the viscous linearised equation (27) with and without (by setting $u_s = w_s = 0$) the effect of the wave kinematics for the opposing wave cases WOW01 and WOW04. The results show that without the effect of the wave kinematics, $\mathrm{Re}[\widehat{w}]$

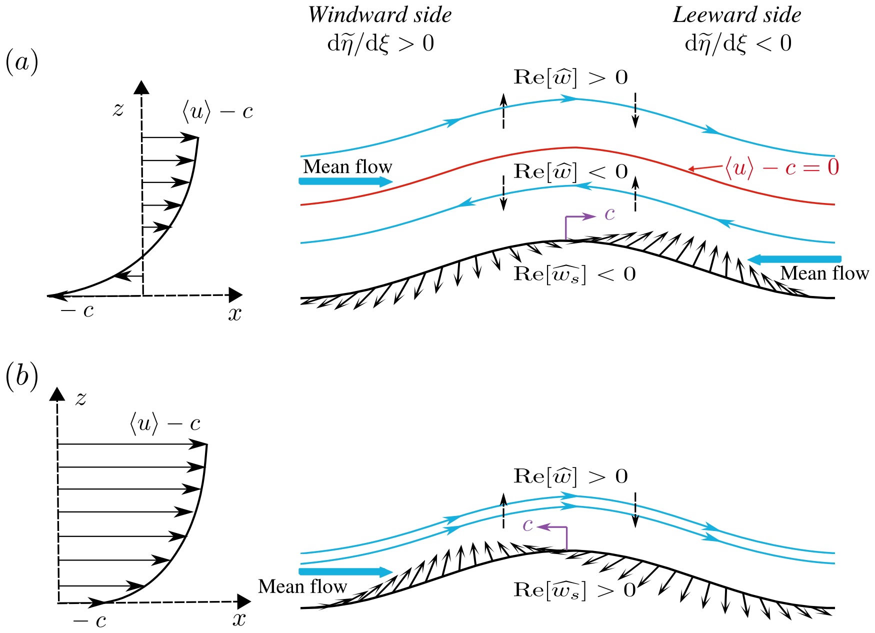

Figure 11: Sketch of streamline perturbation induced by $\mathrm{Re}[\widehat{w}]$ in the frame travelling with the surface wave under the (a) following-wave and (b) opposing-wave conditions. In the figure, the vectors on the wave surface are the wave orbital velocity and w_s is its vertical component. Note that $\mathrm{Re}[\widehat{w}]$ is the real part of the Fourier coefficient of the wave-induced vertical velocity $\widetilde{w}$ (36). The windward side and leeward side are named based on the wind direction viewed in the frame fixed on the Earth.

becomes much smaller for both wave speeds, suggesting that the strong $\mathrm{Re}[\widehat{w}]$ is related to the wave orbital velocity. By contrast, under the following wave condition, the wave kinematics do not cause a strong $\mathrm{Re}[\widehat{w}]$ in the airflow as shown in figure 9(b).

To explain the different effects of the wave kinematics between following and opposing wave conditions, we sketch the streamline perturbation associated with $\mathrm{Re}[\widehat{w}]$ in the frame travelling with the wave in figure 11. In the wind-following-wave case sketched in figure 11(a), below the critical height, because $\langle u \rangle - c < 0$, the wind velocity is in the $-x$ direction and the airflow is blocked by the wave at the leeward side (named based on the wind direction viewed in the fixed frame on the Earth) and needs to go upward along the wave surface. Meanwhile, the wave orbital velocity induces an upward airflow at the leeward face by (30): $\mathrm{Re}[\widehat{w}](\zeta = 0) = \mathrm{Re}[\widehat{w_s}] = -akc/2 < 0$ owing to $c > 0$. This upward air motion at the leeward side (corresponding to $\mathrm{Re}[\widehat{w}] < 0$) caused by the wave orbital velocity plays an important role in pushing up the air. Because the relative wind speed $c - \langle u \rangle$ decreases away from the wave surface to zero at the critical height, a negative wind shear arises, which damps the airflow perturbation induced by the wave orbital velocity, and the perturbation becomes zero at the critical height, as illustrated by the profile of the following wave case in figure 9(b). Above the critical height, although a positive $\mathrm{Re}[\widehat{w}]$ is generated by the blocking of the airflow at the windward face of the wave because $\langle u \rangle - c > 0$, it is not directly related to the wave kinematics.

On the contrary, in the wind-opposing-wave case sketched in figure 11(b), because $\langle u \rangle - c > 0$ such that the critical height is not present, the blocking of the airflow always takes place at the windward side of the wave. Concurrently, the wave orbital velocity induces an upward motion at the windward side: $\mathrm{Re}[\widehat{w}](\zeta = 0) = \mathrm{Re}[\widehat{w_s}] = -akc/2 > 0$ owing to $c < 0$. Because the relative wind speed $\langle u \rangle - c$ increases away from the wave surface, a positive wind shear arises, which amplifies the airflow perturbation induced by the wave orbital velocity all the way up until the mean wind shear vanishes. Consequently, $\mathrm{Re}[\widehat{w}]$ maintains a positive value and has a large magnitude throughout the wave boundary layer. This explains the results of the opposing wave cases in figure 9(b).

Nonlinear dynamics for $\mathrm{Im}[\widehat{w}]$ near wave surface Under the opposing wave condition, while the viscous linear model quantitatively explains the arising of strong

$\mathrm{Re}[\widehat{w}]$, it underestimates the weak $\mathrm{Im}[\widehat{w}]$ as shown in figure 9(c). Unlike $\mathrm{Re}[\widehat{w}]$, with which the airflow changes the vertical velocity direction on the two sides of the wave crest, $\mathrm{Im}[\widehat{w}]$ corresponds to either an upward or a downward air motion near the wave crest on both sides, which can be seen from its contribution to $\widetilde{w}$ in the physical space (15)

$$\widetilde{w} = -2\,\mathrm{Im}[\widehat{w}]\sin(k\xi) = -2\,\mathrm{Im}[\widehat{w}]\widetilde{\eta}/a, \tag{37}$$

where $\widetilde{\eta} = a\sin(k\xi)$ has been applied. Considering that $\widetilde{\eta} > 0$ near the wave crest, we see that a negative $\mathrm{Im}[\widehat{w}]$ corresponds to an upward airflow there, and vice versa for a positive $\mathrm{Im}[\widehat{w}]$. Another difference from the $\mathrm{Re}[\widehat{w}]$-associated airflow is that the $\mathrm{Im}[\widehat{w}]$-associated air motion is not initiated by the wave orbital velocity at the surface, which can be seen from the boundary condition (31), but only by the viscous stress and nonlinear forcing in the vicinity of the wave surface as discussed subsequently.

The underestimation of $\mathrm{Im}[\widehat{w}]$ by the viscous linear solution indicates that the viscous stress is not the only crucial mechanism for its generation and that the effect of the nonlinear forcing, i.e. the wave-correlated turbulent stress $\widetilde{\tau}_{ij}$ and the wave-correlated wave-induced stress $\widetilde{\tau}^{w}_{ij}$, can be important too. In turbulent wind following slow water waves, it has been shown theoretically that the wave-correlated turbulent stress $\widetilde{\tau}_{ij}$ can result in the generation of $\mathrm{Im}[\widehat{w}]$ in the air (Belcher & Hunt, 1993). In their study, Belcher & Hunt (1993) used the mixing-length turbulence model to solve the asymptotic equations for the wave-coherent velocity and found that $\widetilde{\tau}_{ij}$ affects $\mathrm{Im}[\widehat{w}]$ significantly near the wave surface. The height of this turbulent stress-influenced region is very small compared with the wavelength of the surface wave, suggesting that $\mathrm{Im}[\widehat{w}]$ is strongly affected by the nonlinear forcing only in the vicinity of the wave surface. Compared with $\widetilde{\tau}_{ij}$, the effect of $\widetilde{\tau}^{w}_{ij}$ has received less attention and was neglected in the previous asymptotic studies (e.g., Jacobs, 1987; Belcher & Hunt, 1993; Miles, 1993, 1996).

To show the effect of the nonlinear forcing on generating $\mathrm{Im}[\widehat{w}]$ in wind opposing waves, we examine the vertical momentum budget of wave-coherent airflow, which reads

$$(\langle u\rangle - c)\frac{\partial \widetilde{w}}{\partial \xi} + \frac{\partial \widetilde{p}}{\partial \zeta} - \nu\left(\frac{\partial^2 \widetilde{w}}{\partial \xi^2} + \frac{\partial^2 \widetilde{w}}{\partial \zeta^2}\right) + \frac{\partial \widetilde{\tau}_{3j}}{\partial \xi_j} + \frac{\partial \widetilde{\tau}^w_{3j}}{\partial \xi_j} = 0 + O((ak)^2). \tag{38}$$

Equation (38) is the vertical component of the full momentum equations for wave-coherent airflow (22), with the advection, viscous, and pressure terms simplified according to (25). Taking the imaginary part of (38) with respect to $(\langle u\rangle - c)\partial\widetilde{w}/\partial\xi$, we obtain the equation governing $\mathrm{Im}[\widehat{w}]$ as

$$\underbrace{k(\langle u\rangle - c)\,\mathrm{Im}[\widehat{w}]}_{Adv} \underbrace{-\frac{\mathrm{d}\,\mathrm{Re}[\widehat{p}]}{\mathrm{d}\zeta}}_{Pre} \underbrace{-\nu\left(k^2\,\mathrm{Re}[\widehat{w}] - \frac{\mathrm{d}^2\,\mathrm{Re}[\widehat{w}]}{\mathrm{d}\zeta^2}\right)}_{Vis}$$
$$\underbrace{+k\,\mathrm{Im}[\widehat{\tau}_{31}] - \frac{\mathrm{d}\,\mathrm{Re}[\widehat{\tau}_{33}]}{\mathrm{d}\zeta}}_{Tub} \underbrace{+k\,\mathrm{Im}[\widehat{\tau}^w_{31}] - \frac{\mathrm{d}\,\mathrm{Re}[\widehat{\tau}^w_{33}]}{\mathrm{d}\zeta}}_{Wav} = 0 + O((ak)^2). \tag{39}$$

Here, '*Adv*' is the advection by the wave-coherent velocity, '*Pre*' is the vertical gradient of the wave-induced pressure, and '*Vis*' is the divergence of the wave-induced viscous stress. Note that $\mathrm{Im}[\widehat{w}]$ appears in the '*Adv*' term, while $\mathrm{Re}[\widehat{w}]$ is present in the '*Vis*' term so that it can impact $\mathrm{Im}[\widehat{w}]$. The last two groups, '*Tub*' and '*Wav*', represent the nonlinear forcing by the wave-correlated turbulence stress $\widetilde{\tau}_{ij}$ and the wave-correlated wave-induced stress $\widetilde{\tau}^w_{ij}$, respectively.

Calculated from the LES data, the stress terms in (39) are presented in figure 12.

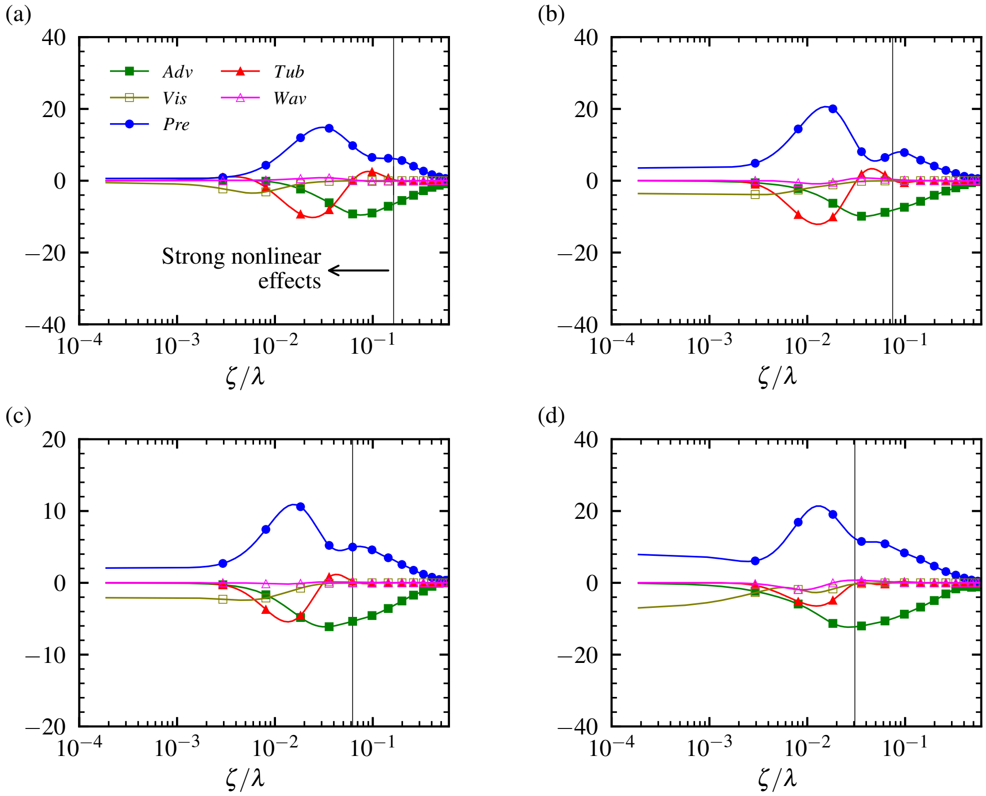

Figure 12: Profiles of the terms in the budget equation (39) for $\mathrm{Im}[\widehat{w}]$, normalised by u_τ^2/λ, for surface wave conditions: (a) WFW01, (b) WOW01, (c) WOW01L, and (d) WOW04. In the figure, the thin black line represents the height of the inner region defined in (40).

As shown, in the four wave cases plotted, the wave boundary layer can be divided into two regions by the thin solid black line in the figure, including a near-surface region, or the inner region, and a faraway region, or the outer region. The line is defined such that the following condition is satisfied above it,

$$|Tub| + |Wav| < 0.05\min(|Adv|, |Pre|). \tag{40}$$

It is shown that in the inner region, the magnitude of the nonlinear forcing, with $\tilde{\tau}_{ij}$ dominating $\tilde{\tau}_{ij}^{w}$, is not negligible compared with that of the wave-induced pressure and advection, suggesting the nonlinear mechanisms for the generation of $\mathrm{Im}[\widehat{w}]$ near the wave surface. In the outer region, as suggested in (40), the magnitude of $\tilde{\tau}_{ij}$ and $\tilde{\tau}_{ij}^{w}$ is small. This combined with the small magnitude of the viscous stress indicates that the wave-induced pressure and advection are in balance with each other, i.e. the inviscid linear dynamics are dominant there.

The predicted inviscid linear behaviour of $\mathrm{Im}[\widehat{w}]$ in the outer layer is verified in figure 13, which compares the inviscid linear solutions of (33) and the LES results in the outer region. To obtain the inviscid linear solutions, we impose the value of $\mathrm{Im}[\widehat{w}]$ at the top of the inner region from the LES data as the Dirichlet boundary condition for the inviscid equation (33), which is then numerically solved in the outer region. As shown in figure 13, the linear solutions and the LES results are almost indistinguishable from each other, indicating the linear behaviour of $\mathrm{Im}[\widehat{w}]$ in the outer layer.

Figure 13 shows that the height of inner region depends more on the wave phase speed than the wave amplitude. The heights of the inner region for cases WFW01,

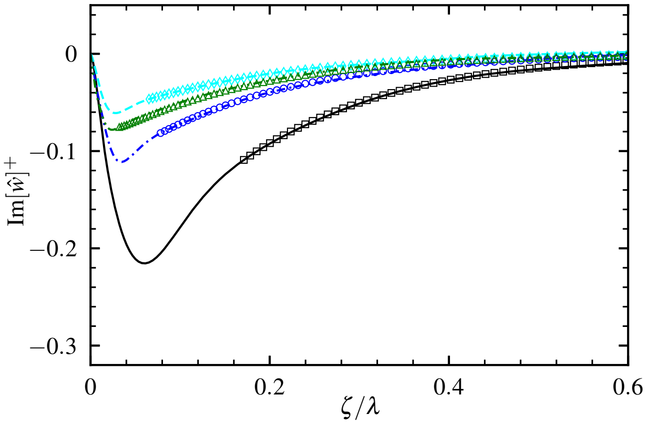

Figure 13: Comparison of $\mathrm{Im}[\widehat{w}]$ profiles in the outer region between the LES results: WFW01 (——), WOW01 (-·-), WOW01L (---), and WOW04 (-···); and the solutions of the inviscid linearised equation (33): WFW01 (□), WOW01 (○), WOW01L(◇), and WOW04 (△). The outer region is defined in (40), indicating that the effect of nonlinear forcing vanishes there.

WOW01, WOW01L, and WOW04 are $\zeta/\lambda = 0.163$, 0.075, 0.065, and 0.031, respectively. This variation of the inner region height can be explained using the timescale argument. As pointed out by Belcher & Hunt (1998), in the turbulent wind following water waves, the height of the inner region is qualitatively determined by the relative magnitude between two timescales, the advection timescale T_A and the Lagrangian timescale T_L. The advection timescale T_A is proportional to the inverse of the mean relative velocity, i.e. $1/(\langle u \rangle - c)$, and it measures how fast the turbulence eddies are distorted and advected. The Lagrangian timescale T_L is proportional to the distance from the wave surface, i.e. ζ, and it quantifies the decorrelation time of the large turbulence eddies. The inviscid region is characterized by $T_A < T_L$, indicating that the turbulence eddies are rapidly distorted. Based on this argument, we attribute the lower inner region height for the opposing wave to the larger mean relative velocity $\langle u \rangle - c$, because $c < 0$, such that the condition $T_A < T_L$ is satisfied at a lower height. The thinner inner region to generate $\mathrm{Im}[\widehat{w}]$ for opposing waves explains the corresponding smaller magnitude of $\mathrm{Im}[\widehat{w}]$ compared with the following wave case.

Although the turbulent stress-influenced region is confined to the proximity of the wave surface, its impact on $\mathrm{Im}[\widehat{w}]$ extends to the entire wave boundary layer because the value of $\mathrm{Im}[\widehat{w}]$ at the top of the inner region sets the boundary condition for $\mathrm{Im}[\widehat{w}]$ in the outer region. This mechanism of how the nonlinear forcing affecting $\mathrm{Im}[\widehat{w}]$ is similar between the wind opposing waves and the wind following slow wave. Hence, the negligence of the turbulent stress by the viscous linear equation (27) leads to its underestimation of the magnitude of $\mathrm{Im}[\widehat{w}]$ in the inner region, resulting in a further underestimation in the outer region, as shown in figure 9(c).

For all of the four wave conditions shown, $\mathrm{Im}[\widehat{w}]$ maintains a negative value. To illustrate the underlying physical processes, we sketch the streamline perturbation induced by $\mathrm{Im}[\widehat{w}]$ in the frame traveling with the surface wave in figure 14. In the wind-following-wave case sketched in figure 14(a), unlike $\mathrm{Re}[\widehat{w}]$ plotted in figure 11(a), the critical height has no direct effect on $\mathrm{Im}[\widehat{w}]$. In particular, near the wave crest, both below and above the critical height, $\mathrm{Im}[\widehat{w}]$ is negative, corresponding to an upward motion to bring up the air blocked by the wave surface. This effect of $\mathrm{Im}[\widehat{w}]$-induced air motion, together with that of the $\mathrm{Re}[\widehat{w}]$-induced airflow as illustrated in figure 11(a), push the air up. Because $\mathrm{Re}[\widehat{w}]$ is not strong enough and thus can only push up part of the blocked air, an appreciable $\mathrm{Im}[\widehat{w}]$ is generated to further lift up the air. On the contrary, in the wind-opposing-wave case sketched in figure 14(b), only a weak negative $\mathrm{Im}[\widehat{w}]$ is generated, as the air blocked by the wave surface is moved up mainly by the strong $\mathrm{Re}[\widehat{w}]$-induced air motion (see figure 11b).

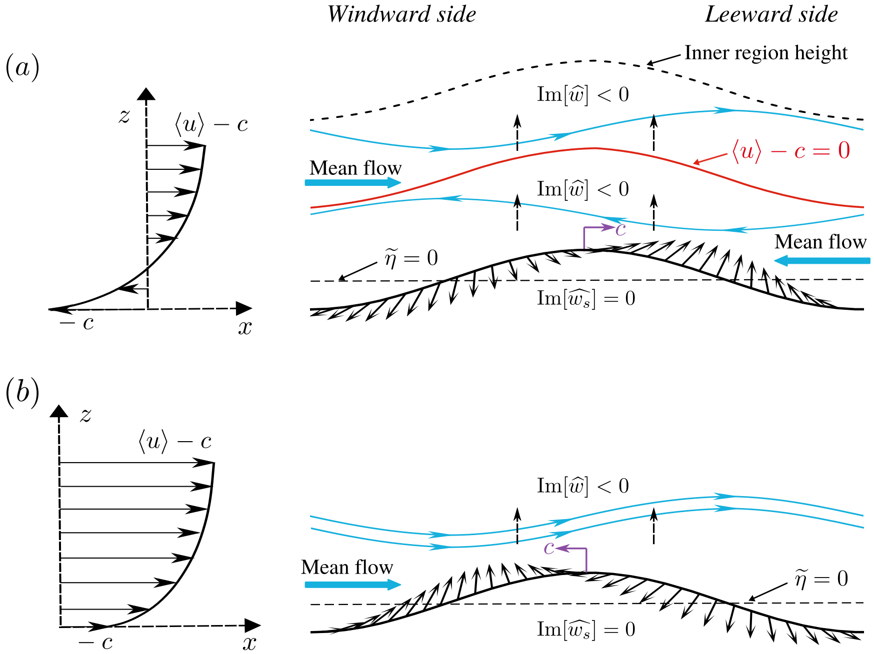

Figure 14: Sketch of the streamline perturbation in the airflow induced by $\mathrm{Im}[\widehat{w}]$ in the frame traveling with the surface wave under the (a) wind-following-wave and (b) wind-opposing-wave condition. Note that $\mathrm{Im}[\widehat{w}]$ is the imaginary part of the Fourier coefficient of the wave-induced vertical velocity $\widetilde{w}$ (37). The windward side and leeward side are named based on the wind direction viewed in the frame fixed on the Earth.

As a summary of this subsection, the wave kinematics induce airflow perturbation at the surface, which is damped out at the critical height of the following wave, but is amplified by the mean wind velocity in the opposing wave cases and results in the seemingly antisymmetric $\widetilde{w}$ in the air. The viscous stress acts in concert with the turbulent stress to cause $\widetilde{w}$ to deviate slightly from a perfect antisymmetry. In the following subsections, we further perform analyses on the effects of the wave kinematics-induced airflow on the streamwise velocity, wave-coherent stress, and pressure in the opposing wave condition.

2.5.2 Wave-induced streamwise velocity $\widetilde{u}$

In this subsection, we examine how the wave-coherent streamwise velocity $\widetilde{u}$ is affected by the wave kinematics, viscous stress, and turbulent stress for the opposing waves, and then explain its spatial structure observed in § 2.3.1. The wave-induced streamwise velocity $\widetilde{u}$ can be obtained using $\widetilde{w}$ through the modified continuity equation (26). With (15), $\widetilde{u}$ is represented as

$$\widetilde{u} = 2|\widehat{u}| \sin\big(k\xi - \phi_{\widetilde{u}\widetilde{\eta}}\big), \tag{41}$$

where $2|\widehat{u}|$ is the magnitude of $\widetilde{u}$ and $\phi_{\widetilde{u}\widetilde{\eta}}$ is the phase difference between $\widetilde{u}$ and $\widetilde{\eta}$. Figure 15 presents the the comparison of $|\widehat{u}|$ (figure 15a), $\mathrm{Re}[\widehat{u}]$ (figure 15b), $\mathrm{Im}[\widehat{u}]$ (figure 15c), and $\phi_{\widetilde{u}\widetilde{\eta}}$ (figure 15d) between the LES results and the solutions of the viscous linearised equation (27) for the opposing wave cases. The comparison between figure 15(a) and (c) shows that the behaviour of $|\widehat{u}|$ is mainly determined by $\mathrm{Im}[\widehat{u}]$, and for both of them the solutions of (27) agree reasonably with the LES results. This

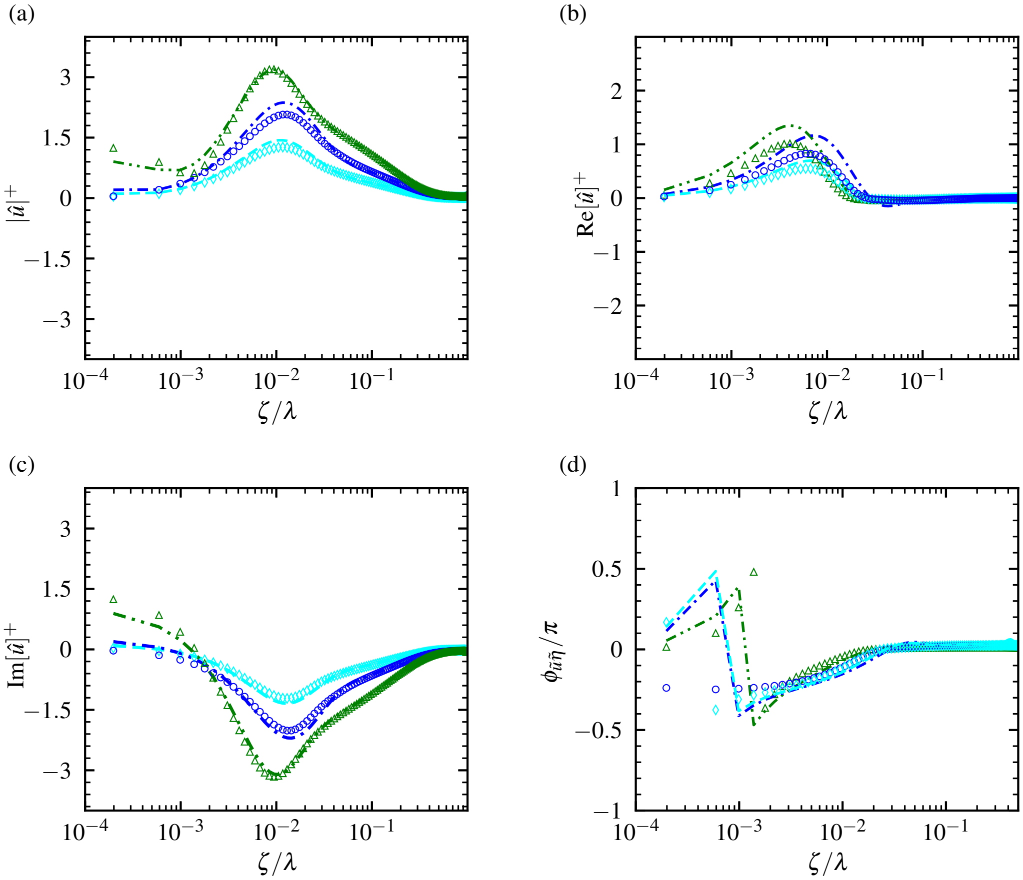

Figure 15: Comparison of (a) $|\widehat{u}|$, (b) $\mathrm{Re}[\widehat{u}]$, (c) $\mathrm{Im}[\widehat{u}]$, and (d) $\phi_{\widetilde{u}\widetilde{\eta}}$ between the LES results: WOW01 (-·-), WOW01L (---), and WOW04 (-··-); and the solutions of the viscous linearised equation (27): WOW01 (○), WOW01L(◇), and WOW04 (△). The superscript '+' denotes normalisation by u_τ.

result is caused by the larger magnitude of $\mathrm{Im}[\widehat{u}]$ than $\mathrm{Re}[\widehat{u}]$, especially for $\zeta/\lambda > 0.03$, as can be seen from the comparison between figure 15(b) and (c), because $\mathrm{Im}[\widehat{u}]$ is associated with the strong $\mathrm{Re}[\widehat{w}]$ as suggested by (26),

$$\mathrm{Im}[\widehat{u}] = \frac{1}{k}\frac{\mathrm{d}\,\mathrm{Re}[\widehat{w}]}{\mathrm{d}\zeta} + \frac{a}{2}g\frac{\mathrm{d}\langle u\rangle}{\mathrm{d}\zeta}. \tag{42}$$

Equation (42) also indicates that following the behaviour of $\mathrm{Re}[\widehat{w}]$, $\mathrm{Im}[\widehat{u}]$ is also related to the flow perturbation by the wave kinematics and controlled by the linear mechanisms. The dominance of $\mathrm{Im}[\widehat{u}]$ also results in $\phi_{\widetilde{u}\widetilde{\eta}} \approx 0$ for $\zeta/\lambda > 0.03$ in both the linear solutions and LES results (figure 15d), which indicates that the wave kinematics-induced airflow results in the symmetry of $\widetilde{u}$ away from the wave surface, consistent with figure 4(b–d).

In the region $\zeta/\lambda < 0.03$, though $|\,\mathrm{Im}[\widehat{u}]| > |\,\mathrm{Re}[\widehat{u}]|$, their magnitudes are comparable, which causes $\phi_{\widetilde{u}\widetilde{\eta}}$ to deviate from zero and consequently $\widetilde{u}$ to be not symmetric near the opposing wave surface (figure 4b–d). To see why a strong $\mathrm{Re}[\widehat{u}]$ arises near the surface, we can obtain the following relation from (26)

$$\mathrm{Re}[\widehat{u}] = -\frac{1}{k}\frac{\mathrm{d}\,\mathrm{Im}[\widehat{w}]}{\mathrm{d}\zeta}, \tag{43}$$

which suggests that $\mathrm{Re}[\widehat{u}]$ is caused by the sharp arising of $\mathrm{Im}[\widehat{w}]$ close to the surface (figure 9c). This mechanism further indicates that $\mathrm{Re}[\widehat{u}]$, or the asymmetry of $\widetilde{u}$ near the wave surface, results from the effects of the viscous stress and turbulent stress. Same as $\mathrm{Im}[\widehat{w}]$ is underpredicted by the viscous linear model owing to the negligence of the turbulence stress (see § 2.5.1), $\mathrm{Re}[\widehat{u}]$ is underestimated too as shown in figure 15(b).

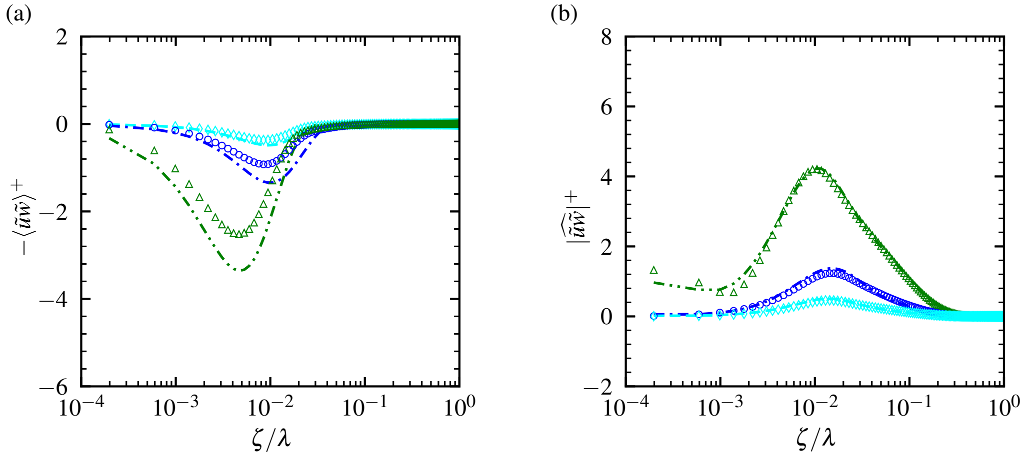

Figure 16: Comparison of (a) $-\langle \widetilde{u}\widetilde{w}\rangle$ and (b) $|\widehat{\widetilde{u}\widetilde{w}}|$ between the LES results: WOW01 (-·-), WOW01L (---), and WOW04 (-···); and the solutions of the viscous linearised equation (27): WOW01 (○), WOW01L(◇), and WOW04 (△). The superscript '+' denotes normalisation by u_τ^2.

In summary of this subsection, we found that the seemingly symmetric distribution of $\widetilde{u}$ away from the opposing wave surface is caused by the flow perturbation related to the wave kinematics. Near the surface, the viscous stress and turbulent stress cause $\widetilde{u}$ to deviate from the symmetric distribution noticeably.

2.5.3 Wave-induced stress $-\widetilde{u}\widetilde{w}$ and pressure $\widetilde{p}$

In this subsection, we investigate how the wave kinematics, viscous stress, and turbulent stress affect the wave-coherent stress $-\widetilde{u}\widetilde{w}$ and pressure $\widetilde{p}$ in the wind opposing waves. The wave-induced stress $-\widetilde{u}\widetilde{w}$ can be decomposed into a mean part and a wave-coherent part

$$-\widetilde{u}\widetilde{w} = \langle -\widetilde{u}\widetilde{w}\rangle - \widetilde{\widetilde{u}\widetilde{w}} = \langle -\widetilde{u}\widetilde{w}\rangle - (\widehat{\widetilde{u}\widetilde{w}}\mathrm{e}^{\mathrm{i}2k\xi} + \widehat{\widetilde{u}\widetilde{w}}^{*}\mathrm{e}^{-\mathrm{i}2k\xi}), \tag{44}$$

where $\langle -\widetilde{u}\widetilde{w}\rangle$ is the mean of $-\widetilde{u}\widetilde{w}$, and $-\widetilde{\widetilde{u}\widetilde{w}}$ is the wave-coherent part of $-\widetilde{u}\widetilde{w}$, with $-\widehat{\widetilde{u}\widetilde{w}}$ being its Fourier coefficient. In figure 16, we compare $-\langle\widetilde{u}\widetilde{w}\rangle$ and $|\widehat{\widetilde{u}\widetilde{w}}|$ betwen the viscous solutions (27) and LES results for the opposing waves. As shown, $-\langle\widetilde{u}\widetilde{w}\rangle$ (figure 16a) is significant only near the surface, $\zeta/\lambda < 0.03$, because $-\langle\widetilde{u}\widetilde{w}\rangle$ is mainly contributed by the correlation between $\mathrm{Re}[\widehat{u}]$ and $\mathrm{Re}[\widehat{w}]$, and thus is significant only in the region where $\mathrm{Re}[\widehat{u}]$ is appreciable (see figure 15). In other words, $-\langle\widetilde{u}\widetilde{w}\rangle$ is closely related to the asymmetry of $\widetilde{u}$ near the surface and results from the effects of the viscous stress and turbulent stress. Because of the nonlinear mechanism of $\mathrm{Re}[\widehat{u}]$, $\langle -\widetilde{u}\widetilde{w}\rangle$ is slightly underestimated by the viscous model (figure 16a). By contrast, the effect of $|\widehat{\widetilde{u}\widetilde{w}}|$ (figure 16b) can reach a much higher altitude, $\zeta/\lambda \approx 0.5$, because $|\widehat{\widetilde{u}\widetilde{w}}|$ mainly results from the correlation between $\mathrm{Im}[\widehat{u}]$ and $\mathrm{Re}[\widehat{w}]$, and both of them are significant up to $\zeta/\lambda \approx 0.5$. This behaviour explains the alternating positive and negative $-\widetilde{u}\widetilde{w}$ in figure 5. Because of the linear mechanism for $\mathrm{Im}[\widehat{u}]$ and $\mathrm{Re}[\widehat{w}]$, $|\widehat{\widetilde{u}\widetilde{w}}|$ can also be described by the viscous linearised model.

The wave-induced pressure $\widetilde{p}$ can be obtained through the vertical momentum equation (25). With (15), $\widetilde{p}$ is represented as

$$\widetilde{p} = 2|\widehat{p}|\sin\big(k\xi - \phi_{\widetilde{p}\widetilde{\eta}}\big), \tag{45}$$

where $2|\widehat{p}|$ is the magnitude of $\widetilde{p}$ and $\phi_{\widetilde{p}\widetilde{\eta}}$ is the phase difference between $\widetilde{p}$ and $\widetilde{\eta}$. Figure 17 compares $|\widehat{p}|$ (figure 17a), $\mathrm{Re}[\widehat{p}]$ (figure 17b), $\mathrm{Im}[\widehat{p}]$ (figure 17c), and $\phi_{\widetilde{p}\widetilde{\eta}}$ (figure 17d) between the LES results and the solutions of the viscous linearised equation (27) for the three opposing waves. Through comparing figure 17(a) and (c), we see that $|\widehat{p}|$ is contributed mainly by the large-magnitude $\mathrm{Im}[\widehat{p}]$, which is related to

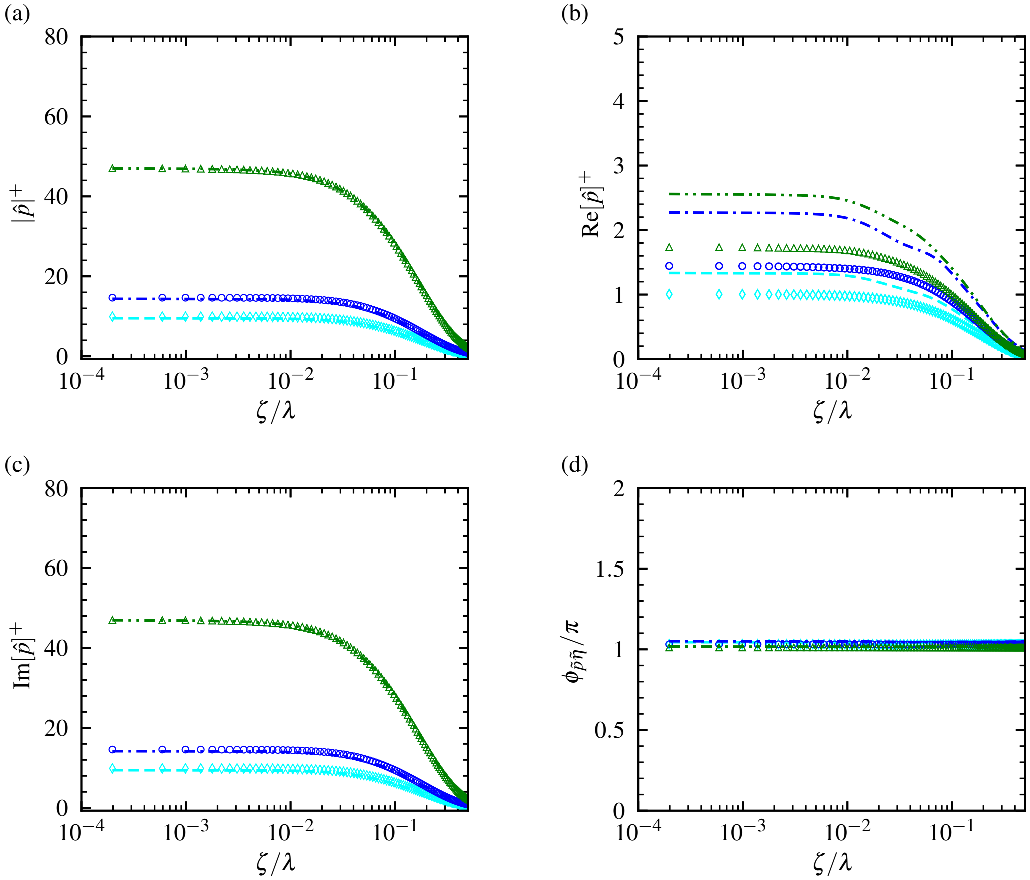

Figure 17: Comparison of (a) $|\widehat{p}|$, (b) $\mathrm{Re}[\widehat{p}]$, (c) $\mathrm{Im}[\widehat{p}]$, and (d) $\phi_{\widetilde{p}\widetilde{\eta}}$ between the LES results: WOW01 (-·-), WOW01L (- - -), and WOW04 (-···); and the solutions of the viscous linearised equation (27): WOW01 (○), WOW01L(◇), and WOW04 (△). The superscript '+' denotes normalisation by $\rho_a u_\tau^2$. Note the scale difference between (b) and (c).

the wave kinematics-induced $\mathrm{Re}[\widehat{w}]$

$$\mathrm{Im}[\widehat{p}]\big|_{\zeta} \approx \int_{\zeta}^{\lambda} k(\langle u\rangle - c)\,\mathrm{Re}[\widehat{w}]\mathrm{d}\zeta, \tag{46}$$

and thereby is controlled by the linear mechanism. As a result, the linear solutions of $|\widehat{p}|$ and $\mathrm{Im}[\widehat{p}]$ agree with the LES results. The derivation of (46) is given in appendix E. Equation (46) also explains why $\widetilde{p}$ is significantly stronger under the opposing wave condition than the following wave condition (figure 6): in the wind opposing wave, $\mathrm{Re}[\widehat{w}]$ is much stronger, and $\langle u\rangle - c$ is also larger owing to $c < 0$, resulting in a significantly larger $\mathrm{Im}[\widehat{p}]$. Meanwhile, because $\mathrm{Im}[\widehat{p}]$ dominates $\mathrm{Re}[\widehat{p}]$ throughout the boundary layer, $\phi_{\widetilde{p}\widetilde{\eta}}$ is close to π for both the linear solutions and LES results (figure 17d). Therefore, the symmetry of $\widetilde{p}$ in the wind opposing waves (figure 6b–d) is explained by the wave kinematics-induced airflow.

In the wind opposing waves, only the out-of-phase pressure $\mathrm{Re}[\widehat{p}]$ can generate form drag on the wave surface. Starting from (25) and with the derivation given in appendix E, we can obtain the following relation between $\mathrm{Re}[\widehat{p}]$ and $\mathrm{Im}[\widehat{w}]$

$$\mathrm{Re}[\widehat{p}]\big|_{\zeta} \approx \int_{\zeta}^{\lambda} -k(\langle u\rangle - c)\,\mathrm{Im}[\widehat{w}]\mathrm{d}\zeta, \tag{47}$$

which suggests that although $\mathrm{Im}[\widehat{w}]$ is small for the opposing waves, it can still result in appreciable $\mathrm{Re}[\widehat{p}]$ to cause a form drag on the wave surface owing to the large $\langle u\rangle - c$, despite that $\mathrm{Im}[\widehat{w}]$ is concealed by its strong out-of-phase counterpart $\mathrm{Re}[\widehat{w}]$. Because of the underestimation of $\mathrm{Im}[\widehat{w}]$ by the linear model, $\mathrm{Re}[\widehat{p}]$ is also underestimated as shown in figure 17(b).

As a conclusion of § 2.5, we would like to emphasize that in the wind opposing waves, the dominant components of $\widetilde{w}$, $\widetilde{u}$, $\widetilde{p}$, i.e. $\mathrm{Re}[\widehat{w}]$, $\mathrm{Im}[\widehat{u}]$, and $\mathrm{Im}[\widehat{p}]$, respectively, and the wave-coherent part of $-\widetilde{u}\widetilde{w}$, i.e. $-\widetilde{\widetilde{u}\widetilde{w}}$, are caused by the linear interaction between the wave kinematics-induced airflow at the surface and the mean wind speed $\langle u \rangle - c$. The effects of turbulent stress have two aspects. First, the turbulent stress is important to maintain a logarithmic profile of $\langle u \rangle$ and thus a strong shear, which is important for the amplification of airflow perturbation initiated by the wave kinematics. Second, the turbulent stress, in concert with the viscous stress, result in an asymmetry in $\widetilde{u}$ and $\widetilde{w}$, which is crucial for the strong mean wave-coherent stress $\langle -\widetilde{u}\widetilde{w} \rangle$ and an out-of-phase pressure near the wave surface to generate the form drag.

2.6 Wave attenuation rate

In this section, we investigate the attenuation rate of water waves due to the forcing by the opposing wind. As reviewed by Belcher & Hunt (1998) and Sullivan & McWilliams (2010), the wind impacts the evolution of a wave mainly through exerting a form drag on the wave surface, which is defined as

$$F_p = \frac{1}{\lambda} \int_0^\lambda \frac{\widetilde{p}}{\rho_a u_\tau^2} \frac{\mathrm{d}\widetilde{\eta}}{\mathrm{d}x} \mathrm{d}x = \frac{ak\,\mathrm{Re}[\widehat{p}]|_{\zeta=0}}{\rho_a u_\tau^2}. \tag{48}$$

The resultant non-dimensional wave attenuation rate γ/f under an opposing wind is (Li *et al.*, 2000; Donelan *et al.*, 2006)

$$\frac{\gamma}{f} = -\frac{1}{Ef}\frac{\mathrm{d}E}{\mathrm{d}t} = -2\pi \frac{\rho_a}{\rho_w} \beta \left(\frac{u_\tau}{c} \right)^2, \qquad \text{where } \beta = -\frac{2F_p}{(ak)^2}. \tag{49}$$

Here, γ and f are the dimensional wave attenuation rate and the wave frequency, respectively, $E = \rho_w g\eta^2$ is the wave energy density, ρ_w is the water density, and β is the wave attenuation rate parameter. The values of γ/f calculated from (48) and (49) using the pressure data from the present LES are compared with the results of parameterizations based on the measurements of opposing wave-induced airflow (Young & Sobey, 1985; Donelan, 1999) and evolution of wave field (Peirson *et al.*, 2003; Mitsuyasu & Honda, 1982), and the numerical simulations using the RANS equations (Harris *et al.*, 1995; Cohen, 1997).

Figure 18 compares the wave attenuation rate γ/f as a function of the inverse wave age $|u_\tau/c|$ between the present and previous studies. Overall, the values of γ/f calculated using the air pressure in the present LES results are compared reasonably well with the previous studies, especially the parameterization of Mitsuyasu & Yoshida (2005) and the numerical simulations of Harris *et al.* (1995) and Cohen (1997). The parameterization of Young & Sobey (1985) with $ak = 0.08$ is smaller than most of the studies shown in the figure, while their result with $ak = 0.15$ is comparable to the other studies. The parameterization of Peirson *et al.* (2003) shows a higher γ/f than most of the results in the figure, which is likely caused by the contribution to the wave decay by the interaction between the wave and wind-induced current at the water side in their study, as suggested by Peirson *et al.* (2003). In addition, the wave attenuation rates in the present LES and the result of Mitsuyasu & Yoshida (2005) have magnitudes comparable with the wave growth rate in the following wind condition measured by Mitsuyasu & Honda (1982), indicating that the timescale of wave decay by an opposing wind is comparable to that of the wave growth by a following wind. Figure 18 also shows the values of γ/f estimated using the pres-

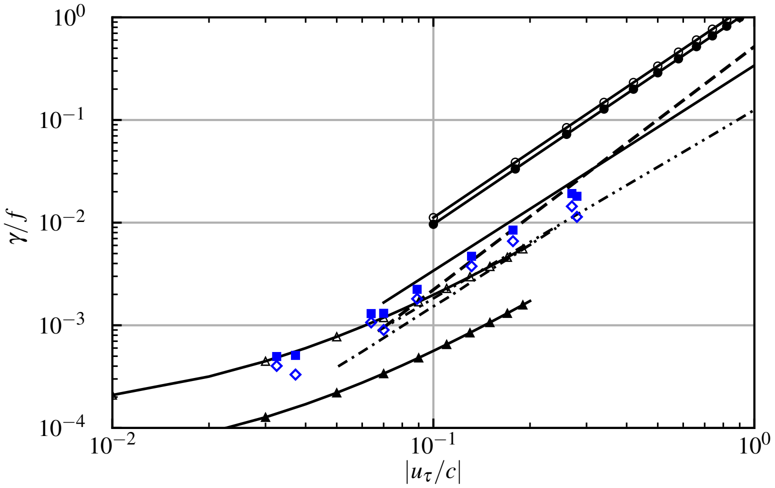

Figure 18: Comparison of non-dimensional wave attenuation rate γ/f as a function of the inverse wave age $|u_\tau/c|$ between the present and previous studies. The filled squares (■) and open diamonds (◇) denote the LES results and the solutions of the viscous linearised equation (27), respectively. The lines with triangles are the results of Young & Sobey (1985) $\gamma/f = 1.4\pi(ak)^2\rho_a/\rho_w(1-U_\infty/c)^2$ with $ak = 0.15$ (—△—) and $ak = 0.08$ (—▲—), where $U_\infty \approx 30u_\tau$ in their study. The dash-dot (-·-) and dash-dot-dot (-··-) lines show the results of Harris *et al.* (1995) and Cohen (1997), respectively. The lines with circles are the parameterization of Peirson *et al.* (2003) $\gamma/f = 2.275(ak)^{0.238}|u_\tau/c|^{2.112}$ with $ak = 0.15$ (—○—) and $ak = 0.08$ (—●—). The parameterization of Mitsuyasu & Yoshida (2005) $\gamma/f = 0.52|u_\tau/c|^{2.37}$ is plotted with the dashed line (- - -). As a reference, the parameterization of wave growth rate in the following wind $\gamma/f = 0.34(u_\tau/c)^2$ by Mitsuyasu & Honda (1982) is shown using the solid line (—).

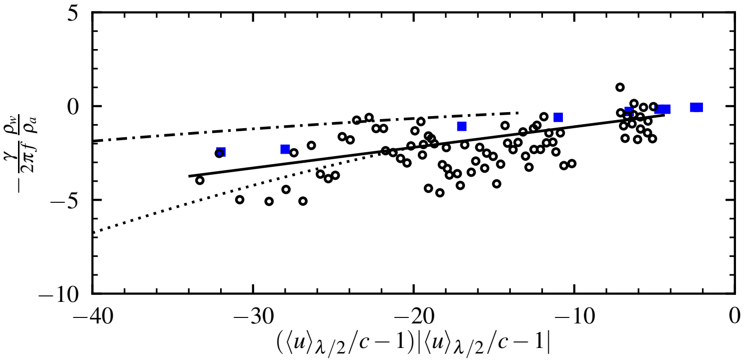

Figure 19: Comparison of wave attenuation rate as a function of $(u_{\lambda/2}/c{-}1)|u_{\lambda/2}/c{-}1|$ between the present LES results and the previous studies. The filled squares (■) and open circles (∘) denote the present LES results and the measurement by Donelan (1999), respectively. The solid line (——) is the parameterization of Donelan (1999) $-\gamma/(2\pi f) = -0.11\rho_a/\rho_w|u_{\lambda/2}/c{-}1|^2$. The dotted (·····) and dashed-dot (-·-) lines are the parameterization of Peirson *et al.* (2003) $\gamma/f = 2.36\times10^{-4}(ak)^{0.240}|u_{\lambda/2}/c{-}1|^{3.265}$ with $ak = 0.08$ and the parameterization of Mitsuyasu & Yoshida (2005) $\gamma/f = 5.8\times10^{-5}|u_{\lambda/2}/c-1|^{3.3}$, respectively.

sure in the solution of the viscous linearised equation (27). Although the estimated γ/f is lower than the LES results because of the negligence of the nonlinear forcing (§ 2.5.3), they still fall in the range of the various studies and have the same trend of variation, suggesting that the pressure asymmetry induced by the viscous stress plays an important role in the wave decay. Figure 19 compares the wave attenuation rate $-\gamma/(2\pi f)\cdot\rho_w/\rho_a$ as a function of $(u_{\lambda/2}/c-1)|u_{\lambda/2}/c-1|$ between the present LES results and the previous studies. As shown, the wave attenuation rates in the LES fall into the measurement data of Donelan (1999) and exhibit a behaviour consistent with the three parameterizations.

To summarize this section, we have shown that the wave attenuation rates in the LES agree reasonably well with the previous studies. The comparison of the theoretical prediction based on the viscous linear model in the present study with the wave attenuation rates in the previous studies suggests that the viscous stress plays an important role in causing the wave decay by inducing a slight pressure asymmetry in the wind opposing a wave.

2.7 Conclusions and discussion

A deep understanding of the interaction between the wind and opposing water waves is important for the study of air–sea interactions under complex oceanic conditions, such as in the presence of tropical cyclones or fronts. To uncover the physical mechanisms underlying the wave-induced airflow by the opposing waves, we have performed LES of turbulent wind following and opposing water waves. To explain the flow dynamics, we have derived the viscous and inviscid linearised equations for the wave-induced velocity in the mapped computational curvilinear coordinate. Below, we provide perspectives on this problem based on the results of the present study.

We have shown that the opposing wave-induced airflow exhibits features very different from that induced by the following wave with the same wave parameters. In particular, our study illustrates that compared with the following wave, the opposing wave induces a significantly stronger vertical velocity perturbation that is out-of-phase with the wave surface, i.e. $\mathrm{Re}[\widehat{w}]$ for the wave form $\widetilde{\eta} = a\sin(k\xi)$, with a much weaker vertical velocity perturbation that is in-phase with the wave surface, i.e. $\mathrm{Im}[\widehat{w}]$, resulting in a nearly antisymmetric spatial distribution of the wave-induced vertical velocity $\widetilde{w}$ in the air. In addition, the modulation on the turbulent statistics in the airflow by the opposing wave is confined to a much thinner region than the following wave.

It is discovered that $\mathrm{Re}[\widehat{w}]$ and $\mathrm{Im}[\widehat{w}]$ are governed by different physical mechanisms. The large-magnitude $\mathrm{Re}[\widehat{w}]$ induced by the opposing waves is driven by the wave orbital velocity at the surface and is amplified by the viscous stress and mean shear in the wind. Consequently, $\mathrm{Re}[\widehat{w}]$ from the LES result agrees well with the solution of the curvilinear viscous linearised equation for different opposing wave parameters. The strong $\mathrm{Re}[\widehat{w}]$ results in a large-amplitude in-phase streamwise velocity perturbation $\mathrm{Im}[\widehat{u}]$ and pressure perturbation $\mathrm{Im}[\widehat{p}]$ in the wind, leading to a seemingly symmetric spatial distribution of the wave-induced streamwise velocity $\widetilde{u}$ (away from the wave surface) and pressure $\widetilde{p}$ observed from the previous studies and the present LES result. On the contrary, $\mathrm{Im}[\widehat{w}]$ is not directly affected by the wave kinematics at the surface. Near the wave surface, $\mathrm{Im}[\widehat{w}]$ is forced by $\mathrm{Re}[\widehat{w}]$ through the viscous and turbulent stresses. The phenomenon that viscous stress affects $\widetilde{w}$ is also observed in the study of wind following fast waves by Akervik & Vartdal (2019). In the outer region, $\mathrm{Im}[\widehat{w}]$ displays an inviscid decay behaviour. In the wind opposing waves, the region for generating $\mathrm{Im}[\widehat{w}]$ is thinner than that in the counterpart following wave case owing to the smaller advection time scale under the former condition, and correspondingly, a weaker $\mathrm{Im}[\widehat{w}]$ is generated by the opposing waves. The weak $\mathrm{Im}[\widehat{w}]$ causes a moderate out-of-phase streamwise velocity perturbation $\mathrm{Re}[\widehat{u}]$ and pressure perturbation $\mathrm{Re}[\widehat{p}]$ in the air, which cause a slight asymmetry in $\widetilde{u}$ and $\widetilde{p}$, respectively. It is found that $\mathrm{Re}[\widehat{u}]$ plays an important role in generating a strong mean wave-induced stress $\langle -\widetilde{u}\widetilde{w} \rangle$ in the proximity of the surface. Away from the wave surface, $\langle -\widetilde{u}\widetilde{w} \rangle$ is small, and the perturbation of the wave-induced stress $-\widetilde{\widetilde{u}\widetilde{w}}$ displays an antisymmetric distribution and can be described by the viscous linearised model.

We have further explained the arising of form drag on the opposing waves, which is caused by Re$[\widehat{p}]$. An important finding is that for the same wave speed, despite the smaller value of Im$[\widehat{w}]$ for the opposing wave than that for the following wave, it can still induce an appreciable Re$[\widehat{p}]$ for the opposing wave, because of the much larger mean relative velocity. While this result is consistent with the intuition as wind is expected to exert form drag on opposing waves to attenuate the waves, our study has illustrated this process systematically with a quantitative model.

At last, we remark that because the dominant effect of opposing waves on the air is to induce strong asymmetric vertical velocity perturbation and symmetric streamwise velocity and pressure perturbation by the interaction between the wave kinematics and mean wind shear, the curvilinear viscous model developed in this study can be used to describe the wave-induced airflow given the mean wind profile. In the case of nonlinear waves, such as a Stokes wave, because the wave orbital velocity is dominated by the solution of the leading order mode, which is the same as the linear wave solution, it is expected to induce airflow perturbation similar to the linear wave. The wave-induced airflow affects the turbulence momentum and scalar fluxes, resulting in their wave-phase-dependent spatial distribution. The parameterization for these processes is important for a variety of applications and should be the subject of study in the future.

3 Wind Following Fast-Moving Water Waves

3.1 Introduction

Turbulent wind–wave interactions play an important role in determining the ocean environment, but they are challenging to predict in the weather and climate modelling because of the complex flow dynamics. The presence of water waves induces flow perturbations to the overlying turbulent wind field, or the wave-induced airflow, which can in turn affect the wave field evolution by causing a form drag on the wave surface and thereby a wind–wave momentum exchange. A deep understanding of the wave-induced airflow is the key to modelling the turbulent wind–wave interactions.

For wind and waves that are aligned in the same direction, based on the direction of wind–wave momentum flux at the water surface, the turbulent wind–wave interactions can be roughly divided into two regimes. When the wave age c/u_τ is low, roughly satisfying $c/u_\tau \lesssim 15$ (c is the wave phase speed and u_τ is the friction velocity in the air), the momentum transfer is from the wind to the wave, which serves as the momentum source for the development of the wave field. Extensive experiments have been performed to quantify the wind–wave momentum transfer and the associated wave growth rate in this case (e.g., Snyder *et al.*, 1981; Hsu, Hsu & Street, 1981; Hsu & Hsu, 1983; Hasselmann & Bsenberg, 1991; Donelan *et al.*, 2005, 2006; Grare *et al.*, 2013*b*). Meanwhile, two mechanisms have been identified as the key factors determining the structure of wave-induced airflow and the resultant momentum exchange. The first mechanism is the effect of the critical layer, defined as the height where the wind speed equals the wave celerity. The theoretical study by Miles (1957) has shown that the inviscid equation governing the wave-induced airflow has a singularity at the critical height, causing a recirculating airflow perturbation in the wave-following frame, which leads to an asymmetric pressure on the wave surface about the wave crest and a form drag on the wave. Later, the critical layer effects on the wave-induced airflow were confirmed in field observations (Hristov, Miller & Friehe, 2003; Grare, Lenain & Melville, 2013*a*). The second mechanism is the wave-induced turbulent stress, defined as the difference between the phase-averaged and the plane-and-time-averaged turbulent stresses in the wind, which was also theoretically found to play an important role in causing the asymmetry of wave-induced velocity and pressure for a from drag to arise (e.g., Knight, 1977; Jacobs, 1987; Van Duin & Janssen, 1992; Belcher & Hunt, 1993; Miles, 1993, 1996). As pointed out by Belcher & Hunt (1998), for slow waves the physical processes affecting the wave-induced airflow and the associated form drag are relatively well understood.

When c/u_τ is high, about $c/u_\tau \gtrsim 15$, the wave speed is comparable to or faster than the mean wind speed, and the direction of wind–wave momentum flux is from the wave to the wind, which has also been observed in the previous simulations and experiments (e.g., Harris, 1966; Smedman, Tjernstrm & Hgstrm, 1994; Mastenbroek, 1996; Drennan, Kahma & Donelan, 1999; Sullivan, McWilliams & Moeng, 2000; Grachev & Fairall, 2001; Hanley & Belcher, 2008; Sullivan *et al.*, 2008; Druzhinin, Troitskaya & Zilitinkevich, 2012; Jiang *et al.*, 2016; Akervik & Vartdal, 2019). The scenario of wave propagating faster than wind can happen when long waves are generated by the nonlinear interaction of shorter waves in a broadband wave field and enter a region with relatively calm wind. These long waves propagate fast according to the dispersion relation for water waves. Over the past several decades, despite the extensive research on wind over fast-moving water waves, there still remain important questions unanswered as summarized below.

First, with the limited amount of theoretical studies on this topic, the mechanisms responsible for the structure of fast wave-induced airflow are not well understood. For low c/u_τ, due to the effects of the critical layer and wave-induced turbulent stress as reviewed above, the wave-induced airflow is asymmetric about the wave crest as visualized in simulations and experiments (e.g., Sullivan *et al.*, 2000; Yang & Shen, 2010; Druzhinin *et al.*, 2012; Buckley & Veron, 2016). However, for high c/u_τ, the above-cited studies have shown that the wave-induced velocity and pressure exhibit a nearly symmetric or antisymmetric spatial distribution. The different features of the wave-induced airflow between low and high c/u_τ indicate that the fast wave-induced airflow is controlled by a mechanism different from that for slow waves, which is illustrated in the present study.

Second, previous studies have shown that the dominant mechanism producing the form drag on the wave surface may change as the wave speed increases in the high c/u_τ condition. Specifically, under the condition $c/u_\tau \lesssim 34$, Cohen (1997) modelled the wave-induced turbulent stress using a damped mixing-length model and found that it can cause a form drag on the water surface. Later, based on the analysis of the wall-resolved LES data of turbulent wind over fast waves, Akervik & Vartdal (2019) found that as c/u_τ approaches 36, the effects of wave-induced viscous stress on the form drag become increasingly more significant, whereas the effects of wave-induced turbulent stress decreases. These studies suggest that as c/u_τ increases, the dominant mechanism for form drag transits from wave-induced turbulent stress to wave-induced viscous stress, but the occurrence of this transition is still not fully understood. More importantly, the mechanism for wave-induced viscous stress to generate the form drag has not been investigated systematically.

Third, there still lacks high-fidelity simulation data to confirm the dominant role of wave-induced viscous stress in producing the form drag for $c/u_\tau \gtrsim 36$. The condition $c/u_\tau \gtrsim 36$ is a common scenario in turbulent wind–wave interactions. For example, Hanley & Belcher (2010) pointed out that in a broadband wave field, the peak wave speed can be as large as 2.8 times of the 10-m wind speed, roughly corresponding to $c \simeq 72u_\tau$. Although there have been wall-modeled LES studies in which the wave age lies in the range of $c/u_\tau \gtrsim 36$ (e.g., Sullivan *et al.*, 2008; Jiang *et al.*, 2016), the viscous sublayer is parameterized instead of being resolved in those studies and thus the effects of wave-induced viscous stress could not be examined. Therefore, direct numerical simulation (DNS) and wall-resolved LES of wind over waves for high wave age are in critical need.

Based on the review above, the present study aims to first expand the high-fidelity dataset of turbulent wind over fast waves to wave ages higher than what are in the literature, and secondly to elucidate the mechanisms for the fast wave-induced airflow and the associated form drag (with its signed changed for high c/u_τ) on the water surface. We perform wall-resolved LES of turbulent wind over fast-moving water waves. We also theoretically investigate the mechanisms for fast wave effects on the wind based on the curvilinear linear models of wave boundary layer, including the non-orthogonal viscous model developed in our study for wind opposing waves in § 2 and a new orthogonal viscous model developed in the present study of § 3. The wall-resolved LES can achieve Reynolds numbers higher than DNS, but it still resolves the viscous sublayer of airflow without resorting to parameterizations of surface roughness and stress. The fast wave-induced airflow is extracted from the LES data and compared with the solutions of the linear models to illustrate the underlying mechanisms. We remark that while the present study in § 3 and the study in § 2 use the same LES code, the physical problems studied are drastically different. In § 2, we focus on the condition in which the directions of wind and wave are opposite with each other, whereas in § 3 they are aligned. More importantly, the behaviours of wave-induced airflow and the underlying mechanisms revealed are significantly different between these two studies, as summarized in § 3.6.

The remainder of § 3 is organised as follows. The numerical method is introduced in § 3.2. Based on the LES data, the features and order of magnitude of the wave effects on the airflow are examined § 3.3. Then in § 3.4, we develop a linear analysis framework for the wave effects, based on which the mechanisms of the wave-induced airflow and the wind–wave momentum flux are elucidated in § 3.5. As last, the conclusions and discussion are given in § 3.6.

3.2 Numerical method

To obtain the three-dimensional turbulent wind field, we perform wall-resolved LES of wind turbulence over prescribed water waves. The LES solves the filtered incompressible Navier–Stokes (NS) equations for air motions,

$$\frac{\partial u_j}{\partial x_j} = 0, \tag{50}$$

$$\frac{\partial u_j}{\partial t} + \frac{\partial (u_j u_m)}{\partial x_m} = -\frac{1}{\rho_a}\frac{\partial p}{\partial x_j} - \frac{\partial \tau^d_{jm}}{\partial x_m} + \nu \frac{\partial^2 u_j}{\partial x_m \partial x_m}, \tag{51}$$

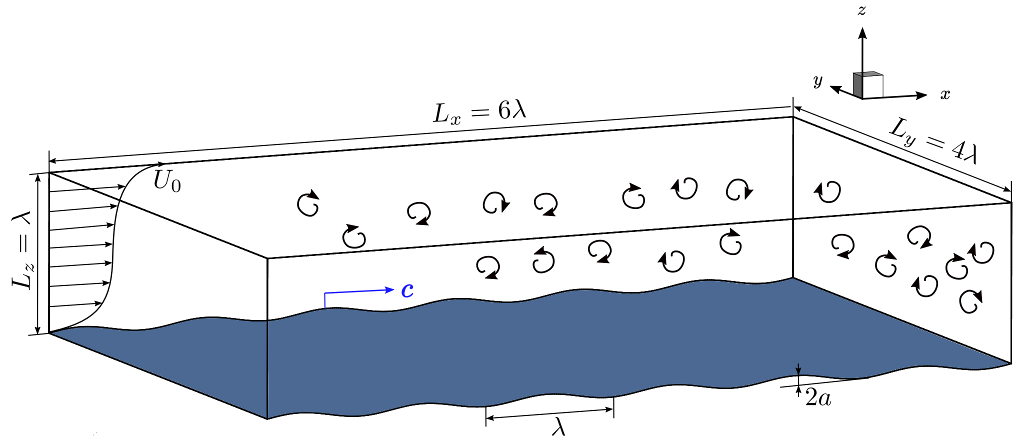

Figure 20: Sketch of the configuration of LES of wind over water wave. The turbulent wind field is driven by a constant velocity U_0 at the top of the computational domain, with the Dirichlet boundary condition applied at the wave surface. Periodic boundary conditions are applied in the horizontal directions. The surface wave propagates in x-direction, with a wavelength λ, an amplitude a, and a phase speed c.

where x, y, and z denote the Cartesian coordinates in the streamwise, spanwise, and vertical directions, respectively, as illustrated in figure 20, $u_j(j = 1, 2, 3) = (u, v, w)$ is the filtered velocity in LES at the grid scale, p is the filtered modified pressure, τ^d_{jm} is the trace-free part of the subgrid-scale (SGS) stress tensor, ρ_a is the density of air, and ν is the air kinematic viscosity. At the water surface, a progressive water wave is imposed as the Dirichlet boundary condition for the airflow, $u_i(z = \eta) = (u_s, v_s, w_s)$, where η is the surface wave elevation and (u_s, v_s, w_s) is the orbital velocity of the wave at the water surface, given as

$$\eta(x, y, t) = a \sin k(x - ct), \tag{52}$$

$$u_s(x, y, z, t) = akc \sin k(x - ct), \tag{53}$$

$$v_s(x, y, z, t) = 0, \tag{54}$$

$$w_s(x, y, z, t) = -akc \cos k(x - ct), \tag{55}$$

where a is the amplitude of the surface wave, $k = 2\pi/\lambda$ is its wavenumber, λ is its wavelength, and c is its phase speed. In (52)–(55), an Airy wave solution is adopted. In the case of nonlinear waves, such as a Stokes wave, the effect of nonlinearity by the higher harmonics is of $O((ak)^2)$. In the linear analysis of the wave-induced airflow performed in later sections, the $O((ak)^2)$ terms in the governing equations are omitted. As explained in § 2, to be consistent we only consider the dominant Fourier component in the water wave solution.

The LES solver employs a boundary-fitted moving grid that follows the instantaneous wave surface at each time step. To discretize and numerically solve the governing equations (50) and (51), the irregular physical domain (x, y, z, t) above the wave is transformed to a rectangular computational domain (ξ, ψ, ζ, τ) through the following algebraic mapping,

$$\tau = t, \qquad \xi = x, \qquad \psi = y, \qquad \zeta = z + g(\zeta)\eta, \qquad \text{where } g(\zeta) = \frac{\zeta}{L_z} - 1. \tag{56}$$

Here, L_z is the mean physical domain height and $g(\zeta)$ denotes the transformation function. The index notation is adopted to denote the physical and computational coordinates as $x_j(j = 1,2,3) = (x,y,z)$ and $\xi_j(j = 1,2,3) = (\xi,\psi,\zeta)$, respectively. The Jacobian matrix corresponding to the above transformation is

$$\mathbf{J} = \begin{bmatrix} \dfrac{\partial \xi}{\partial x} & \dfrac{\partial \xi}{\partial y} & \dfrac{\partial \xi}{\partial z} \\ \dfrac{\partial \psi}{\partial x} & \dfrac{\partial \psi}{\partial y} & \dfrac{\partial \psi}{\partial z} \\ \dfrac{\partial \zeta}{\partial x} & \dfrac{\partial \zeta}{\partial y} & \dfrac{\partial \zeta}{\partial z} \end{bmatrix} = \begin{bmatrix} 1 & 0 & 0 \\ 0 & 1 & 0 \\ \dfrac{g\eta_\xi}{1-g_\zeta\eta} & \dfrac{g\eta_\psi}{1-g_\zeta\eta} & \dfrac{1}{1-g_\zeta\eta} \end{bmatrix}, \tag{57}$$

where $g_\zeta = \mathrm{d}g/\mathrm{d}\zeta$. Because of the surface wave motion, the transformation (56) varies with time, resulting in a transformation of time derivative between the computational space and the physical space

$$\frac{\partial}{\partial t} = \frac{\partial}{\partial \tau} + \frac{\partial \xi_j}{\partial t}\frac{\partial}{\partial \xi_j} = \frac{\partial}{\partial \tau} + \frac{\partial \zeta}{\partial t}\frac{\partial}{\partial \zeta}, \quad \text{where } \frac{\partial \zeta}{\partial t} = \frac{g\eta_\tau}{1-g_\zeta\eta}. \tag{58}$$

The transformed LES equations in the computational space read

$$J_{pj}\frac{\partial u_j}{\partial \xi_p} = 0, \tag{59}$$

$$\frac{\partial u_j}{\partial \tau} + \delta_{p3}\frac{\partial \zeta}{\partial t}\frac{\partial u_j}{\partial \xi_p} + J_{lp}\frac{\partial (u_j u_p)}{\partial \xi_l} = -\frac{J_{lj}}{\rho_a}\frac{\partial p}{\partial \xi_l} + J_{lp}\frac{\partial \tau^d_{jp}}{\partial \xi_l} + \nu J_{np}\frac{\partial}{\partial \xi_n}\left(J_{lp}\frac{\partial u_j}{\partial \xi_l}\right), \tag{60}$$

where J_{lp} is the (l,p) entry of the mapping matrix $\mathbf{J}$ and δ_{lm} is the Kronecker delta. The transformd LES equations (59) and (60) are discretized and solved in the rectangular computational space. In the $(\xi-\psi)$ plane, a Fourier-series-based pseudo-spectral method is used for discretization with evenly spaced grid points. In the ζ-direction, a second-order finite difference method is employed with grid points clustered near the

c/U_0	ak	$u_\tau/U_0 \times 10^2$	c/u_τ	$c/U_{\lambda/2}$	$u_\tau\lambda/\nu$	$(\Delta\xi^+, \Delta\psi^+, \Delta\zeta^+_{\min})$
0.1	0.15	2.89	3.46	0.24	867	$(20.32, 13.55, 0.17)$
0.4	0.15	2.60	15.38	0.82	768	$(18.00, 12.00, 0.15)$
0.8	0.15	2.38	33.61	1.52	714	$(16.73, 11.16, 0.14)$
1.0	0.15	2.24	44.64	1.83	672	$(15.75, 10.50, 0.13)$
1.2	0.15	2.21	54.30	2.10	663	$(15.54, 10.36, 0.13)$
1.4	0.15	2.10	66.67	2.36	630	$(14.77, 9.84, 0.12)$
0.8	0.10	2.49	32.12	1.56	747	$(17.51, 11.67, 0.15)$
1.0	0.10	2.44	40.98	1.91	732	$(17.16, 11.44, 0.14)$
1.2	0.10	2.38	50.42	2.26	714	$(16.73, 11.16, 0.14)$
1.4	0.10	2.31	60.61	2.55	693	$(16.24, 10.83, 0.14)$

Table 2: List of LES cases for turbulent wind over progressive water waves. The wind field is discretized with $(N_x, N_y, N_z) = (384, 384, 193)$ grid points in the (ξ, ψ, ζ) directions, respectively. The bulk Reynolds number $U_0\lambda/\nu$ is prescribed as 30 000 in all of the wave cases, while u_τ, $u_\tau\lambda/\nu$, and the grid resolution in wall units are obtained *a posterior*.

upper and lower boundaries. The SGS stress tensor is calculated using the dynamic Smagorinsky model (Smagorinsky, 1963; Germano *et al.*, 1991; Lilly, 1992). The detailed numerical procedure and extensive validations can be found in our previous studies of turbulent wind–wave interactions (Yang & Shen, 2010, 2011*a*; Yang *et al.*, 2013; Hao & Shen, 2019).

As sketched in figure 20, the turbulent wind is driven by an external velocity at the top of the simulation domain, (u, v, w)=(U_0, 0, 0), which has been a canonical setup in the simulations of turbulent airflows over surface waves (e.g., Sullivan *et al.*, 2000; Druzhinin *et al.*, 2012). In the present study, the wave age c/U_0 varies between 0.1 and 1.4, and two wave steepness values are considered, $ak = 0.10$ and 0.15 (table 2).

The wave steepness in the present study is within the range of values adopted in the previous studies of wind over fast waves, e.g. $ak = 0.10$ in Sullivan *et al.* (2000), $ak = 0.2$ in Hanley & Belcher (2008), $ak = 0.10$ and 0.25 in Yang & Shen (2010), $ak = 0.05 - 0.4$ in Jiang *et al.* (2016), and $ak = 0.10$ in Akervik & Vartdal (2019). The Reynolds number based on the wavelength of the surface wave and the top-driven velocity, $U_0\lambda/\nu$, is 30 000, which is higher than the previous DNS of wind over water waves, e.g., 8 800 in Sullivan *et al.* (2000), 10 000 in Yang & Shen (2010), and 15 000 in Druzhinin *et al.* (2012), but is still lower than the values in the real marine atmospheric boundary layer. Further increase of Reynolds number is prohibited by the high computation cost of the wall-resolved LES. However, as reviewed by Sullivan & McWilliams (2010), despite the lower Reynolds number, DNS and LES are capable to reveal many key physical processes in the turbulent wind–wave interactions. The Reynolds number based on the air friction velocity u_τ, i.e. $u_\tau\lambda/\nu$, is obtained *a posterior*, which varies slightly from case to case, but is larger than 600 for all of the cases as summarized in table 2. Here, u_τ is defined as $u_\tau = \sqrt{\tau_s/\rho_a}$, where τ_s is the mean viscous shear stress at the top of the simulation domain, and it equals the mean total stress in the streamwise direction at any given height in the wave boundary layer. To capture the wave-coherent motions in the wind field, a simulation domain of the size $(L_x, L_y, L_z) = (6\lambda, 4\lambda, \lambda)$ is adopted, following the previous studies (e.g., Sullivan *et al.*, 2000; Druzhinin *et al.*, 2012). The turbulent flow field is discretized in the computational space with $384^2 \times 193$ grid points, providing a resolution of $\Delta\xi^+ \simeq 21$, $\Delta\psi^+ \simeq 14$, and $\Delta\zeta^+_{\min} \simeq 0.2$, where $\Delta\zeta^+_{\min}$ denotes the minimum grid space in the ζ direction near the boundary. The superscript '+' indicates normalisation by the viscous length scale ν/u_τ. The grid resolution in all of the cases satisfies the requirement of wall-resolved LES specified by Choi & Moin (2012). The parameters and resolution of the LES cases in this study are summarized in table 2.

3.3 Features and order of magnitude of wave effects on airflow

In this section, we investigate the features and perform order-of-magnitude analyses of the wave-induced perturbations to the airflow using the LES data. We first examine in § 3.3.1 the wave effects on the airflow velocity and pressure. Then in § 3.3.2, the wave-induced perturbations to the airflow turbulence variance and turbulent stress are analysed.

To extract the wave effects on the wind field, we adopt the triple decomposition (Hussain & Reynolds, 1970) for an instantaneous physical quantity in the airflow,

$$f = \overline{f}(\xi,\zeta) + f'(\xi,\psi,\zeta,t) = \langle f\rangle(\zeta) + \widetilde{f}(\xi,\zeta) + f'(\xi,\psi,\zeta,t), \tag{61}$$

where f denotes an arbitrary physical quantity, $\overline{f}$ is its phase-averaged part, $\langle f\rangle$ is its mean value, which is obtained through the average in time and over the (ξ,ψ) plane, $\widetilde{f} = \overline{f} - \langle f\rangle$ is its wave-induced fluctuation, and $f' = f - \overline{f}$ is its turbulent fluctuation. We note that $\widetilde{f}$ in (61) is defined based on the computational curvilinear coordinates as in previous studies (e.g., Hsu *et al.*, 1981; Belcher & Hunt, 1993; Sullivan *et al.*, 2000; Druzhinin *et al.*, 2012; Buckley & Veron, 2016; Akervik & Vartdal, 2019). For periodic waves, $\widetilde{f}$ can be represented using its Fourier coefficient $\widehat{f}$, as

$$\widetilde{f} = \widehat{f}\mathrm{e}^{\mathrm{i}k\xi} + \widehat{f}^{*}\mathrm{e}^{-\mathrm{i}k\xi} = 2\,\mathrm{Re}\left[\widehat{f}\right]\cos(k\xi) - 2\,\mathrm{Im}\left[\widehat{f}\right]\sin(k\xi) = 2|\widehat{f}|\sin\Big(k\xi - \phi_{\widetilde{f}\widetilde{\eta}}\Big). \tag{62}$$

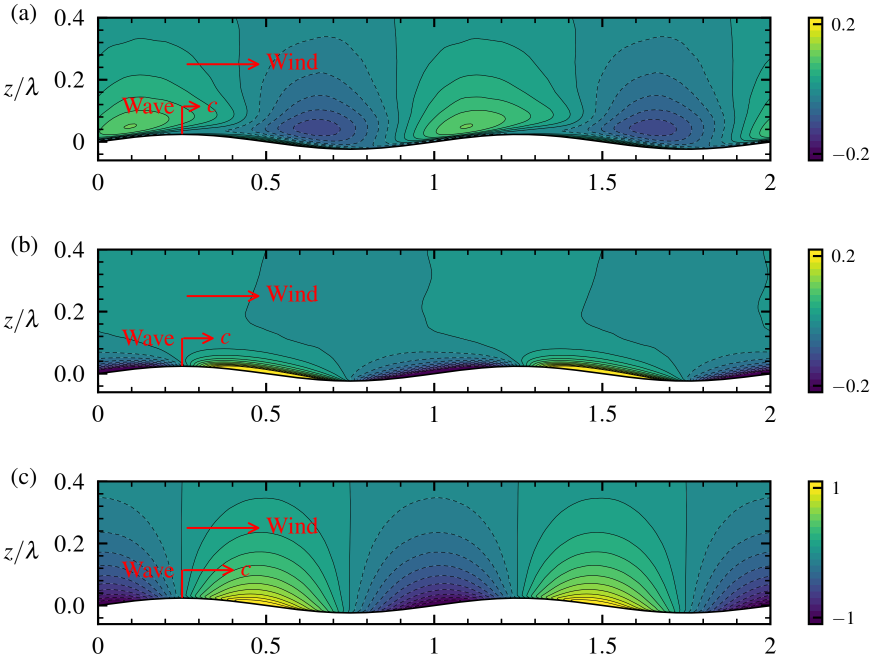

Figure 21: Wave-induced vertical air velocity $\widetilde{w}/(akU_0)$ for the wave conditions: (a) $c/U_0 = 0.1$; (b) $c/U_0 = 0.4$; (c) $c/U_0 = 1.2$. $ak = 0.15$.

Here '$|\cdot|$' is the modulus operator for complex numbers and $\phi_{\widetilde{f}\widetilde{\eta}} = \arctan\Big(\mathrm{Re}[\widehat{f}]/\,\mathrm{Im}[\widehat{f}]\Big)$ is the phase difference from the surface wave profile $\widetilde{\eta} = a\sin(k\xi)$, and $\widehat{f}^*$ is the complex conjugate of $\widehat{f}$.

3.3.1 Wave-induced velocity and pressure

In this subsection, we focus on the wave-induced velocity and pressure in the wind field. Figure 21 presents the wave-induced vertical velocity $\widetilde{w}$ for different wave ages. Here, we note that in §§ 3.3 and 3.5, to illustrate the behaviour of wave-induced airflow, we only present the results of $ak = 0.15$ as representative cases for space consideration, and to elucidate the mechanisms underlying the wave-induced airflow, the results are shown for both $ak = 0.1$ and $ak = 0.15$. It is shown that the structure of $\widetilde{w}$ varies substantially with c/U_0, indicating that the physical process producing $\widetilde{w}$ depends on c/U_0 significantly. For the slow wave with $c/U_0 = 0.1$ (figure 21*a*), away from the surface, $\widetilde{w}$ is mostly positive above the windward face and negative above the leeward face, without displaying antisymmetry across the wave crest. The $\widetilde{w}$ for slow waves ($c \simeq u_\tau$) is produced by the airflow blocked by the windward face of the wave due to the low wave speed. The airflow goes upward along the wave windward surface and thereby has a positive $\widetilde{w}$ there. However, when $c \gg u_\tau$, the wave surface no longer blocks the overlying airflow. As shown, for the intermediate wave with $c/U_0 = 0.4$ (figure 21*b*), the structure of $\widetilde{w}$ is remarkably different from that for the slow wave. Specifically, in the near surface region, $\widetilde{w}$ exhibits a nearly antisymmetric spatial structure about the wave crest, namely positive over the leeward side and negative over the windward side with a comparable magnitude. The antisymmetric distribution of $\widetilde{w}$ is also present in the fast wave case with $c/U_0 = 1.2$ (figure 21*c*), but with a much larger amplitude and extends to a much higher altitude in the airflow.

The nearly antisymmetric $\widetilde{w}$ in the intermediate (figure 21*b*) and fast (figure 21*c*) wave cases indicates that it is associated with the airflow perturbation induced by the vertical wave movement, i.e. w_s (55). At the surface, the vertical air velocity satisfies the Dirichlet boundary condition (55) and thereby $\widetilde{w}(\zeta = 0) = \widetilde{w}_s = -akc\cos(k\xi)$, with $\widetilde{\eta} = a\sin(k\xi)$. Therefore, one can expect that at the wave surface, a strong vertical motion of water wave would initiate a strong upward airflow at the leeward face and downward airflow at the windward face, which is confirmed by the LES result of $\widetilde{w}$ shown in figures 21(*b*) and 21(*c*). Away from the surface, the airflow perturbation induced by the vertical wave motion weakens gradually and thus the magnitude of $\widetilde{w}$

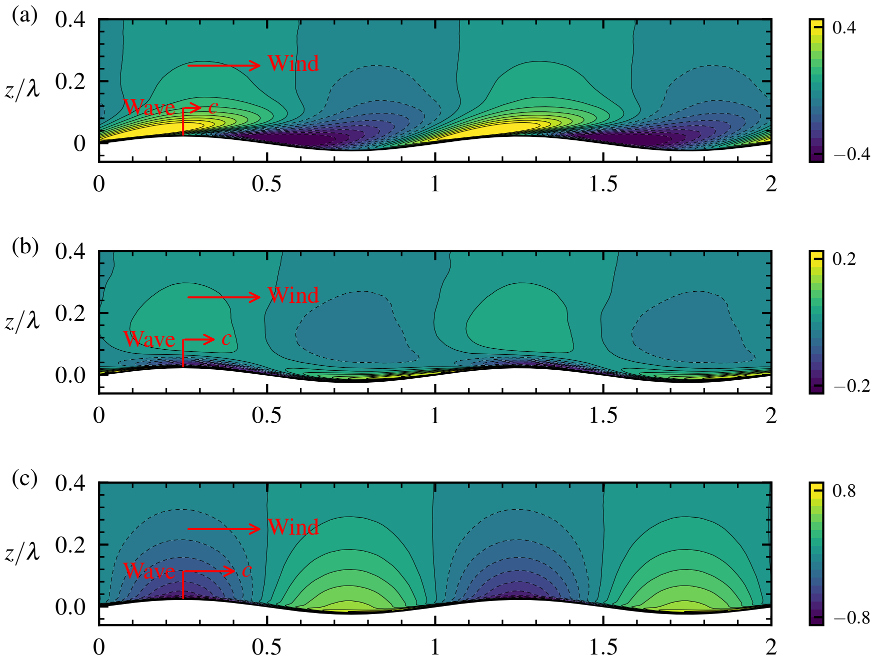

Figure 22: Wave-induced streamwise air velocity $\widetilde{u}/(akU_0)$ for the wave conditions: (a) $c/U_0 = 0.1$; (b) $c/U_0 = 0.4$; (c) $c/U_0 = 1.2$. $ak = 0.15$.

decays with height. The above mechanism for the arising of $\widetilde{w}$ indicates that $\widetilde{w}$ has an order of magnitude of akc for intermediate and fast waves. In particular, when the wave speed $c \gtrsim U_0$, we have $\widetilde{w} = O(akc) = O(akU_0)$. Therefore, in figure 21(c) with $c/U_0 = 1.2$, $\widetilde{w}/(akU_0)$ has a magnitude around 1, which is significantly larger than that in figures 21(a) and 21(b).

Figure 22 shows the wave-induced streamwise air velocity $\widetilde{u}$ for different c/U_0. At the low wave age with $c/U_0 = 0.1$ (figure 22a), $\widetilde{u}$ has a strong positive value at the windward side near the wave crest, caused by the airflow blocked there. Because the airflow accumulates at the windward face, a streamwise velocity acceleration is generated there to remove the gathered airflow and causes a positive $\widetilde{u}$. For the intermediate wave with $c/U_0 = 0.4$ (figure 22*b*), $\widetilde{u}$ has a large magnitude only in a very thin region above the surface. For the fast wave with $c/U_0 = 1.2$ (figure 22*c*), $\widetilde{u}$ is nearly in anti-phase with the wave elevation, namely a positive $\widetilde{u}$ above the wave trough and a negative $\widetilde{u}$ above the wave crest, which appears contrary to the airflow perturbation induced by the streamwise component of the wave kinematics. Specifically, at the wave surface, $\widetilde{u}(\zeta = 0) = \widetilde{u}_s = akc \sin(k\xi)$, with $\widetilde{\eta} = a \sin(k\xi)$, according to the Dirichlet boundary condition (53). Therefore, the streamwise motion of water wave induces a $\widetilde{u}$ in phase with the wave elevation (because $akc > 0$), which is not exhibited by the result in figure 22(*c*). In fact, for fast waves, $\widetilde{u}$ is mainly produced by the airflow perturbation induced by the vertical wave motion (figure 21*c*) through mass conservation as

$$\frac{\partial \widetilde{u}}{\partial \xi} = -\frac{\partial \widetilde{w}}{\partial \zeta} - \frac{\mathrm{d}\langle u \rangle}{\mathrm{d}\zeta} g\widetilde{\eta}_\xi, \tag{63}$$

which is derived using (69) in § 3.4 and illustrates how $\widetilde{u}$ can be generated by $\widetilde{w}$. Under the fast wave condition $c \gtrsim U_0$, at a vertical length scale $l = O(k^{-1})$, $\partial\widetilde{w}/\partial\zeta = O(ak^2c)$ and $\mathrm{d}\langle u \rangle/\mathrm{d}\zeta g\widetilde{\eta}_\xi = O(ak^2u_\tau)$, equation (63) suggests that away from the surface, $\widetilde{u}$ is dominated by $\partial\widetilde{w}/\partial\zeta$ and thereby $\widetilde{u} = O(akc) = O(akU_0)$, which is reflected in the result in figure 22(*c*). In addition, because $\widetilde{w}$ has the form of $-\cos(k\xi)$ and decays with ζ (figure 21*c*), the dominance of $\partial\widetilde{w}/\partial\zeta$ in (63) indicates that above the wave, $\widetilde{u}$ is in anti-phase with wave surface, which is consistent with figure 22(*c*).

Figure 23 presents the wave-induced air pressure $\widetilde{p}$ for different c/U_0. At the low wave age with $c/U_0 = 0.1$ (figure 23*a*), $\widetilde{p}$ is highly asymmetric about the wave crest, positive at the windward face and negative at the leeward face, which generates a strong form drag on the wave surface to transfer the momentum from the wind to wave. For the intermediate wave with $c/U_0 = 0.4$ (figure 23*b*), similar to $\widetilde{w}$ and $\widetilde{u}$,

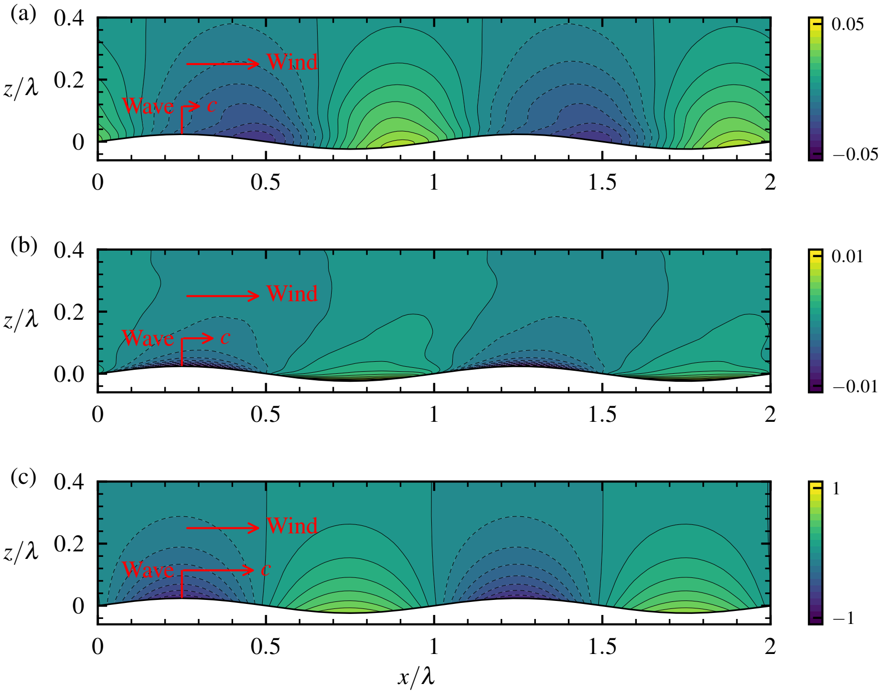

Figure 23: Wave-induced air pressure $\widetilde{p}/(ak\rho_a U_0^2)$ for the wave conditions: (a) $c/U_0 = 0.1$; (b) $c/U_0 = 0.4$; (c) $c/U_0 = 1.2$. $ak = 0.15$.

$\widetilde{p}$ is significant only within a thin region near the surface. For the fast wave with $c/U_0 = 1.2$ (figure 23*c*), similar to $\widetilde{u}$, $\widetilde{p}$ is strong and is nearly in anti-phase with the wave surface, owing to the vertical wave motion-induced airflow. To illustrate this point, we obtain the dominant mechanism for producing $\widetilde{p}$ using the vertical momentum equation of the wave-induced airflow, which is (detailed derivation is given in § 3.4.1)

$$(\langle u \rangle - c)\frac{\partial \widetilde{w}}{\partial \xi} \approx -\frac{\partial \widetilde{p}}{\partial \zeta}, \tag{64}$$

and the solution below follows,

$$\widetilde{p}|_\zeta \approx \int_\zeta^\infty (\langle u \rangle - c)\frac{\partial \widetilde{w}}{\partial \xi} \mathrm{d}\zeta. \tag{65}$$

Because for the fast wave, $\widetilde{w}$ is nearly in anti-phase with the wave slope $\widetilde{\eta}_\xi$ as shown in figure 21(*c*) and $\langle u \rangle - c < 0$, equation (65) illustrates that $\widetilde{p}$ is nearly in anti-phase with the wave elevation. Meanwhile, for $c \gtrsim U_0$, by considering $\widetilde{w} = O(akU_0)$ and $U_0/2 \lesssim |\langle u \rangle - c|$ when $\zeta/\lambda < 0.5$, we obtain that $\widetilde{p} = O(ak\rho_a U_0^2)$ based on (65), which is confirmed by the result of figure 23(*c*).

To summarize this subsection, the LES results have shown that the wave-induced airflow is governed by different physical processes between slow waves and fast waves. Specifically, for slow waves, the wave-induced airflow arises as a result of the blocking effect of the wave surface, while for fast waves it results from the airflow perturbation induced by the vertical motion of the wave. Therefore, when the wave speed c is comparable to or larger than the outer velocity U_0, i.e. $c \gtrsim U_0$, the wave-induced velocity and pressure scale as $\widetilde{u} = O(akc)$, $\widetilde{w} = O(akc)$, and $\widetilde{p} = O(ak\rho_a U_0^2)$, respectively, which are significantly stronger than those for the slow wave.

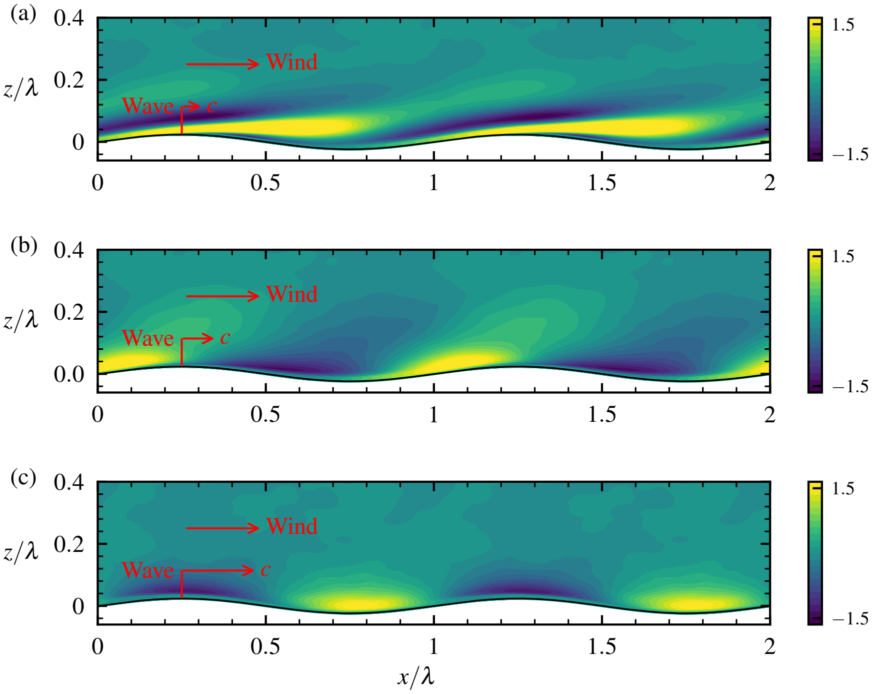

Figure 24: Wave-induced turbulence variance $(\widetilde{u'u'}+\widetilde{w'w'})/u_\tau^2$ for the wave conditions: (a) $c/U_0 = 0.1$; (b) $c/U_0 = 0.4$; (c) $c/U_0 = 1.2$. $ak = 0.15$.

3.3.2 Wave-induced turbulence variance and turbulent stress

In this subsection, we examine the spatial structure and magnitude of the wave-induced turbulence variance and turbulent shear stress. Figure 24 presents the distribution of wave-induced turbulence variance $\widetilde{u'u'}+\widetilde{w'w'} = \overline{u'u'} - \langle u'u' \rangle + \overline{w'w'} - \langle w'w' \rangle$ for different c/U_0. Here, $\widetilde{v'v'} = \overline{v'v'} - \langle v'v' \rangle$ is omitted because it does not affect the wave-induced airflow. In general, $\widetilde{u'u'} + \widetilde{w'w'}$ represents the wave effects on the turbulence kinematic energy in the air and it can in turn affect the behaviour of wave-induced airflow as illustrated in the previous studies on wind over slow waves (e.g., Belcher & Hunt, 1993; Miles, 1993, 1996). As shown, the slow wave with $c/U_0 = 0.1$ induces a strong positive $\widetilde{u'u'} + \widetilde{w'w'}$ above the leeward face of the wave

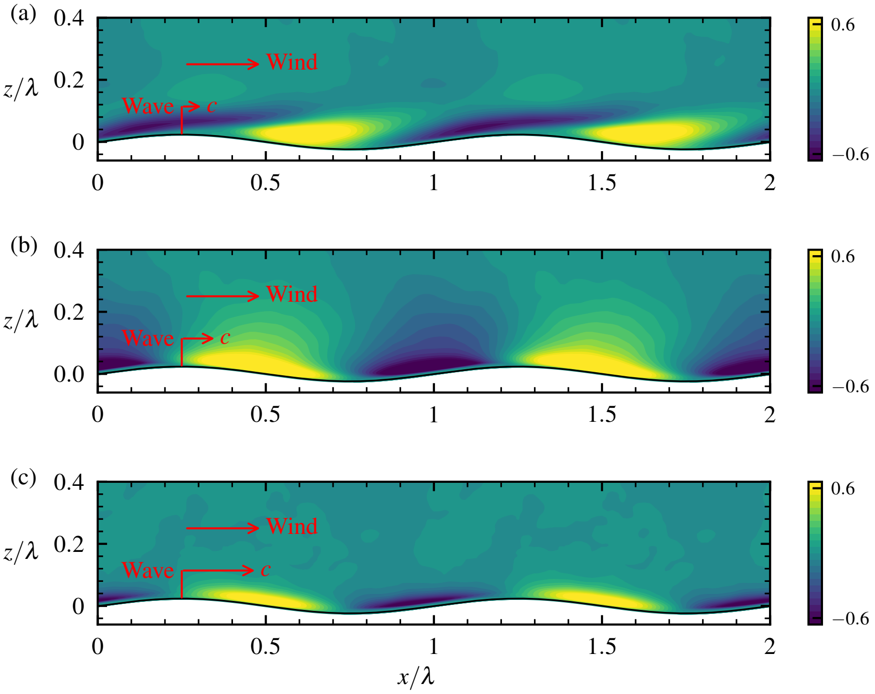

Figure 25: Wave-induced turbulent shear stress $-\widetilde{u'w'}/u_\tau^2$ for the wave conditions: (a) $c/U_0 = 0.1$; (b) $c/U_0 = 0.4$; (c) $c/U_0 = 1.2$. $ak = 0.15$.

(figure 24*a*). Buckley & Veron (2016) attributes this enhanced turbulence intensity to the sporadical airflow separation past the wave crest. By contrast, the intermediate wave with $c/U_0 = 0.4$ intensifies the turbulence variance at the windward face of the wave, and suppresses the turbulence variance at the leeward face (figure 24*b*). As the wave propagates faster with $c/U_0 = 1.2$, the regions corresponding to the intensified and suppressed turbulence variance shift further upstream, such that $\widetilde{u'u'} + \widetilde{w'w'}$ displays a positive value over the wave trough and negative value over the wave crest, as shown in figure 24(*c*). Importantly, it is observed that, unlike the $\widetilde{w}$, $\widetilde{u}$, and $\widetilde{p}$, the magnitudes of wave-induced turbulence variance normalised by u_τ^2 are comparable for different c/U_0 with a magnitude of $O(1)$, or $\widetilde{u'u'} + \widetilde{w'w'} = O(u_\tau^2)$.

Figure 25 compares the wave-induced turbulent shear stress $-\widetilde{u'w'} = -\overline{u'w'} - \langle -u'w' \rangle$ among the three wave ages. At the slow wave age with $c/U_0 = 0.1$, similar to the turbulence variance (figure 24*a*), the turbulent shear stress is enhanced above the leeward face of the wave (figure 25*a*), due to the effect of intermittent airflow separation downstream of the wave crest (Buckley & Veron, 2016). For the intermediate wave age with $c/U_0 = 0.4$, $-\widetilde{u'w'}$ has a negative value above the windward face and a positive value above the leeward face with an almost antisymmetric spatial structure across the wave crest (figure 25*b*). Compared with case $c/U_0 = 0.4$, at the high wave age with $c/U_0 = 1.2$, $-\widetilde{u'w'}$ exhibits a similar spatial distribution, but is limited to a slightly thinner region in the airflow (figure 25*c*). Similar to $\widetilde{u'u'} + \widetilde{w'w'}$, the LES results suggest that for different wave ages, $-\widetilde{u'w'} = O(u_\tau^2)$. The above results demonstrate that on the contrary to the wave-induced velocity and pressure, which are significantly stronger in the fast wave case than in the slow wave case, $\widetilde{u'u'} + \widetilde{w'w'}$ and $-\widetilde{u'w'}$ have magnitudes comparable for different wave speeds.

To conclude § 3.3, the LES results indicate that in the wind over fast waves, the wave-coherent airflow is dominated by the vertical wave motion-induced air motion, which is much stronger than that in wind over slow waves. On the contrary, compared with the slow wave, the modulation of turbulence variance and turbulent stress by the fast waves are not strengthened. These results together suggest that the effects of wave-induced turbulent stress on the wave-induced airflow become relatively weaker as the wave propagates faster. In § 3.4, we develop a linear analysis framework for the wave effects on the wind, based on which the fast wave-induced airflow is explained theoretically in § 3.5.

3.4 Development of linear analysis framework for wave effects

In this section, we develop a linear analysis framework for the wave-induced airflow in the turbulent wave boundary layer. In § 3.4.1, a linear model is presented based on non-orthogonal curvilinear coordinates. Using it, we analyse the effects of nonlinear forcing in § 3.4.2. To investigate the effects of coordinates system, we further develop a new linear model using orthogonal curvilinear coordinates in § 3.4.3, and show that the mechanisms of wave effects revealed by the linear models based on different coordinates are the same. In § 3.4.4, we show that a linear model can be split into two equations to investigate the effects of wave kinematics and body forcing induced by the wave elevation, respectively.

3.4.1 Non-orthogonal linear model

To capture the wave-induced quantities in the entire region of airflow including the height above the wave trough and below the wave crest, the Cartesian coordinates (x, y, z) can be transformed to the non-orthogonal curvilinear coordinates (ξ, ψ, ζ), as

$$\xi = x, \qquad \psi = y, \qquad \zeta = z + g(\zeta)\eta, \tag{66}$$

where $g(\zeta)$ can be any function that increases monotonically from the wave surface to the top of the simulation domain (Hsu *et al.*, 1981). In the present LES, the computational coordinates (56) follow the form of (66) with a linear mapping function $g = \zeta/L_z - 1$. With the general transformation (66) and the properties of phase average, the momentum and continuity equations for the wave-induced airflow can be expressed without the curvilinear coordinate variables as (see § 2)

$$
\begin{aligned}
(\langle u\rangle - c)\frac{\partial \widetilde{u}}{\partial \xi} + (\widetilde{w} + (\langle u\rangle - c) g\widetilde{\eta}_\xi)\frac{\mathrm{d}\langle u\rangle}{\mathrm{d}\zeta} + \frac{1}{\rho_a}\frac{\partial \widetilde{p}}{\partial \xi} &= \nu\Big(\frac{\partial^2 \widetilde{u}}{\partial \zeta^2} - \frac{\partial^2 \widetilde{w}}{\partial \xi \partial \zeta}\Big) \\
&\quad + \nu\frac{\mathrm{d}}{\mathrm{d}\zeta}\Big(\frac{\mathrm{d}\langle u\rangle}{\mathrm{d}\zeta} g_\zeta\Big)\widetilde{\eta} + O((ak)^2) + n.l.f., \qquad (67) \\
(\langle u\rangle - c)\frac{\partial \widetilde{w}}{\partial \xi} + \frac{1}{\rho_a}\frac{\partial \widetilde{p}}{\partial \zeta} &= \nu\Big(\frac{\partial^2 \widetilde{w}}{\partial \xi^2} + \frac{\partial^2 \widetilde{w}}{\partial \zeta^2}\Big) + O((ak)^2) + n.l.f., \qquad (68) \\
\frac{\partial \widetilde{u}}{\partial \xi} + \frac{\partial \widetilde{w}}{\partial \zeta} + \frac{\mathrm{d}\langle u\rangle}{\mathrm{d}\zeta} g\widetilde{\eta}_\xi &= 0 + O((ak)^2), \qquad (69)
\end{aligned}
$$

where $O((ak)^2)$ denotes the neglected second- and higher-order terms, and '$n.l.f.$' represents the neglected nonlinear forcing, i.e. the wave-induced fluctuations of the turbulent stress, i.e. $\widetilde{\tau}_{jm}$, and the wave-induced stress, i.e. $\widetilde{\tau}^w_{jm}$, where $\tau_{jm} = -u'_j U'_m + J^{-1}\tau^d_{jl}\partial\xi_m/\partial x_l$ and $\tau^w_{jm} = -\widetilde{u}_j \widetilde{U}_m$ with $U_j = J^{-1}u_m \partial\xi_j/\partial x_m$. The effects of $\widetilde{\tau}^w_{jm}$ are always small for moderate wave slopes, and the effects of $\widetilde{\tau}_{jm}$ are analysed in § 3.4.2. By eliminating $\widetilde{u}$ and $\widetilde{p}$, we can reduce the equation system (67)–(69) to a single equation for $\widetilde{w}$ as (see § 2)

$$
\begin{aligned}
-\frac{\nu}{\mathrm{i}k}\left[\frac{\mathrm{d}^4}{\mathrm{d}\zeta^4} - 2k^2\frac{\mathrm{d}^2}{\mathrm{d}\zeta^2} + k^4\right]\widehat{w} + \left[(\langle u\rangle - c)\Big(\frac{\mathrm{d}^2}{\mathrm{d}\zeta^2} - k^2\Big) - \frac{\mathrm{d}^2\langle u\rangle}{\mathrm{d}\zeta^2}\right]\widehat{w} \\
= \nu\widehat{\eta}\frac{\mathrm{d}^2}{\mathrm{d}\zeta^2}\left[g\frac{\mathrm{d}^2\langle u\rangle}{\mathrm{d}\zeta^2}\right] + O((ak)^2) + n.l.f, \qquad (70)
\end{aligned}
$$

where $\widehat{w}$ is the Fourier coefficient of $\widetilde{w}$ (62). The linear equation (70) is different from the original Orr–Sommerfeld equation (e.g., Lin, 1955) in that the presence of the wave elevation $\widehat{\eta}$ leads to a forcing term on its right hand side.

Equation (70) can be solved using the boundary conditions imposed by the wave kinematics, which are the Dirichlet boundary conditions for $\widehat{w}$,

$$\widehat{w}|_{\zeta=0} = \widehat{w}_s, \qquad \widehat{w}|_{\zeta=\infty} = 0, \tag{71}$$

and the Neumann boundary conditions for $\mathrm{d}\widehat{w}/\mathrm{d}\zeta$, which can be derived from (69) and read

$$\left.\frac{\mathrm{d}\widehat{w}}{\mathrm{d}\zeta}\right|_{\zeta=0} = \mathrm{i}k\widehat{u}_s - \mathrm{i}k\widehat{\eta}\left.\frac{\mathrm{d}\langle u\rangle}{\mathrm{d}\zeta}\right|_{\zeta=0}, \qquad \left.\frac{\mathrm{d}\widehat{w}}{\mathrm{d}\zeta}\right|_{\zeta=\infty} = 0, \tag{72}$$

where $\widehat{u}_s$ and $\widehat{w}_s$ are the Fourier coefficients of the streamwise (53) and vertical (55) components of wave orbital velocity, respectively. In § 3.5, equation (70) with $g = \zeta/L_z - 1$ is numerically solved using the mean wind velocity $\langle u\rangle$ from the LES, and its results are compared with LES data to illustrate the mechanisms for the fast wave-induced airflow.

3.4.2 Effects of fast wave-induced turbulent stress

In this subsection we perform scaling analysis of the effects of fast wave-induced turbulent stress $\widetilde{\tau}_{jm}$ on the wave-induced momentum equations (67) and (68). In § 3.3, the LES results have shown that for fast waves $\widetilde{w} = O(akc)$, $\widetilde{u'u'} + \widetilde{w'w'} = O(u_\tau^2)$, and $-\widetilde{u'w'} = O(u_\tau^2)$. Based on these results, it can be further shown that in the curvilinear coordinates, the wave-induced turbulent stress satisfies $\widetilde{\tau}_{jm} = O(u_\tau^2)$, which has been neglected in deriving (67) and (68). By comparing the magnitude of $\widetilde{\tau}_{jm}$ with the stress terms in (67) and (68), we can evaluate the effects of $\widetilde{\tau}_{jm}$ on the fast wave-induced airflow.

To investigate the effects of $\widetilde{\tau}_{jm}$, we focus on a vertical length scale l satisfying $kl < 1$, because $\widetilde{u'u'} + \widetilde{w'w'}$ (figure 24) and $-\widetilde{u'w'}$ (figure 25) are significant only within this region. To analyse the streamwise momentum equation (67), we can reduce it into the following form by using (69) to eliminate $\widetilde{u}$ as

$$-(\langle u\rangle - c)\frac{\partial \widetilde{w}}{\partial \zeta} + \widetilde{w}\frac{\mathrm{d}\langle u\rangle}{\mathrm{d}\zeta} + \frac{1}{\rho_a}\frac{\partial \widetilde{p}}{\partial \xi} = \nu\Big(\frac{\partial^2 \widetilde{u}}{\partial \zeta^2} - \frac{\partial^2 \widetilde{w}}{\partial \xi \partial \zeta}\Big) + \nu\frac{\mathrm{d}}{\mathrm{d}\zeta}\Big(\frac{\mathrm{d}\langle u\rangle}{\mathrm{d}\zeta}g_\zeta\Big)\widetilde{\eta}. \tag{73}$$

With the results in § 3.3, we can obtain the the following scaling in (73),

$$\frac{1/\rho_a \partial \widetilde{p}/\partial \xi}{-(\langle u\rangle - c)\partial \widetilde{w}/\partial \zeta} \sim \frac{akU_0^2 \cdot k}{akU_0^2/l} = kl, \tag{74}$$

$$\frac{\widetilde{w}\langle u\rangle_\zeta}{-(\langle u\rangle - c)\partial \widetilde{w}/\partial \zeta} \sim \frac{akU_0\langle u\rangle(l)/l}{akU_0^2/l} = \frac{\langle u\rangle(l)}{U_0}, \tag{75}$$

$$\frac{\partial \widetilde{\tau}_{11}/\partial \xi}{-(\langle u\rangle - c)\partial \widetilde{w}/\partial \zeta} \sim \frac{u_\tau^2 \cdot k}{akU_0^2/l} < \frac{u_\tau^2/l}{akU_0^2/l} \sim \frac{\partial \widetilde{\tau}_{13}/\partial \zeta}{-(\langle u\rangle - c)\partial \widetilde{w}/\partial \zeta} \sim \frac{1}{ak}\Big(\frac{u_\tau}{U_0}\Big)^2, \tag{76}$$

where $\langle u\rangle(l)$ is the value of $\langle u\rangle$ at $\zeta = l$. Similarly, for the vertical momentum equation (68), we have

$$\frac{(\langle u\rangle - c)\partial \widetilde{w}/\partial \xi}{1/\rho_a \partial \widetilde{p}/\partial \zeta} \sim \frac{akU_0^2 \cdot k}{akU_0^2/l} = kl, \tag{77}$$

$$\frac{\partial \widetilde{\tau}_{31}/\partial \xi}{1/\rho_a \partial \widetilde{p}/\partial \zeta} \sim \frac{u_\tau^2 \cdot k}{akU_0^2/l} < \frac{u_\tau^2/l}{akU_0^2/l} \sim \frac{\partial \widetilde{\tau}_{33}/\partial \zeta}{1/\rho_a \partial \widetilde{p}/\partial \zeta} \sim \frac{1}{ak}\Big(\frac{u_\tau}{U_0}\Big)^2. \tag{78}$$

Because in the wave surface layer, $ak \simeq 0.1$ and $U_0/u_\tau \simeq 30$ such that $1/(ak)(u_\tau/U_0)^2 \ll 1$, we see that $\partial\widetilde{\tau}_{11}/\partial\xi$ and $\partial\widetilde{\tau}_{13}/\partial\zeta$ are significantly smaller than $-(\langle u\rangle - c)\partial\widetilde{w}/\partial\zeta$ in the streamwise momentum equation (73). Likewise, $\partial\widetilde{\tau}_{31}/\partial\xi$ and $\widetilde{\tau}_{33}/\partial\zeta$ have negligible effects compared with $1/\rho_a \cdot \partial\widetilde{p}/\partial\zeta$ in the vertical momentum equation (68). For $ak \ll 0.1$, the magnitude of $\widetilde{\tau}_{jm}$ should be much smaller than $O(u_\tau^2)$, and we still expect that its effects are much smaller than the wave-induced advection or pressure. The results above suggest that with $c \gtrsim U_0$ for fast waves, the effects of wave-induced turbulent stress $\widetilde{\tau}_{jm}$ on the wave-induced airflow are always much smaller than the dominant forcing in the wave-induced momentum equations, which constitutes the physical grounds of neglecting $\widetilde{\tau}_{jm}$, i.e. the nonlinear forcing, in the linear equations.

3.4.3 Orthogonal linear model

In this subsection, we develop linearised equations based on the orthogonal curvilinear coordinates to investigate the effects of transformation orthogonality on the modelling of the wave-induced airflow. The following orthogonal mapping between the physical coordinates and curvilinear coordinates is considered, which has been extensively used in the literature (e.g., Sullivan *et al.*, 2000; Buckley & Veron, 2016; Yousefi & Veron, 2020; Yousefi *et al.*, 2020),

$$\xi = x - \mathrm{i}a\mathrm{e}^{-kz}\mathrm{e}^{\mathrm{i}kx}, \qquad \psi = y, \qquad \zeta = z - a\mathrm{e}^{-kz}\mathrm{e}^{\mathrm{i}kx}. \tag{79}$$

Based on the above mapping, the momentum and mass equations for the wave-induced airflow are obtained as (see the derivations in appendix F)

$$\begin{aligned} (\langle u\rangle - c)\frac{\partial \widetilde{u}}{\partial \xi} + (\widetilde{w} - (\langle u\rangle - c)\mathrm{e}^{-\mathrm{k}\zeta}\widetilde{\eta}_\xi)\frac{\mathrm{d}\langle u\rangle}{\mathrm{d}\zeta} + \frac{1}{\rho_a}\frac{\partial \widetilde{p}}{\partial \xi} = \\ \nu\Big(\frac{\partial^2 \widetilde{u}}{\partial \xi^2} + \frac{\partial^2 \widetilde{u}}{\partial \zeta^2}\Big) + O((ak)^2) + n.l.f., \end{aligned} \tag{80}$$

$$(\langle u\rangle - c)\frac{\partial \widetilde{w}}{\partial \xi} + \frac{1}{\rho_a}\frac{\partial \widetilde{p}}{\partial \zeta} = \nu\Big(\frac{\partial^2 \widetilde{w}}{\partial \xi^2} + \frac{\partial^2 \widetilde{w}}{\partial \zeta^2}\Big) + O((ak)^2) + n.l.f., \tag{81}$$

$$\frac{\partial \widetilde{u}}{\partial \xi} + \frac{\partial \widetilde{w}}{\partial \zeta} - \frac{\mathrm{d}\langle u\rangle}{\mathrm{d}\zeta}\mathrm{e}^{-\mathrm{k}\zeta}\widetilde{\eta}_\xi = 0 + O((ak)^2). \tag{82}$$

Using (80)–(82) and eliminating $\widetilde{u}$ and $\widetilde{p}$, we can obtain the equation for $\widehat{w}$ as

$$-\frac{\nu}{\mathrm{i}k}\left[\frac{\mathrm{d}^4}{\mathrm{d}\zeta^4}-2k^2\frac{\mathrm{d}^2}{\mathrm{d}\zeta^2}+k^4\right]\widehat{w}+\left[(\langle u\rangle-c)\Big(\frac{\mathrm{d}^2}{\mathrm{d}\zeta^2}-k^2\Big)-\frac{\mathrm{d}^2\langle u\rangle}{\mathrm{d}\zeta^2}\right]\widehat{w}$$
$$=-\nu\widehat{\eta}\left[\frac{\mathrm{d}^2}{\mathrm{d}\zeta^2}-k^2\right]\left(\frac{\mathrm{d}}{\mathrm{d}\zeta}\Big(\frac{\mathrm{d}\langle u\rangle}{\mathrm{d}\zeta}\mathrm{e}^{-\mathrm{k}\zeta}\Big)\right)+O((ak)^2)+n.l.f. \tag{83}$$

Based on (53), (55) and (82), it can be shown that (83) can be solved with the same boundary conditions as (70), namely the boundary conditions (71) and (72).

A comparison between (70) and (83) provides valuable insights into the effects of curvilinear coordinates system on the wave-induced airflow modelling. First, equation (83) has the same left-hand-side terms as (70) and both of them have a non-zero right-hand-side term. More importantly, the dominant terms on the right hand side of (83) and (70) are consistent with each other. Specifically, the right hand side of (83) is dominated by the term related to the fourth-order vertical derivative of $\langle u\rangle$, namely $-\nu\widehat{\eta}\mathrm{e}^{-k\zeta}\mathrm{d}^4\langle u\rangle/\mathrm{d}^4\zeta$, which is the same as the dominant term of the right hand side of (70) with $g=-\exp(-k\zeta)$. This result suggests that the solution of (83) using the orthogonal mapping should be consistent with the solution of (70) using the non-orthogonal transformation with a mapping function $g=-\exp(-k\zeta)$. Second, both (83) and (70) are driven by the same boundary conditions, indicating that the wave kinematics impose the same effects on the wave-induced airflow between these two coordinates systems. A more detailed analysis on the effects of coordinates systems is presented in § 3.5.4.

3.4.4 Split equations of linear model

In this subsection, we develop split equations for the linear models of the wave effects. The expressions of the linear models (70) and (83), and their boundary conditions (71)–(72), reveal two mechanisms of the impacts of fast waves on the overlying turbulent wind field, namely the forcing induced by the wave elevation, which is the source term on the right hand side of (70) and (83), and the wave kinematics, which is shown by the boundary conditions (71)–(72). To investigate these two mechanisms separately, we can split a linear equation into two separate equations corresponding to the two components of $\widehat{w}$, $\widehat{w}^k$ and $\widehat{w}^f$, respectively,

$$\widehat{w} = \widehat{w}^k + \widehat{w}^f. \tag{84}$$

In the equation above, $\widehat{w}^k$ and $\widehat{w}^f$ are the vertical velocity perturbations associated with the wave kinematics and by the forcing caused by the wave elevation, respectively.

We use (70) to illustrate the splitting procedure. Extracted from (70), the equation for $\widehat{w}^k$ has a zero source term on the right hand side, but is driven by the wave orbital velocity at the wave surface, which is

$$-\frac{\nu}{\mathrm{i}k}\left[\frac{\mathrm{d}^4}{\mathrm{d}\zeta^4} - 2k^2\frac{\mathrm{d}^2}{\mathrm{d}\zeta^2} + k^4\right]\widehat{w}^k + \left[(\langle u\rangle - c)\Big(\frac{\mathrm{d}^2}{\mathrm{d}\zeta^2} - k^2\Big) - \frac{\mathrm{d}^2\langle u\rangle}{\mathrm{d}\zeta^2}\right]\widehat{w}^k = 0, \tag{85}$$

with the boundary conditions

$$\widehat{w}^k\Big|_{\zeta=0} = \widehat{w}_s, \qquad \widehat{w}^k\Big|_{\zeta=\infty} = 0, \tag{86}$$

$$\frac{\mathrm{d}\widehat{w}^k}{\mathrm{d}\zeta}\bigg|_{\zeta=0} = -\mathrm{i}k\widehat{u}_s - \mathrm{i}k\widehat{\eta}\left(g\frac{\mathrm{d}\langle u\rangle}{\mathrm{d}\zeta}\right)\bigg|_{\zeta=0}, \qquad \frac{\mathrm{d}\widehat{w}^k}{\mathrm{d}\zeta}\bigg|_{\zeta=\infty} = 0. \tag{87}$$

On the contrary, the equation for $\widehat{w}^f$ has a non-zero source term on the right hand side, but is not affected by the wave kinematics at the surface,

$$\begin{aligned} -\frac{\nu}{\mathrm{i}k}\left[\frac{\mathrm{d}^4}{\mathrm{d}\zeta^4} - 2k^2\frac{\mathrm{d}^2}{\mathrm{d}\zeta^2} + k^4\right]\widehat{w}^f + \left[(\langle u\rangle - c)\Big(\frac{\mathrm{d}^2}{\mathrm{d}\zeta^2} - k^2\Big) - \frac{\mathrm{d}^2\langle u\rangle}{\mathrm{d}\zeta^2}\right]\widehat{w}^f \\ = \nu\widehat{\eta}\frac{\mathrm{d}^2}{\mathrm{d}\zeta^2}\left[g\frac{\mathrm{d}^2\langle u\rangle}{\mathrm{d}\zeta^2}\right], \end{aligned} \tag{88}$$

with the homogeneous boundary conditions

$$\widehat{w}^f\Big|_{\zeta=0} = 0, \qquad \widehat{w}^f\Big|_{\zeta=\infty} = 0, \tag{89}$$

$$\frac{\mathrm{d}\widehat{w}^f}{\mathrm{d}\zeta}\bigg|_{\zeta=0} = 0, \qquad \frac{\mathrm{d}\widehat{w}^f}{\mathrm{d}\zeta}\bigg|_{\zeta=\infty} = 0. \tag{90}$$

In §§ 3.5.1 and 3.5.2, the equations (85)–(87) and (88)–(90) are solved separately, and their solutions are compared with the LES data to elucidate the effects of wave kinematics and forcing by the wave elevation on fast wave-induced airflow.

To conclude § 3.4, we have developed a linear analysis framework for the fast wave effects on the overlying turbulent wind field. The scaling analysis shows that for $c \gtrsim U_0$, the nonlinear forcing has secondary effects on the wave-induced airflow compared with the advection induced by $\widetilde{w}$ and the gradient of $\widetilde{p}$. The linear models based on different curvilinear coordinates systems show the same mechanisms for wave effects on the airflow, namely the wave kinematics and the forcing induced by the wave elevation, which can be investigated separately by the split linear models.

3.5 Explanation of fast wave-induced airflow using linear theory

In this section, we analyse the behaviours and the underlying mechanisms of fast wave-induced airflow through the comparisons between the solutions of the linear equations in § 3.4 and the LES results. The dominant and weak components of the wave-induce airflow are investigated in §§ 3.5.1 and 3.5.2, respectively. In § 3.5.3, we examine the generation of wave-coherent stress in the wind and the form drag on the wave surface. At last, in § 3.5.4 we compare the behaviours of the fast wave-induced airflow between the solutions of the linear equations using different curvilinear coordinate systems.

To explain the fast wave-induced airflow, we express the wave-induced vertical velocity $\widetilde{w}$, wave-induced streamwise velocity $\widetilde{u}$, and wave-induced pressure $\widetilde{p}$ using their Fourier coefficients (62), as

$$\widetilde{w} = 2|\widehat{w}| \sin\big(k\xi - \phi_{\widetilde{w}\widetilde{\eta}}\big), \tag{91}$$

$$\widetilde{u} = 2|\widehat{u}| \sin\big(k\xi - \phi_{\widetilde{u}\widetilde{\eta}}\big), \tag{92}$$

$$\widetilde{p} = 2|\widehat{p}| \sin\big(k\xi - \phi_{\widetilde{p}\widetilde{\eta}}\big), \tag{93}$$

where $2|\widehat{w}|$, $2|\widehat{u}|$, $2|\widehat{p}|$ are the amplitude of $\widetilde{w}$, $\widetilde{u}$, and $\widetilde{p}$, respectively, and $\phi_{\widetilde{w}\widetilde{\eta}}$, $\phi_{\widetilde{u}\widetilde{\eta}}$, and $\phi_{\widetilde{p}\widetilde{\eta}}$ are the phase difference of $\widetilde{w}$, $\widetilde{u}$, and $\widetilde{p}$ with respect to the wave surface $\widetilde{\eta} = \sin(k\xi)$, respectively.

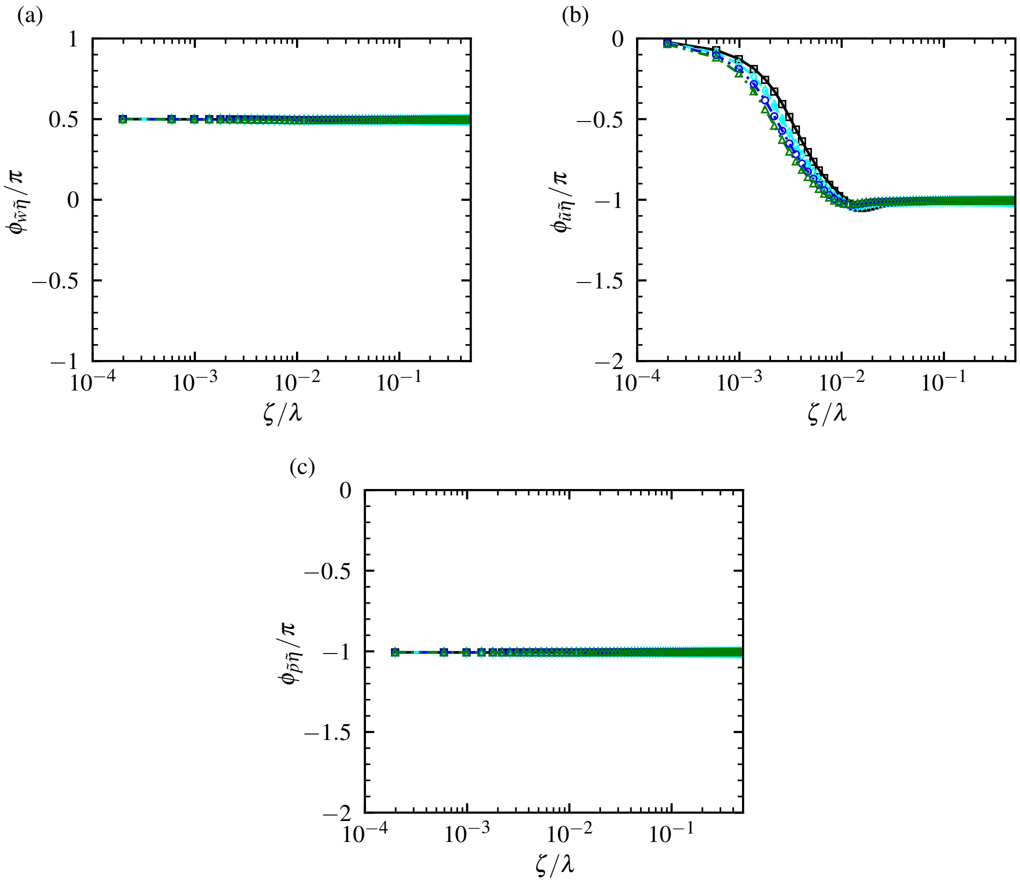

Figure 26: Comparison of the phase difference (a) $\phi_{\widetilde{w}\widetilde{\eta}}$ (91), (b) $\phi_{\widetilde{u}\widetilde{\eta}}$ (92), and (c) $\phi_{\widetilde{p}\widetilde{\eta}}$ (93) between the LES results and the solutions of linear equation (70) for the fast waves. Lines are the LES results: —, $c/U_0 = 0.8$; - - -, $c/U_0 = 1.0$; -·-, $c/U_0 = 1.2$; -··-, $c/U_0 = 1.4$. Symbols are the linear solutions: □, $c/U_0 = 0.8$; ◇, $c/U_0 = 1.0$; ○, $c/U_0 = 1.2$; △, $c/U_0 = 1.4$. In all of the four cases, $ak = 0.15$. Note that in (a) and (c), the results for different cases collapse.

Figure 26 compares the phase difference $\phi_{\widetilde{w}\widetilde{\eta}}$ (91), $\phi_{\widetilde{u}\widetilde{\eta}}$ (92), and $\phi_{\widetilde{p}\widetilde{\eta}}$ (93) between the LES results and the solutions of the linear equation (70) for the fast waves. In all of the four wave cases shown, the linear solutions agree well with the LES results. It is found that $\phi_{\widetilde{w}\widetilde{\eta}} \approx \pi/2$ (figure 26*a*) and $\phi_{\widetilde{p}\widetilde{\eta}} \approx -\pi$ (figure 26*c*) throughout the wave boundary layer, consistent with the observation in figures 21(*c*) and 23(*c*), respectively. From the definitions of $\phi_{\widetilde{w}\widetilde{\eta}}$ and $\phi_{\widetilde{p}\widetilde{\eta}}$ (62), it can be deduced that $|\,\mathrm{Re}[\widehat{w}]| \gg |\,\mathrm{Im}[\widehat{w}]|$ and $|\,\mathrm{Im}[\widehat{p}]| \gg |\,\mathrm{Re}[\widehat{p}]|$ throughout the wave boundary layer. Figure 26(*b*) shows that $\phi_{\widetilde{u}\widetilde{\eta}} \approx -\pi$ only away from the surface, $\zeta/\lambda \geq 0.01$, which is consistent with the results in figure 22(*c*) and suggests that $|\,\mathrm{Im}[\widehat{u}]| \gg |\,\mathrm{Re}[\widehat{u}]|$ there. At the surface, owing to the non-slip boundary condition $\widetilde{u} = ak\sin(k\xi)$ (53), it is obtained that $\phi_{\widetilde{u}\widetilde{\eta}} = 0$. These results indicate that the direct effect of the boundary condition (53) on $\widetilde{u}$ is only limited to a very thin region in the airflow, $\zeta/\lambda \leq 0.01$. In the following subsections, the mechanisms for the strong ($\mathrm{Re}[\widehat{w}]$, $\mathrm{Im}[\widehat{u}]$, and $\mathrm{Im}[\widehat{p}]$) and weak ($\mathrm{Im}[\widehat{w}]$, $\mathrm{Re}[\widehat{u}]$, and $\mathrm{Re}[\widehat{p}]$) components of fast wave-induced airflow are investigated.

3.5.1 Mechanisms for dominant components of wave-induced airflow

Insofar, we have demonstrated that for fast waves, $\mathrm{Re}[\widehat{w}]$, $\mathrm{Im}[\widehat{u}]$, and $\mathrm{Im}[\widehat{p}]$ are the dominant components of $|\widehat{w}|$, $|\widehat{u}|$, and $|\widehat{p}|$, respectively. In this subsection, we explain how they are produced. First, we identify the flow dynamics governing the dominant wave-induced airflow. Figure 27 compares the magnitudes and the dominant components of the wave-induced velocity and pressure between the LES results and the solutions of linear equation (70) for four fast waves. The agreement between the LES results and the linear solutions demonstrates that the dominant components of

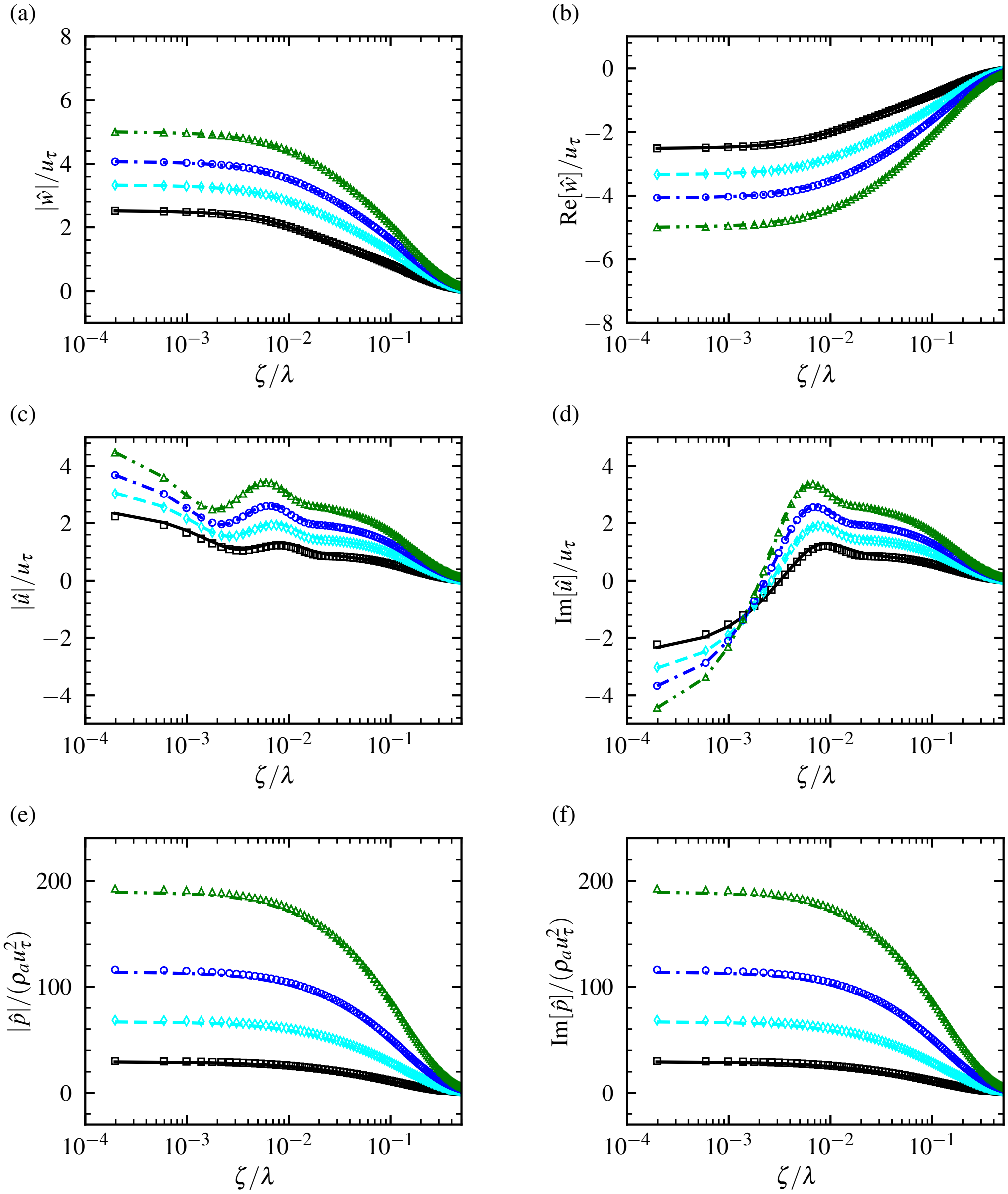

Figure 27: Comparison of the magnitudes (left column) and the dominant components (right column) of wave-induced airflow between the LES results and the solutions of linear equation (70) for the fast waves: (*a*) $|\widehat{w}|$; (*b*) $\mathrm{Re}[\widehat{w}]$; (*c*) $|\widehat{u}|$; (*d*) $\mathrm{Im}[\widehat{u}]$; (*e*) $|\widehat{p}|$; and (*f*) $\mathrm{Im}[\widehat{p}]$. Lines are the LES results: ——, $c/U_0 = 0.8$; - - -, $c/U_0 = 1.0$; -·-, $c/U_0 = 1.2$; -···, $c/U_0 = 1.4$. Symbols are the linear solutions: □, $c/U_0 = 0.8$; ◇, $c/U_0 = 1.0$; ○, $c/U_0 = 1.2$; △, $c/U_0 = 1.4$. $ak = 0.15$.

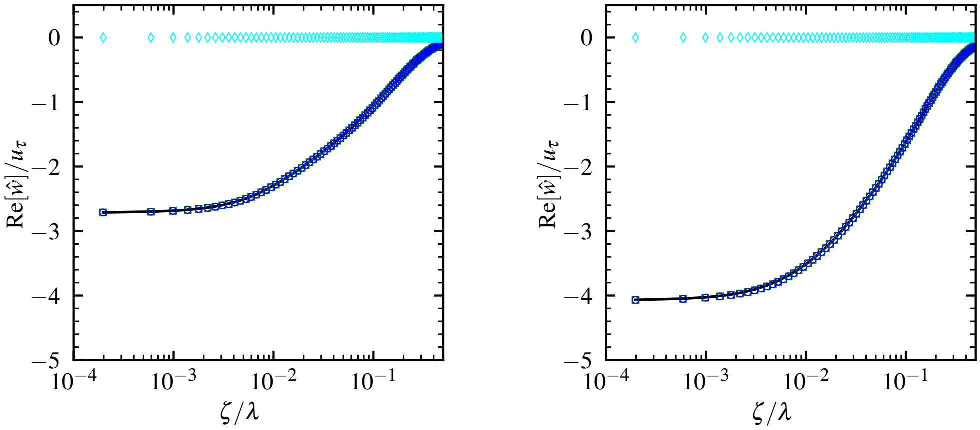

Figure 28: Comparison among $\mathrm{Re}[\widehat{w}^k]$ solved from (85), $\mathrm{Re}[\widehat{w}^f]$ solved from (88), $\mathrm{Re}[\widehat{w}^k] + \mathrm{Re}[\widehat{w}^f]$, and the $\mathrm{Re}[\widehat{w}]$ result from LES for (*a*) case $(c/U_0, ak) = (1.2, 0.10)$ and (*b*) case $(c/U_0, ak) = (1.2, 0.15)$. ∘, $\mathrm{Re}[\widehat{w}^k]$; ◇, $\mathrm{Re}[\widehat{w}^f]$; ▫, $\mathrm{Re}[\widehat{w}^k]$+$\mathrm{Re}[\widehat{w}^f]$; and —, LES result of $\mathrm{Re}[\widehat{w}]$. Note that $\mathrm{Re}[\widehat{w}^k]$ and $\mathrm{Re}[\widehat{w}^k] + \mathrm{Re}[\widehat{w}^f]$ collapse together.

wave-induced airflow are controlled by linear dynamics. As shown, $|\widehat{w}|$ and $|\widehat{p}|$ have almost the same magnitudes as $\mathrm{Re}[\widehat{w}]$ and $\mathrm{Im}[\widehat{p}]$, respectively, throughout the boundary layer, indicating that the overall structures of $\widetilde{w}$ and $\widetilde{p}$ are determined by $\mathrm{Re}[\widehat{w}]$ and $\mathrm{Im}[\widehat{p}]$, respectively. Because $\mathrm{Re}[\widehat{w}]$ maintains a negative value and $\mathrm{Im}[\widehat{p}]$ has a positive sign, using (62) we can obtain that $\phi_{\widetilde{w}\widetilde{\eta}} \approx \pi/2$ and $\phi_{\widetilde{p}\widetilde{\eta}} \approx -\pi$, which explain the results of figures 26(*a*) and 26(*c*). By contrast, $|\widehat{u}|$ has a similar magnitude as $\mathrm{Im}[\widehat{u}]$ only at $\zeta/\lambda \geq 0.01$, indicating that $\mathrm{Im}[\widehat{u}]$ determines the structure of $\widetilde{u}$ there. The positive value of $\mathrm{Im}[\widehat{u}]$ for $\zeta/\lambda \geq 0.01$ suggests that $\phi_{\widetilde{u}\widetilde{\eta}} \approx -\pi$. For $\zeta/\lambda < 0.01$, $\phi_{\widetilde{u}\widetilde{\eta}}$ transits from zero at the surface to $-\pi$ further away, which is caused by the change of the sign of $\mathrm{Im}[\widehat{u}]$ across this thin region. These results explain figure 26(*b*).

The quasilinear behaviour of the dominant wave-induced airflow suggests that the underlying mechanisms can be explained using the linear models. The key is to identify the physical processes that generate $\mathrm{Re}[\widehat{w}]$, which can be found using the split linear equations obtained in § 3.4.4. As mentioned above, (85) for $\widehat{w}^k$ and (88) for $\widehat{w}^f$ represent the effects of the wave kinematics and the forcing by wave elevation, respectively. Figure 28 compares $\mathrm{Re}[\widehat{w}^k]$ solved from (85), $\mathrm{Re}[\widehat{w}^f]$ solved from (88), and $\mathrm{Re}[\widehat{w}^k] + \mathrm{Re}[\widehat{w}^f]$ with the $\mathrm{Re}[\widehat{w}]$ result from the LES for $ak = 0.1$ and 0.15. As shown, for both wave steepness, $\mathrm{Re}[\widehat{w}]$ is contributed to almost entirely by $\mathrm{Re}[\widehat{w}^k]$ with near zero contribution from $\mathrm{Re}[\widehat{w}^f]$, indicating that the wave kinematics plays a primary role in perturbing the vertical airflow velocity. To further investigate how the wave kinematics produces $\mathrm{Re}[\widehat{w}^k]$, we examine the boundary conditions for $\mathrm{Re}[\widehat{w}^k]$, which can be derived from (86) and (87), and read

$$\mathrm{Re}[\widehat{w}^k]\Big|_{\zeta=0} = -\frac{1}{2}akc, \qquad \frac{\mathrm{d}\,\mathrm{Re}[\widehat{w}^k]}{\mathrm{d}\zeta}\Bigg|_{\zeta=0} = -\frac{1}{2}ak^2c - \frac{1}{2}ak\left(g\frac{\mathrm{d}\langle u\rangle}{\mathrm{d}\zeta}\right)\Bigg|_{\zeta=0}. \qquad (94a, b)$$

We find that the vertical component of wave orbital velocity w_s (55) initiates a perturbation to the vertical air velocity $\mathrm{Re}[\widehat{w}^k]$ at the wave surface through the Dirichlet boundary condition (94a), and the streamwise component of wave orbital velocity u_s (53) only affects the vertical derivative of $\mathrm{Re}[\widehat{w}^k]$, i.e. $\mathrm{d}\,\mathrm{Re}[\widehat{w}^k]/\mathrm{d}\zeta$, at the wave surface (94b). Away from the wave surface, $\mathrm{Re}[\widehat{w}^k]$ decays monotonically to zero without alternating its sign as shown in figure 28.

Based on the results of $\mathrm{Re}[\widehat{w}]$, the mechanisms for the dominant components of wave-induced streamwise air velocity $\mathrm{Im}[\widehat{u}]$ and air pressure $\mathrm{Im}[\widehat{p}]$ can also be explained. Specifically, $\mathrm{Im}[\widehat{u}]$ arises as a result of mass conservation in response to the $\mathrm{Re}[\widehat{w}]$-associated airflow perturbation, which can be obtained from the continuity equation (69) as

$$\mathrm{Im}[\widehat{u}] = \frac{1}{k}\frac{\mathrm{d}\,\mathrm{Re}[\widehat{w}]}{\mathrm{d}\zeta} + \frac{1}{2}ag\frac{\mathrm{d}\langle u\rangle}{\mathrm{d}\zeta}. \tag{95}$$

Equation (95) explains that the alternating sign of $\mathrm{Im}[\widehat{u}]$ (figure 27*d*) and the associated variation of $\phi_{\widetilde{u}\widetilde{\eta}}$ (figure 26*b*) in the wave boundary layer are because that the effects of u_s on $\mathrm{Im}[\widehat{u}]$ through the Dirichlet boundary condition (53) are limited to the proximity of the wave surface and the behaviour of $\mathrm{Im}[\widehat{u}]$ at higher altitude is determined primarily by the $\mathrm{Re}[\widehat{w}]$-associated airflow. Meanwhile, $\mathrm{Im}[\widehat{p}]$ is generated through the momentum conservation of the $\mathrm{Re}[\widehat{w}]$-associated airflow, which can be seen from the contribution to $\mathrm{Im}[\widehat{p}]$ derived from (68)

$$\mathrm{Im}[\widehat{p}] = \int_{\zeta}^{\infty} (\langle u\rangle - c)k\,\mathrm{Re}[\widehat{w}] + vis., \tag{96}$$

where 'vis' denotes the viscous stress effect and is much smaller compared with the first term on the right hand side. Equation (96) shows that a strong $\mathrm{Re}[\widehat{w}]$ leads to a large-magnitude $\mathrm{Im}[\widehat{p}]$ (figure 27*f*).

As a summary of this subsection, we have discovered that the dominant components of wave-induced velocity and pressure are directly driven by the wave kinematics at the water surface and can be described by the linear models. Based on the split linear models, we have illustrated that the vertical wave motion (w_s) initiates a strong vertical air velocity at the wave surface, which gradually decays away from the wave surface and causes a strong $\mathrm{Re}[\widehat{w}]$ in the airflow. The $\mathrm{Re}[\widehat{w}]$ further results in $\mathrm{Im}[\widehat{u}]$ and $\mathrm{Im}[\widehat{p}]$ in the air through the conservation of mass and momentum, respectively.

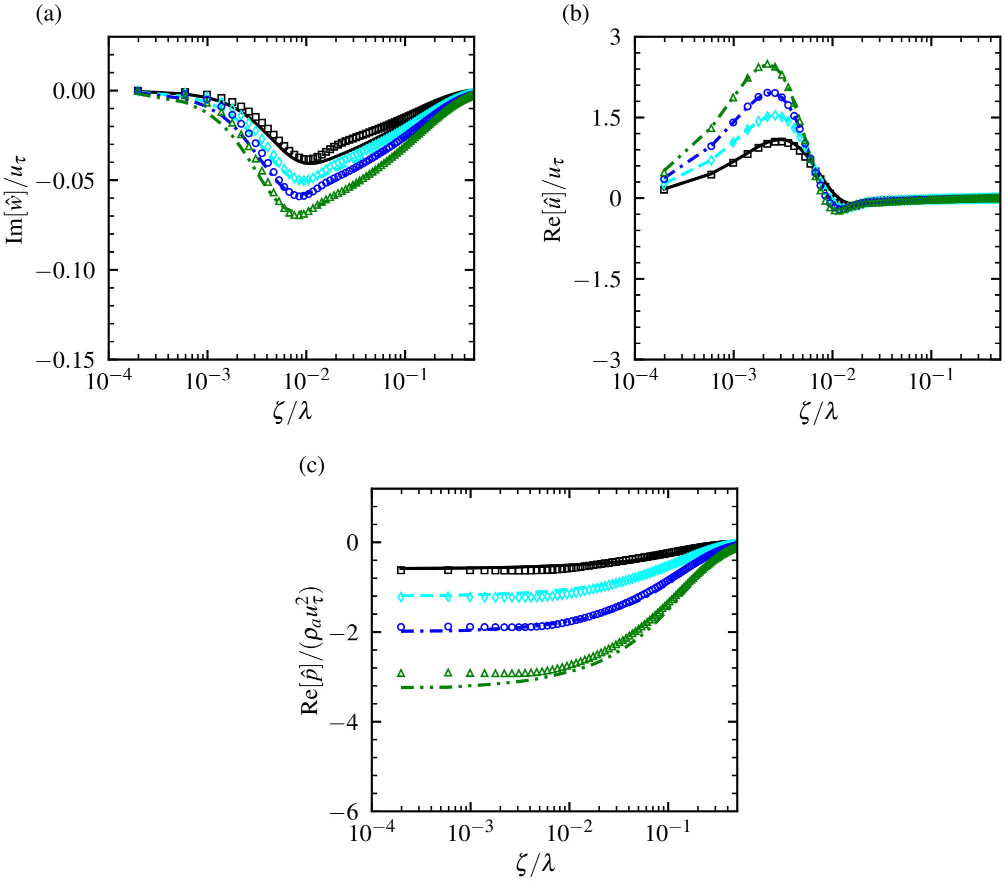

Figure 29: Comparison of the profiles of (a) $\mathrm{Im}[\widehat{w}]$, (b) $\mathrm{Re}[\widehat{u}]$, and (c) $\mathrm{Re}[\widehat{p}]$ between the LES results and the solutions of linear equation (70) for fast waves. Lines are the LES results: —, $c/U_0 = 0.8$; - - -, $c/U_0 = 1.0$; -·-, $c/U_0 = 1.2$; -··, $c/U_0 = 1.4$. Symbols are the linear solutions: □, $c/U_0 = 0.8$; ◇, $c/U_0 = 1.0$; ○, $c/U_0 = 1.2$; △, $c/U_0 = 1.4$. $ak = 0.15$.

3.5.2 Mechanisms for weak components of wave-induced airflow

In the previous subsection, we have explained the arising of $\mathrm{Re}[\widehat{w}]$, $\mathrm{Im}[\widehat{u}]$, and $\mathrm{Im}[\widehat{p}]$, i.e. the dominant components of the fast wave-induced airflow, using the linear equations of wave boundary layer. In this subsection, we further investigate the physical processes producing the weak components $\mathrm{Im}[\widehat{w}]$, $\mathrm{Re}[\widehat{u}]$, and $\mathrm{Re}[\widehat{p}]$. To show the flow dynamics governing these weak components of wave-induced airflow, figure 29 compares the profiles of $\mathrm{Im}[\widehat{w}]$, $\mathrm{Re}[\widehat{u}]$, and $\mathrm{Re}[\widehat{p}]$ between the LES results and the solutions of the linear equation (70) for the fast waves. In all of the four cases shown, the linear solutions agree well with the LES results, suggesting that similar to their strong counterparts, $\mathrm{Im}[\widehat{w}]$, $\mathrm{Re}[\widehat{u}]$, and $\mathrm{Re}[\widehat{p}]$ are also controlled by linear dynamics. For $\widetilde{w}$ and $\widetilde{p}$, compared with $\mathrm{Re}[\widehat{w}]$ and $\mathrm{Im}[\widehat{p}]$ (figures 27*b* and 27*f*), it is found that $|\,\mathrm{Im}[\widehat{w}]| < 0.04|\,\mathrm{Re}[\widehat{w}]|$ and $|\,\mathrm{Re}[\widehat{p}]| < 0.04|\,\mathrm{Im}[\widehat{p}]|$ throughout the boundary layer (figures 29*a* and 29*c*). Therefore, the contributions from $\mathrm{Im}[\widehat{w}]$ and $\mathrm{Re}[\widehat{p}]$ to the magnitude, $|\widehat{w}|$ and $|\widehat{p}|$ (figures 27*a* and 27*e*), and the phase difference, $\phi_{\widetilde{w}\widetilde{\eta}}$ and $\phi_{\widetilde{p}\widetilde{\eta}}$ (figures 26*a* and 26*c*), are negligible. However, for $\widetilde{u}$, $\mathrm{Re}[\widehat{u}]$ (figure 29*b*) is comparable to $\mathrm{Im}[\widehat{u}]$ (figure 27*d*) near the surface, $\zeta/\lambda \le 0.01$, and therefore, $\phi_{\widetilde{u}\widetilde{\eta}}$ (figure 26*b*) varies significantly across this thin region. Away from the wave surface, $\zeta/\lambda \ge 0.01$, $\mathrm{Re}[\widehat{u}]$ becomes negligible compared with $\mathrm{Im}[\widehat{u}]$ and correspondingly, $\phi_{\widetilde{u}\widetilde{\eta}} \approx -\pi$ there (figure 26*b*).

The quasilinear behaviour of the weak components of fast wave-induced airflow shown above suggests that we can use the split linear equations (85) and (88) developed in § 3.4.4 to explain the underlying mechanism. As discussed above, in (85), a strong $\mathrm{Re}[\widehat{w}^k]$ directly results from the airflow perturbation induced by the vertical wave motion and it almost fully determines $\mathrm{Re}[\widehat{w}]$, with near zero contribution from

$\mathrm{Re}[\widehat{w}^f]$ in (88). However, this is not the case for $\mathrm{Im}[\widehat{w}^k]$. To illustrate this point, we first examine the boundary conditions for $\mathrm{Im}[\widehat{w}^k]$, which can be derived from (86) and (87), and read

$$\mathrm{Im}[\widehat{w}^k]\Big|_{\zeta=0} = 0, \qquad \frac{\mathrm{d}\,\mathrm{Im}[\widehat{w}^k]}{\mathrm{d}\zeta}\bigg|_{\zeta=0} = 0. \qquad (97a, b)$$

Equations (97a,b) show that on the contrary to $\mathrm{Re}[\widehat{w}^k]$, $\mathrm{Im}[\widehat{w}^k]$ has homogeneous boundary conditions, indicating that $\mathrm{Im}[\widehat{w}^k]$ is not directly driven by the wave kinematics. Meanwhile, an examination of the expression of (85) shows that $\mathrm{Im}[\widehat{w}^k]$ can be forced by $\mathrm{Re}[\widehat{w}^k]$ and thereby arises in the boundary layer. This can be seen by taking the imaginary part of (85) with respect to its advection term,

$$\frac{\nu}{k}\left[\frac{\mathrm{d}^4}{\mathrm{d}\zeta^4} - 2k^2\frac{\mathrm{d}^2}{\mathrm{d}\zeta^2} + k^4\right]\mathrm{Re}[\widehat{w}^k] + \left[(\langle u\rangle - c)\Big(\frac{\mathrm{d}^2}{\mathrm{d}\zeta^2} - k^2\Big) - \frac{\mathrm{d}^2\langle u\rangle}{\mathrm{d}\zeta^2}\right]\mathrm{Im}[\widehat{w}^k] = 0. \quad (98)$$

Equation (98) shows that it is $\mathrm{Re}[\widehat{w}^k]$ that appears in the viscous term and $\mathrm{Im}[\widehat{w}^k]$ in the advection term for the two components of $\widehat{w}^k$ to be coupled. In other words, because of the wave-induced viscous stress, a strong $\mathrm{Re}[\widehat{w}^k]$ can lead to the arising of $\mathrm{Im}[\widehat{w}^k]$. In (88) for $\widehat{w}^f$, it is shown that similar to $\mathrm{Re}[\widehat{w}^f]$, $\mathrm{Im}[\widehat{w}^f]$ is also driven by the right-hand-side forcing induced by the wave elevation.

Figure 30 shows the comparison among $\mathrm{Im}[\widehat{w}^k]$ solved from (85), $\mathrm{Im}[\widehat{w}^f]$ solved from (88), $\mathrm{Im}[\widehat{w}^k] + \mathrm{Im}[\widehat{w}^f]$, and the $\mathrm{Im}[\widehat{w}]$ result from LES for $ak = 0.1$ and 0.15. As shown, for both wave steepness, $\mathrm{Im}[\widehat{w}^k]$ has a magnitude larger than $\mathrm{Im}[\widehat{w}^f]$. However, the contribution from $\mathrm{Im}[\widehat{w}^f]$ to $\mathrm{Im}[\widehat{w}]$ is still appreciable, especially for the higher wave steepness (figure 30b). These results suggest that the small-magnitude $\mathrm{Im}[\widehat{w}]$ (figure 30a) is mainly generated through the forcing by $\mathrm{Re}[\widehat{w}]$, but also with

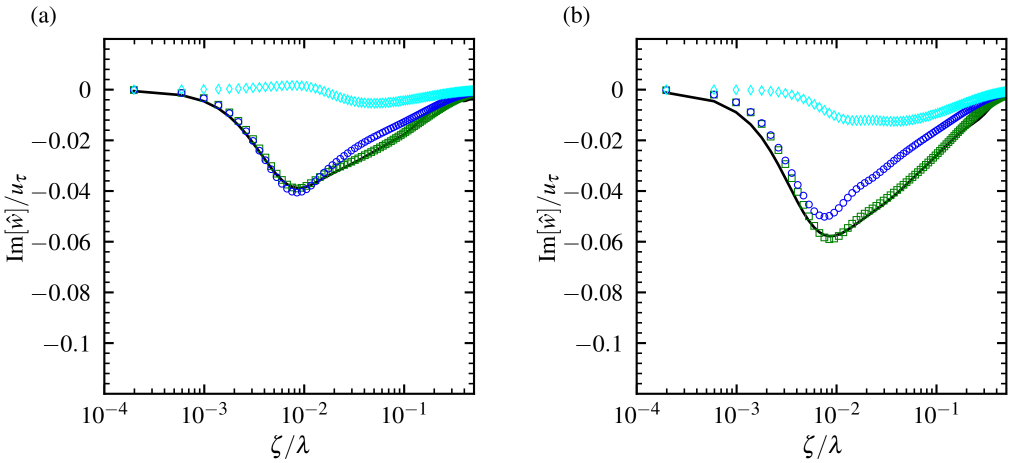

Figure 30: Comparison among $\mathrm{Im}[\widehat{w}^k]$ solved from (85), $\mathrm{Im}[\widehat{w}^f]$ solved from (88), $\mathrm{Im}[\widehat{w}^k] + \mathrm{Im}[\widehat{w}^f]$, and the $\mathrm{Im}[\widehat{w}]$ result from LES for (a) case $(c/U_0, ak) = (1.2, 0.10)$ and (b) case $(c/U_0, ak) = (1.2, 0.15)$. ○, $\mathrm{Im}[\widehat{w}^k]$; ◇, $\mathrm{Im}[\widehat{w}^f]$; □, $\mathrm{Im}[\widehat{w}^k]+\mathrm{Im}[\widehat{w}^f]$; and —, LES result of $\mathrm{Im}[\widehat{w}]$.

an appreciable contribution from the forcing by the wave elevation.

Similar to the dominant components discussed in § 3.5.1, a weak $\mathrm{Im}[\widehat{w}]$ can generate $\mathrm{Re}[\widehat{u}]$ and $\mathrm{Re}[\widehat{p}]$ through the conservation of mass and momentum of the wave-induced airflow, respectively, as

$$\mathrm{Re}[\widehat{u}] = -\frac{1}{k}\frac{\mathrm{d}\,\mathrm{Im}[\widehat{w}]}{\mathrm{d}\zeta}, \tag{99}$$

$$\mathrm{Re}[\widehat{p}] = -\int_{\zeta}^{\infty} (\langle u \rangle - c)k\,\mathrm{Im}[\widehat{w}] + vis., \tag{100}$$

which can be derived from the continuity equation (69) and the vertical momentum equation (68), respectively. Equations (99) and (100) explain the results of figures 29(b) and 29(c), respectively.

As a summary of this subsection, we have shown that the weak components of fast wave-induced airflow can also be described by the linear models. Unlike their strong

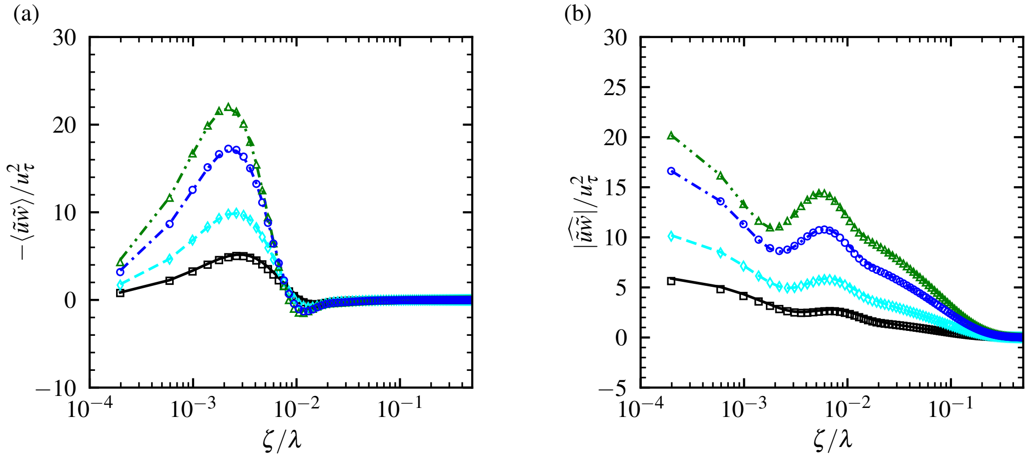

Figure 31: Comparison of (a) $-\langle \widetilde{u}\widetilde{w}\rangle$ and (b) $|\widehat{\widetilde{u}\widetilde{w}}|$ between the LES results and the solutions of linear equation (70) for the fast waves. Lines are the LES results: ——, $c/U_0 = 0.8$; - - -, $c/U_0 = 1.0$; -·-, $c/U_0 = 1.2$; -···, $c/U_0 = 1.4$. Symbols are the linear solutions: □, $c/U_0 = 0.8$; ◇, $c/U_0 = 1.0$; ○, $c/U_0 = 1.2$; △, $c/U_0 = 1.4$. $ak = 0.15$.

counterparts, the weak components have homogeneous boundary conditions and are not directly impacted by the wave kinematics at the water surface. However, with the split linear models, it is discovered that the weak components of wave-induced airflow are forced by their strong counterparts through wave-induced viscous stress and the forcing induced by the wave elevation, and thereby can be generated, too.

3.5.3 Mechanisms for wave-coherent stress and form drag

The proceeding subsections explain the arising of $\widetilde{w}$, $\widetilde{u}$, and $\widetilde{p}$ in the airflow using the linear analysis framework. In this subsection, we analyse the contributions from the strong and weak components of the wave-induced airflow to the wave-coherent stress $-\widetilde{u}\widetilde{w}$ in the wind and the form drag on the wave surface. The $-\widetilde{u}\widetilde{w}$ can be decomposed into a mean component and a fluctuation component as

$$-\widetilde{u}\widetilde{w} = -\langle \widetilde{u}\widetilde{w} \rangle - \widetilde{\widetilde{u}\widetilde{w}} = -\langle \widetilde{u}\widetilde{w} \rangle - \widehat{\widetilde{u}\widetilde{w}}\mathrm{e}^{\mathrm{i}2k\xi} - \widehat{\widetilde{u}\widetilde{w}}^{*}\mathrm{e}^{-\mathrm{i}2k\xi}. \tag{101}$$

Figure 31 compares the profiles of $-\langle \widetilde{u}\widetilde{w} \rangle$ and $|\widehat{\widetilde{u}\widetilde{w}}|$ between the solutions of the viscous linear equation (70) and the LES results, with good agreement obtained. Figure 31(a) shows that $-\langle \widetilde{u}\widetilde{w} \rangle$ is significant only near the surface in the region where $\mathrm{Re}[\widehat{u}]$ (figure 29b) is appreciable, namely $\zeta/\lambda \leq 0.01$, because $-\langle \widetilde{u}\widetilde{w} \rangle = -2(\mathrm{Re}[\widehat{u}]\,\mathrm{Re}[\widehat{w}] + \mathrm{Im}[\widehat{u}]\,\mathrm{Im}[\widehat{w}])$, in which $-2\,\mathrm{Re}[\widehat{u}]\,\mathrm{Re}[\widehat{w}]$ plays a dominant role because $|\,\mathrm{Re}[\widehat{w}]| \gg |\,\mathrm{Im}[\widehat{w}]|$. This result suggests that the weak component of $\widetilde{u}$, i.e. $\mathrm{Re}[\widehat{u}]$, is crucial for generating a mean $-\widetilde{u}\widetilde{w}$ in the wind, i.e. $-\langle \widetilde{u}\widetilde{w} \rangle$. Figure 31($b$) shows that compared with $-\langle \widetilde{u}\widetilde{w} \rangle$, $|\widehat{\widetilde{u}\widetilde{w}}|$ is significant up to a much higher altitude, $\zeta/\lambda \simeq 0.2$, because $|\widehat{\widetilde{u}\widetilde{w}}|$ is dominated by $-\,\mathrm{Im}[\widehat{u}]\,\mathrm{Re}[\widehat{w}]$ (because $|\,\mathrm{Re}[\widehat{w}]| \gg |\,\mathrm{Im}[\widehat{w}]|$) and both $\mathrm{Im}[\widehat{u}]$ and $\mathrm{Re}[\widehat{w}]$ are significant there. Based on this result, we see that the air velocity perturbations directly induced by the vertical wave motion, namely $\mathrm{Im}[\widehat{u}]$ and $\mathrm{Re}[\widehat{w}]$, cause a strong wave-induced fluctuation of $-\widetilde{u}\widetilde{w}$, i.e. $-\widetilde{\widetilde{u}\widetilde{w}}$.

The wave-induced velocity results in $-\widetilde{u}\widetilde{w}$ to affect the momentum transfer within the airflow, and the wave-induced pressure can lead to a form drag on the wave surface, which is the dominant mechanism for the momentum exchange between wind and waves (Belcher & Hunt, 1998). The form drag F_p is defined as

$$F_p = \frac{1}{\rho_a u_\tau^2}\int_0^\lambda \widetilde{p}|_{\zeta=0}\widetilde{\eta}_x \mathrm{d}x = \frac{ak\,\mathrm{Re}[\widehat{p}]}{\rho_a u_\tau^2}\Big|_{\zeta=0}. \tag{102}$$

Equation (102) shows that F_p can only be induced by the weak component of wave-induced pressure, i.e. $\mathrm{Re}[\widehat{p}]$. With F_p on the surface, the resultant wave growth rate

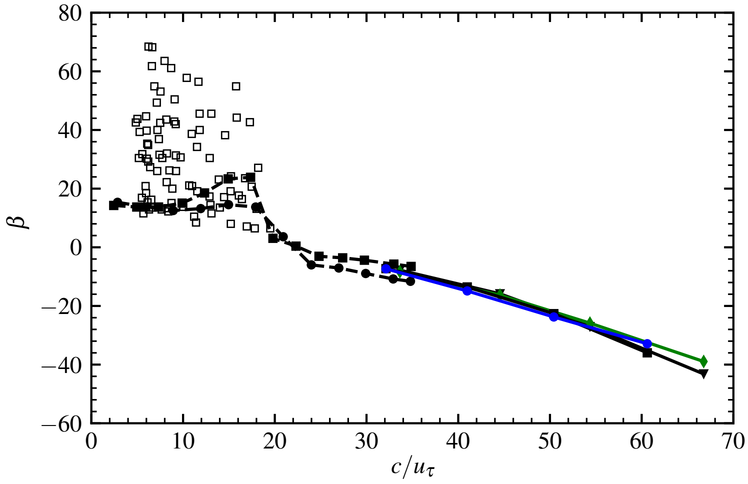

Figure 32: Variation of wave growth rate parameter β (103) as a function of wave age c/u_τ. Data shown are the solutions of (70) for $ak = 0.10$ (—●—) and $ak = 0.15$ (—◆—); the LES results for $ak = 0.10$ (—■—) and $ak = 0.15$ (—▼—); the results of simulations using Reynolds-averaged Navier–Stokes (RANS) equations by Mastenbroek (1996) (-■-); and the results of Cohen (1997) (-●-). As a reference, the values of wave growth rate at low wave age collated by Plant (1982) are also shown (□).

parameter β is (e.g., Li *et al.*, 2000; Donelan, 1999; Yang *et al.*, 2013)

$$\beta = \frac{2F_p}{(ak)^2}, \tag{103}$$

where a positive β corresponds to the wave growth, while a negative β causes the wave to decay.

Figure 32 shows the variation of the wave growth rate parameter β as a function of wave age c/u_τ for all of the fast wave cases in table 2. As shown, the theoretical study of wind over fast wave by Cohen (1997) and the numerical study using Reynolds-averaged Navier–Stokes (RANS) equations by Mastenbroek (1996) investigated the mechanisms for c/u_τ up to about 35. The present study has significantly extended the upper limit of wave age investigated in the literature to $c/u_\tau \approx 67$. The comparison between the LES results and the solutions of linear equation (70) shows good agreement with each other, suggesting that the physical process causing a wind–wave momentum flux at high wave age is governed by the linear dynamics and can be described by the linear equations of wave boundary layer. As a reference, the values of wave growth rate at low wave age collated by Plant (1982) are also included in figure 32. It is shown that the magnitude of wave attenuation rate for $c/u_\tau \gtrsim 45$ is comparable to that of the wave growth rate for $c/u_\tau < 20$, indicating that the strength of wind–wave momentum flux for fast waves can be as large as that for slow waves. This result is reasonable, because for fast waves, although $\mathrm{Re}[\widehat{p}]$ has a magnitude much smaller than $\mathrm{Im}[\widehat{p}]$, it is not small compared with $\rho_a u_\tau^2$ (figure 29*c*), which is the mean total stress in the wind field. Therefore, the form drag and wave attenuation rate induced by $\mathrm{Re}[\widehat{p}]$ is not small for fast waves.

3.5.4 Effects of curvilinear coordinates systems

The proceeding subsections examine the fundamental dynamics of fast wave-induced airflow using the linear equations based on the same curvilinear coordinates as the LES. In this subsection, we analyse the effects of curvilinear coordinates systems on the behaviour of the fast wave-induced airflow. Specifically, we investigate the effects of the mapping function g of the non-orthogonal coordinates (66) and the effects of curvilinear coordinates orthogonality. Figure 33 compares $\widehat{w}$, $\widehat{u}$, and $\widehat{p}$ in case $(c/U_0, ak) = (1.2,\ 0.15)$ among the LES result with $g = \zeta/L_z - 1$, the solution of (70) based on the non-orthogonal mapping (66) with $g = \zeta/L_z - 1$, the solution of (70) based on (66) with $g = -\exp(-k\zeta)$, and the solution of (83) using the orthogonal mapping (79). The other cases have results consistent with the case $(c/U_0, ak) = (1.2,\ 0.15)$ and thus are omitted in the presentation for space consideration. As shown in figure 33, for all of the quantities plotted, the linear solutions using different curvilinear coordinates systems are almost indistinguishable from each other, only with a slight difference among them for $\mathrm{Im}[\hat{u}]$. Specifically, for $\mathrm{Im}[\hat{u}]$, the solution of the non-orthogonal linear equation (70) using $g = -\exp(-k\zeta)$ and that of the orthogonal linear equation (83) are almost identical to each other, which is consistent with the discussion in § 3.4.3 that the dominant terms of the right hand side of these two equations are the same. The $\mathrm{Im}[\hat{u}]$ solved from these two equations are slightly different from that solved from the non-orthogonal linear equation (70) using $g = \zeta/L_z - 1$, because the mapping function g affects $\mathrm{Im}[\hat{u}]$ through the continuity equation as illustrated in (95). Nevertheless, the difference is small.

To conclude § 3.5, we have demonstrated that the fast wave-induced airflow is governed by quasilinear dynamics and can be described by the linear models. Based

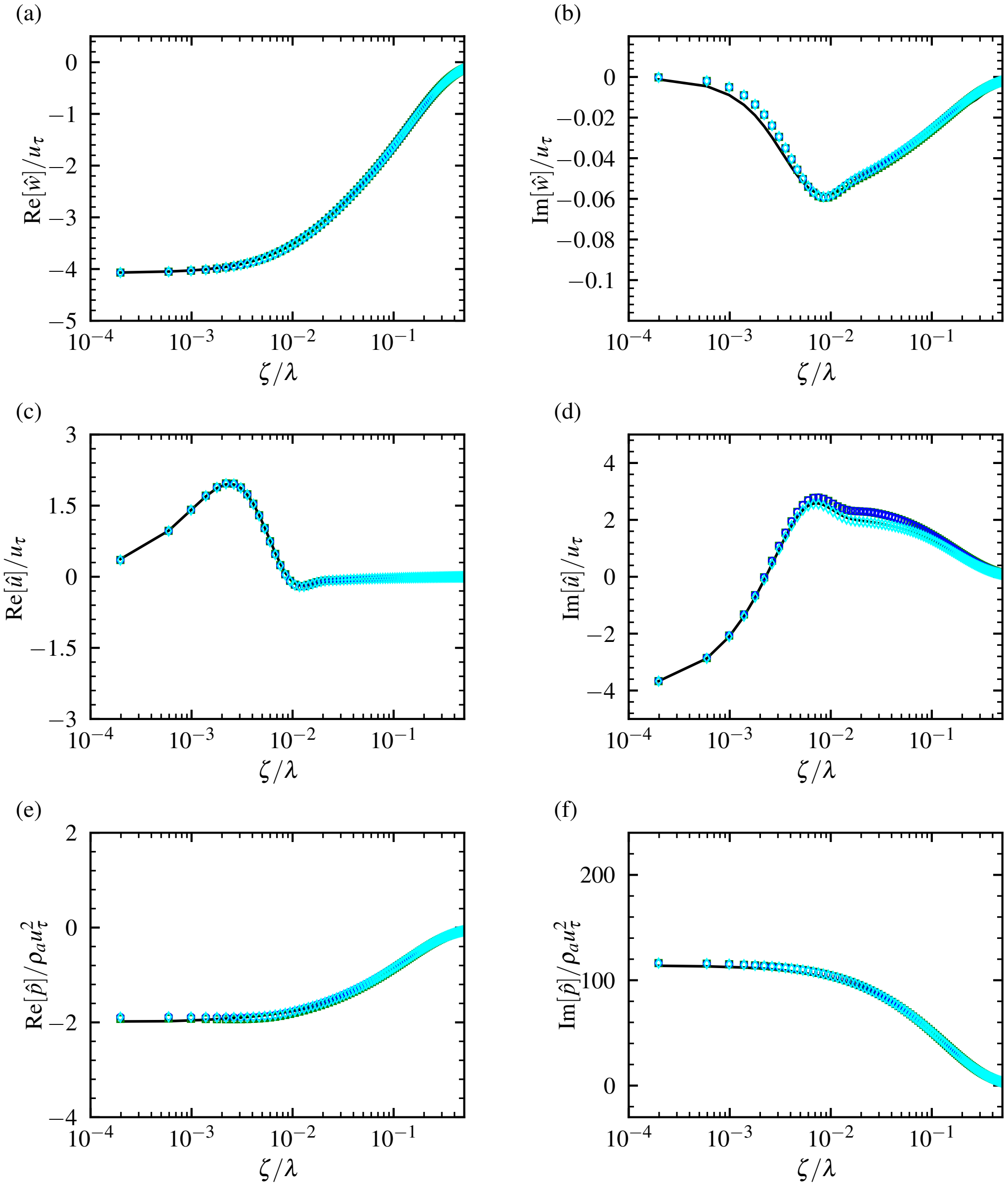

Figure 33: Comparison of $\widehat{w}$, $\widehat{u}$, and $\widehat{p}$ in case $(c/U_0,\, ak) = (1.2,\, 0.15)$ between the LES result and the solutions of linear equations with various curvilinear coordinates systems. The black line (—) denotes the LES result based on the non-orthogonal transformation (66) with $g = \zeta/H - 1$; the diamond (◇) and circle (○) are the solutions of (70) based on the non-orthogonal transformation (66) with $g = \zeta/H - 1$ and with $g = -\exp(-k\zeta)$, respectively; and the square(□) is the solution of (83) based on the orthogonal transformation (79). Note that the circle (○) and square (□) collapse together.

on the split linear model, we have discovered that the dominant components of the wave-induced airflow, namely $\mathrm{Re}[\widehat{w}]$, $\mathrm{Im}[\widehat{u}]$, and $\mathrm{Im}[\widehat{p}]$, are produced by the airflow perturbations directly induced by the vertical component of wave orbital velocity. On the other hand, the weak components, namely $\mathrm{Im}[\widehat{w}]$, $\mathrm{Re}[\widehat{u}]$, and $\mathrm{Re}[\widehat{p}]$, are forced by their strong counterparts and by the forcing induced by the wave elevation, and they cause a wave-induced momentum flux in the airflow and a wind–wave momentum exchange at the wave surface. In a word, the linear analysis framework developed in the present study works well in explaining the fast wave-induced airflow and the underlying mechanisms.

3.6 Conclusions and discussion

In this study, we have performed a numerical and theoretical study on the turbulent wind over fast-moving water waves with wave age higher than that exists in the literature. We have demonstrated that when the wave celerity is comparable to or larger than the wind speed, the effects of wave-induced turbulent stress on the wave-induced airflow become negligibly small. Therefore, the interaction between the wind and the fast waves can be described by the linear equations of wave boundary layer. Below, we summarize our primary findings of the mechanisms underlying the fast wave-induced airflow and remark on future studies.

By performing LES of turbulent wind over fast waves, we have observed that the wave-induced streamwise velocity ($\widetilde{u}$), vertical velocity ($\widetilde{w}$), and pressure ($\widetilde{p}$) in the wind are related to the air motion induced by the vertical wave movement. It is further deduced that for $c \gtrsim U_0$, $\widetilde{w} = O(akU_0)$ and $\widetilde{p} = O(ak\rho_a U_0^2)$ in the wave surface layer. On the other hand, the LES results have shown that the wave-induced turbulent stress has an order of magnitude of $O(u_\tau^2)$. Based on these results, we have performed the scaling analysis on the wave-induced momentum, which suggests that for fast waves, the wave-induced airflow is primarily controlled by the linear forcing.

To confirm the negligible effects of the wave-induced turbulent stress, we have compared the wave-induced airflow in LES with the solution of the linear equation of wave boundary layer based on non-orthogonal curvilinear coordinates developed in our previous study of wind opposing waves in § 2, and good agreement between them has been obtained. This result demonstrates the quasilinear nature of the interaction between turbulent wind and fast waves. Moreover, we have derived a new linear model based on orthogonal curvilinear coordinates, and its solution agrees with that of the non-orthogonal linear equation. The consistency of the solutions of the linear models with different coordinate systems and their agreement with the LES result indicate that the interaction between wind and fast waves can be adequately described by the linear model.

To explain the fundamental dynamics of the fast wave-induced airflow, we split a linear model into two equations corresponding to the effect of wave kinematics and that forced by wave elevation, respectively. Based on the split equations, first we have analysed the arising of the dominant components of the wave-induced airflow, namely $\mathrm{Re}[\widehat{w}]$, $\mathrm{Im}[\widehat{u}]$, and $\mathrm{Im}[\widehat{p}]$, which determine the overall magnitude and structure of $\widetilde{w}$, $\widetilde{u}$, and $\widetilde{p}$, respectively. It is discovered that $\mathrm{Re}[\widehat{w}]$, $\mathrm{Im}[\widehat{u}]$, and $\mathrm{Im}[\widehat{p}]$ are produced by the airflow perturbations directly induced by the vertical component of wave orbital velocity, and they cause the nearly antisymmetric spatial distribution of $\widetilde{w}$ and the nearly symmetric structure of $\widetilde{u}$ and $\widetilde{p}$ observed in the LES. Then we also have elucidated the mechanisms for the weak components of the wave-induced airflow, namely

$\mathrm{Im}[\widehat{w}]$, $\mathrm{Re}[\widehat{u}]$, and $\mathrm{Re}[\widehat{p}]$. Compared with their strong counterparts, $\mathrm{Im}[\widehat{w}]$, $\mathrm{Re}[\widehat{u}]$, and $\mathrm{Re}[\widehat{p}]$ do not affect the magnitude and structure of $\widetilde{w}$, $\widetilde{u}$, and $\widetilde{p}$ noticeably, but they play a central role in generating the momentum flux in the airflow and the wind–wave momentum exchange through the form drag at the wave surface. We have discovered that $\mathrm{Im}[\widehat{w}]$, $\mathrm{Re}[\widehat{u}]$, and $\mathrm{Re}[\widehat{p}]$ are forced by their strong counterparts through the wave-induced viscous stress and by the forcing induced by the wave elevation, and thereby they can arise in the wave boundary layer. We have further illustrated that $\mathrm{Re}[\widehat{u}]$ and $\mathrm{Re}[\widehat{p}]$ result in a mean momentum flux $\langle -\widetilde{u}\widetilde{w} \rangle$ in the airflow and the form drag on the wave surface, respectively.

Next, we compare the fast wave-induced airflow investigated in this section with the opposing wave-induced airflow studied in § 2. First, for fast waves, we have discovered that both the strong and weak components of the wave-induced airflow can be accurately described by the linear models. However, for opposing waves, only the strong components exhibit a quasilinear behaviour and the weak components are significantly affected by the wave-induced turbulent stress, suggesting that the nonlinear forcing remarkably affects the momentum exchange between wind and opposing waves. Second, although for both fast and opposing waves, the strong components of the wave-induced airflow are related to the wave kinematics, they exhibit quite different behaviours. Specifically, away from the wave surface, for fast waves, the wave kinematics-induced airflow decays monotonically, while for opposing waves, it is first amplified by the positive mean velocity shear and then decays.

The fundamental idea of the quasilinear interaction between turbulent wind and fast-moving water waves and the linear analysis framework developed in the present study can be extended to broader settings, such as turbulent flow over a fast-moving flexible wall. The interaction between turbulent flow and a flexible wall is related to fish swimming (e.g., Shen *et al.*, 2003) and turbulent drag reduction (e.g., Akbarzadeh & Borazjani, 2019). Adopting the theoretical analysis framework of the present study to these problems will be our future studies.

4 Concluding Remarks

4.1 Contributions of this thesis

In this thesis, using LES and theoretical analysis, we have investigated the scenarios of turbulent wind–wave interactions that are dominated by linear flow dynamics. Specifically, we found that when the turbulent wind blows over opposing water waves or follows the fast-moving water waves, the dominant wave effects on the airflow are not influenced by the nonlinear forcing, i.e. the wave-induced turbulence stress.

In turbulent wind blowing over opposing water waves, we have derived a linear model for the dominant components of opposing wave-induced airflow. We have also provided the physical insights on the cause of the linear behavior of the dominant opposing wave effects: for the same wave parameters, the wave-induced turbulence stress is much weaker for opposing waves than following waves, whereas the wave-induced velocity is much stronger in the former case, the result of which indicates that under the wind opposing wave condition, the advection induced by wave-induced velocity dominates the wave-induced turbulence stress. To our best knowledge, this process of study is the first systematic study of turbulent wind opposing waves.

For turbulent wind over fast-moving following waves, using scaling analysis, we have shown that when the wave speed is comparable to or faster than the wind speed, the effects of turbulence stress on the wave-induced airflow become negligibly small. In this condition, the arising of fast wave-induced airflow is a quasilinear process and can be entirely described by our linear model. We have also extended our linear analysis framework by developing split equations for the linear model to elucidate the fundamental mechanisms of the fast wave effects in the wind field and the wind–wave momentum exchange. This process of study is the first-ever effort to fully explain structures of the fast wave-induced airflow observed in the literature.

4.2 Future studies

4.2.1 Turbulent wind over slow following waves

Turbulent wind–wave interactions have a variety of conditions. The present study has focused on the scenarios of wind blowing opposing water waves and wind following fast-moving water waves, which are dominated by the linear flow dynamics. However, the scenario of wind following slowly-moving waves is also important and is related to the problem of wave generation by wind. Previous studies have indicated the slow wave-induced airflow is significantly affected by the nonlinear forcing, i.e. the wave-induced turbulence stress (e.g., Belcher & Hunt, 1993; Miles, 1993, 1996). In the past a few decades, theoretical studies have used mixing-length or eddy viscosity models, which turned out can only qualitatively capture the effects of the turbulence stress perturbation. In recent years, although DNS and LES have been widely used to visualize the wave-induced perturbation to the airflow, the modeling of wave-induced turbulence stress has not been improved significantly, as DNS and LES directly solve the highly nonlinear NS equations and thus it is challenging to derive physical relations for the wave-induced turbulence stress from them. Therefore, we propose to use resolvent analysis, which is more realistic than the traditional turbulence models but less complicated than the NS equations, and is particularly suitable for extracting the dominant effects of nonlinear forcing (e.g., Sharma & McKeon, 2013; Luhar *et al.*, 2014). In the resolvent analysis, the wave-induced turbulence stress is emulated by a forcing consisting of various wavenumber–frequency modes. By examining the response of the linearized equation of the wave boundary layer to this forcing, the particular wavenumber–frequency mode that affects the wave-induced velocity most significantly can be identified. Then, the parameterization of the wave-induced turbulence stress reduces to modeling this specific wavenumber–frequency mode, which has much lower complexity than directly modeling the turbulence stress perturbation. The newly proposed model can be further verified using the DNS and LES data of turbulent wind over slow waves.

4.2.2 Effects of aligned angle on turbulent wind–wave interaction

The present study assumes that the aligned angle between wind and water waves is either 180° or 0°. However, in the ocean, the aligned angle can be any values from 0° to 180° (see, e.g., Wright *et al.*, 2001). In the future, the linear analysis framework developed in the present study should be extended to be applicable to the scenario of wind–wave interactions with any aligned angle. More importantly, the boundary between nonlinear and linear regimes of turbulent wind–wave interactions may also vary with the aligned angle. For example, the present study shows that in the case of wind and waves in the same direction, when the wave speed is comparable to or faster than the wind speed, the wave-induced airflow is governed by linear dynamics. However, for wind and waves aligned with a 45° angle, it is expected that when the wave speed is comparable to or faster than $\sqrt{2}/2$ times of wind speed, the wind–wave interaction is controlled by the linear dynamics.

4.2.3 Effects of air stratification on turbulent wind–wave interaction

In this study, we have shown that when the magnitude of wave-induced turbulent stress is small compared to the advection associated with the wave-induced velocity, the wave-induced airflow is governed by the linear dynamics. Previous studies have shown that in turbulent flow, the fluid density variation induced by temperature can affect the intensity of turbulent stress (see, e.g., Fernando, 1991). The fluid temperature is governed by the turbulent transport equation. When the mean gradient of fluid density is opposite to the direction of gravity acceleration, the fluid is stably stratified, and vice versa for the unstable stratification. The stable stratification suppresses the turbulence intensity, whereas it is enhanced by the unstable stratification. Therefore, it is expected that the air stratification can affect the boundary between the linear and nonlinear regimes of turbulent wind–wave interaction, which should be examined in future studies using the present linear analysis framework.

4.2.4 Turbulent wind–wave interaction with multiple wave components

In a broadband wave field, the presence of different wave components can affect the structure of the wave-induced airflow induced by each other, and thereby impact the wind–wave momentum exchange of each other. For example, Jeffreys (1925) found that when the short wave travels through the leeward face of the long wave, it is sheltered from the wind by the long wave and thus it has less chance to grow. Investigating turbulent wind–wave interaction with multiple wave components using the present linear analysis framework should be a topic or future studies.

References

Akbarzadeh, A. M. & Borazjani, I. 2019 Reducing flow separation of an inclined plate via travelling waves. *J. Fluid Mech.* **880**, 831863.

Akervik, E. & Vartdal, M. 2019 The role of wave kinematics in turbulent flow over waves. *J. Fluid Mech.* **880**, 890–915.

Al-Zanaidi, M. A. & Hui, W. H. 1984 Turbulent airflow over water waves – a numerical study. *J. Fluid Mech.* **148**, 225–246.

Anderson, D. A., Tannehill, J. C. & Pletcher, R. H. 1984 *Computational Fluid Mechanics and Heat Transfer*. McGraw-Hill.

Ardhuin, F., Herbers, T. H. C., van Vledder, G. Ph., Watts, K. P., Jensen, R. & Graber, H. C. 2007 Swell and slanting-fetch effects on wind wave growth. *J. Phys. Oceanogr.* **37**, 908–931.

Banner, M. L. 1990 The influence of wave breaking on the surface pressure distribution in wind–wave interactions. *J. Fluid Mech.* **211**, 463–495.

Belcher, S. E. & Hunt, J. C. R. 1993 Turbulent shear flow over slowly moving waves. *J. Fluid Mech.* **251**, 109–148.

Belcher, S. E. & Hunt, J. C. R. 1998 Turbulent flow over hills. *Annu. Rev. Fluid Mech.* **30**, 507–538.

Bowers, J. A., Morton, I. D. & Mould, G. I. 2000 Directional statistics of the winds and waves. *App. Ocean Res.* **22**, 13–30.

Buckles, J., Hanratty, T. J. & Adrian, R. J. 1984 Turbulent flow over large-amplitude wavy surfaces. *J. Fluid Mech.* **140**, 27–44.

Buckley, M. P. & Veron, F. 2016 Structure of the airflow above surface waves. *J. Phys. Oceanogr.* **46**, 1377–1397.

Choi, H. & Moin, P. 2012 Grid-point requirements for large eddy simulation: Chapmans estimates revisited. *Phys. Fluids* **24**, 011702.

Chou, Y. J. & Fringer, O. B. 2010 Consistent discretization for simulations of flows with moving generalized curvilinear coordinates. *Int. J. Numer. Meth. Fluids* **62**, 802–826.

Cohen, J. E 1997 Theory of turbulent wind over fast and slow waves. PhD thesis, University of Cambridge.

Cohen, J. E. & Belcher, S. E. 1999 Turbulent shear flow over fast-moving waves. *J. Fluid Mech.* **386**, 345–371.

Donelan, M. A. 1999 Wind-induced growth and attenuation of laboratory waves. In *Wind-Over-Wave Couplings, Perspectives and Prospects* (ed. S. G. Sajjadi, N. H. Thomas & J. C. R. Hunt). Clarendon.

Donelan, M. A., Babanin, A. V., Young, I. R. & Banner, M. L. 2006 Wave-follower field measurements of the wind-input spectral function. Part II: parameterization of the wind input. *J. Phys. Oceanogr.* **36**, 1672–1689.

Donelan, M. A., Babanin, A. V., Young, I. R., Banner, M. L. & McCormick, C. 2005 Wave-follower field measurements of the wind-input spectral function. Part I: measurements and calibrations. *J. Atmos. Ocean. Technol.* **22**, 799–813.

Drennan, W. M., Kahma, K. K. & Donelan, M. A. 1999 On momentum flux and velocity spectra over waves. *Boundary-Layer Met.* **92**, 489–515.

Druzhinin, O. A., Troitskaya, Y. I. & Zilitinkevich, S. S. 2012 Direct numerical simulation of a turbulent wind over a wavy water surface. *J. Geophys. Res. Oceans* **117**, C00J05.

Druzhinin, O. A., Troitskaya, Y. I. & Zilitinkevich, S. S. 2016 Stably stratified airflow over a waved water surface. Part 1: stationary turbulence regime. *Q. J. R. Met. Soc.* **142**, 759–772.

Fernando, H. J. S. 1991 Turbulent mixing in stratified fluids. *Annu. Rev. Fluid Mech.* **23**, 455–493.

Finnigan, J. J. 1988 Kinetic energy transfer between internal gravity waves and turbulence. *J. Atmos. Sci.* **45**, 486–505.

Germano, M., Piomelli, U., Moin, P. & Cabot, W. H. 1991 A dynamic subgrid-scale eddy viscosity model. *Phys. Fluids A Fluid Dyn.* **3**, 1760–765.

Grachev, A. A. & Fairall, C. W. 2001 Upward momentum transfer in the marine boundary layer. *J. Phys. Oceanogr.* **31**, 1698–1711.

Grare, L., Lenain, L. & Melville, W. K. 2013*a* Wave-coherent airflow and critical layers over ocean waves. *J. Phys. Oceanogr.* **43**, 2156–2172.

Grare, L., Lenain, L. & Melville, W. K. 2018 Vertical profiles of the wave-induced airflow above ocean surface waves. *J. Phys. Oceanogr.* **48**, 2901–2922.

Grare, L., Peirson, W. L., Branger, H., Walker, J. W., Giovanangeli, J.-P. & Makin, V. 2013*b* Growth and dissipation of wind-forced, deep-water waves. *J. Fluid Mech.* **722**, 5–50.

Hanley, K. E. & Belcher, S. E. 2008 Wave-driven wind jets in the marine atmospheric boundary layer. *J. Atmos. Sci.* **65**, 2646–2660.

Hanley, K. E. & Belcher, S. E. 2010 A global climatology of wind–wave interaction. *J. Phys. Oceanogr.* **40**, 1263–1282.

Hao, X. & Shen, L. 2019 Wind–wave coupling study using LES of wind and phase-resolved simulation of nonlinear waves. *J. Fluid Mech.* **874**, 391–425.

Hara, T. & Sullivan, P. P. 2015 Wave boundary layer turbulence over surface waves in a strongly forced condition. *J. Phys. Oceanogr.* **45**, 868–883.

Harris, D. L. 1966 The wave-driven wind. *J. Atmos. Sci.* **23**, 688–693.

Harris, J. A., Fulton, I. & Street, R. L. 1995 Decay of waves in an adverse wind. *Proc. Sixth Asian Congress of Fluid Mechanics, May 22–26, 1995, Singapore* .

Hasselmann, D. & Bsenberg, J. 1991 Field measurements of wave-induced pressure over wind-sea and swell. *J. Fluid Mech.* **230**, 391–428.

Hristov, T., Friehe, C. & Miller, S. 1998 Wave-coherent fields in air flow over ccean waves: identification of cooperative behavior buried in turbulence. *Phys. Rev. Lett.* **81**, 5245–5248.

Hristov, T. & Ruiz-Plancarte, J. 2014 Dynamic balances in a wavy boundary layer. *J. Phys. Oceanogr.* **44**, 3185–3194.

Hristov, T. S., Miller, S. D. & Friehe, C. A. 2003 Dynamical coupling of wind and ocean waves through wave-induced air flow. *Nature* **422**, 55–58.

Hsu, C.-T. & Hsu, E. Y. 1983 On the structure of turbulent flow over a progressive water wave: theory and experiment in a transformed wave-following coordinate system. Part 2. *J. Fluid Mech.* **131**, 123–153.

Hsu, C.-T., Hsu, E. Y. & Street, R. L. 1981 On the structure of turbulent flow over a progressive water wave: theory and experiment in a transformed, wave-following co-ordinate system. *J. Fluid Mech.* **105**, 87–117.

Hussain, A. K. M. F. & Reynolds, W. C. 1970 The mechanics of an organized wave in turbulent shear flow. *J. Fluid Mech.* **41**, 241–258.

Jacobs, S. J. 1987 An asymptotic theory for the turbulent flow over a progressive water wave. *J. Fluid Mech.* **174**, 69–80.

Jeffreys, H. 1925 On the formation of water waves by wind. *Proc. R. Soc. Lond.* **A 107**, 189–206.

Jiang, Q., Sullivan, P., Wang, S., Doyle, J. & Vincent, L. 2016 Impact of swell on air–sea momentum flux and marine boundary layer under low-wind conditions. *J. Atmos. Sci.* **73**, 2683–2697.

Kihara, N., Hanazaki, H., Mizuya, T. & Ueda, H. 2007 Relationship between airflow at the critical height and momentum transfer to the traveling waves. *Phys. Fluids* **19**, 015102.

Knight, D. 1977 Turbulent flow over a wavy boundary. *Boundary-Layer Met.* **11**, 205–222.

Lamb, H. 1932 *Hydrodynamics*. Cambridge University Press.

Li, P., Xu, D. & Taylor, P. 2000 Numerical modelling of turbulent airflow over water waves. *Boundary-Layer Met.* **95**, 397–425.

Lighthill, M. J. 1962 Physical interpretation of the mathematical theory of wave generation by wind. *J. Fluid Mech.* **14**, 385–398.

Lilly, D. K. 1992 A proposed modification of the Germano subgrid-scale closure method. *Phys. Fluids A Fluid Dyn.* **4**, 633–635.

Lin, C. C. 1955 *The Theory of Hydrodynamic Stability*. Cambridge University Press.

Luhar, M., Sharma, A. S. & McKeon, B. J. 2014 On the structure and origin of pressure fluctuations in wall turbulence: predictions based on the resolvent analysis. *J. Fluid Mech.* **751**, 38–70.

Mastenbroek, C. 1996 Wind wave interaction. PhD thesis, Delft Technical University.

Miles, J. W. 1957 On the generation of surface waves by shear flows. *J. Fluid Mech.* **3**, 185–204.

Miles, J. W. 1993 Surface-wave generation revisited. *J. Fluid Mech.* **256**, 427–441.

Miles, J. W. 1996 Surface-wave generation: a viscoelastic model. *J. Fluid Mech.* **322**, 131–145.

Mitsuyasu, H. & Honda, T. 1982 Wind-induced growth of water waves. *J. Fluid Mech.* **123**, 425–442.

Mitsuyasu, H. & Yoshida, Y. 2005 Air–sea interactions under the existence of opposing swell. *J. Oceanogr.* **61**, 141–154.

Orszag, S. A. 1971 Accurate solution of the Orr–Sommerfeld stability equation. *J. Fluid Mech.* **50**, 689–703.

Peirson, W. L., Garcia, A. W. & Pells, S. E. 2003 Water wave attenuation due to opposing wind. *J. Fluid Mech.* **487**, 345–365.

Plant, W. J. 1982 A relationship between wind shear stress and wave slope. *J. Geophys. Res.* **87**, 1961–1967.

Pope, S. B. 2000 *Turbulent Flows*. Cambridge University Press.

Rutgersson, A. & Sullivan, P. P. 2005 The effect of idealized water waves on the turbulence structure and kinetic energy budgets in the overlying airflow. *Dynam. Atmos. Ocean* **38**, 147–171.

Sharma, A. S. & McKeon, B. J. 2013 On coherent structure in wall turbulence. *J. Fluid Mech.* **728**, 196–238.

Shemdin, O. H. & Hsu, E. Y. 1967 Direct measurement of aerodynamic pressure above a simple progressive gravity wave. *J. Fluid Mech.* **30**, 403–416.

Shen, L., Zhang, X., Yue, D. K. P. & Triantafyllou, M. S. 2003 Turbulent flow over a flexible wall undergoing a streamwise travelling wave motion. *J. Fluid Mech.* **484**, 197221.

Smagorinsky, J. 1963 General circulation experiments with the primitive equations. *Monthly Weather Review.* **91**, 99–164.

Smedman, A.-S., Tjernstrm, M. & Hgstrm, U. 1994 The near-neutral marine atmospheric boundary layer with no surface shearing stress: A case study. *J. Atmos. Sci.* **51**, 3399–3411.

Snyder, R. L., Dobson, F. W., Elliott, J. A. & Long, R. B. 1981 Array measurements of atmospheric pressure fluctuations above surface gravity waves. *J. Fluid Mech.* **102**, 1–59.

Sullivan, P. P., Edson, J. B., Hristov, T. & McWilliams, J. C. 2008 Large-eddy simulations and observations of atmospheric marine boundary layers above nonequilibrium surface waves. *J. Atmos. Sci.* **65**, 1225–1245.

Sullivan, P. P. & McWilliams, J. C. 2010 Dynamics of winds and currents coupled to surface waves. *Annu. Rev. Fluid Mech.* **42**, 19–42.

Sullivan, P. P., McWilliams, J. C. & Moeng, C.-H. 2000 Simulation of turbulent flow over idealized water waves. *J. Fluid Mech.* **404**, 47–85.

Van Duin, C. A. & Janssen, P. A. E. M. 1992 An analytic model of the generation of surface gravity-waves by turbulent air-flow. *J. Fluid Mech.* **236**, 197–215.

Veron, F., Saxena, G. & Misra, S. K. 2007 Measurements of the viscous tangential stress in the airflow above wind waves. *Geophys. Res. Lett.* **34**, 1959–1961.

Wang, L.-H., Zhang, W.-Y., Hao, X., Huang, W.-X., Shen, L., Xu, C.-X. & Zhang, Z. 2020 Surface wave effects on energy transfer in overlying turbulent flow. *J. Fluid Mech.* **893**, A21.

Wen, X. & Mobbs, S. 2015 Numerical simulations of air–water flow of a non-linear progressive wave in an opposing wind. *Boundary-Layer Met.* **156**, 91–112.

Wright, C. W., Walsh, E. J., Vandemark, D., Krabill, W. B., Garcia, A. W., Houston, S. H., Powell, M. D., Black, P. G. & Marks, F. D. 2001 Hurricane directional wave spectrum spatial variation in the open ocean. *J. Phys. Oceanogr.* **31**, 2472–2488.

Yang, D., Meneveau, C. & Shen, L. 2013 Dynamic modelling of sea-surface roughness for large-eddy simulation of wind over ocean wavefield. *J. Fluid Mech.* **726**, 62–99.

Yang, D., Meneveau, C. & Shen, L. 2014*a* Effect of downwind swells on offshore wind energy harvesting – a large-eddy simulation study. *Renew. Energy* **70**, 11–23.

Yang, D., Meneveau, C. & Shen, L. 2014*b* Large-eddy simulation of offshore wind farm. *Phys. Fluids* **26**, 025101.

Yang, D. & Shen, L. 2009 Characteristics of coherent vortical structures in turbulent flows over progressive surface waves. *Phys. Fluids* **21**, 125106.

Yang, D. & Shen, L. 2010 Direct-simulation-based study of turbulent flow over various waving boundaries. *J. Fluid Mech.* **650**, 131–180.

YANG, D. & SHEN, L. 2011*a* Simulation of viscous flows with undulatory boundaries. Part I: basic solver. *J. Comput. Phys.* **230**, 5488–5509.

YANG, D. & SHEN, L. 2011*b* Simulation of viscous flows with undulatory boundaries. Part II: Coupling with other solvers for two-fluid computations. *J. Comput. Phys.* **230**, 5510–5531.

YANG, D. & SHEN, L. 2017 Direct numerical simulation of scalar transport in turbulent flows over progressive surface waves. *J. Fluid Mech.* **819**, 58–103.

YOUNG, I. R. & SOBEY, R. J. 1985 Measurements of the wind–wave energy flux in an opposing wind. *J. Fluid Mech.* **151**, 427–442.

YOUSEFI, K. & VERON, F. 2020 Boundary layer formulations in orthogonal curvilinear coordinates for flow over wind-generated surface waves. *J. Fluid Mech.* **888**, A11.

YOUSEFI, K., VERON, F. & BUCKLEY, M. P. 2020 Momentum flux measurements in the airflow over wind-generated surface waves. *J. Fluid Mech.* **895**, A15.

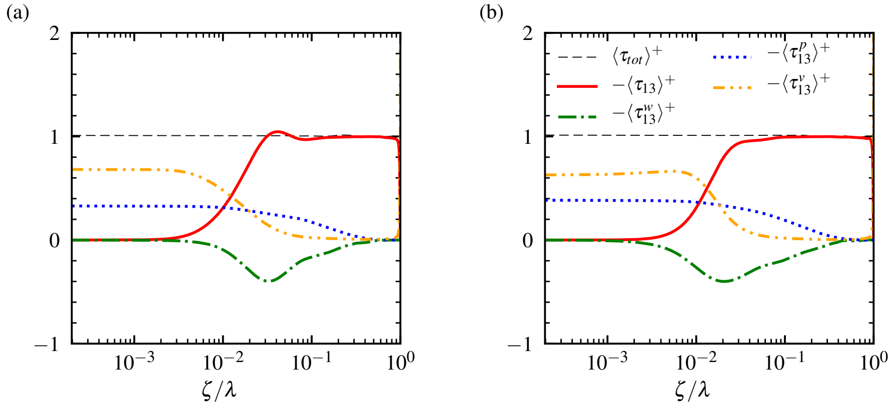

Figure 34: Profiles of the stress terms in (104) for cases (a) WOW01 and (b) WOW04. The superscript '+' denotes normalisation by u_τ^2.

A Conservation of momentum in LES of wind opposing waves

In this appendix, we examine the momentum conservation of the numerical scheme employed in § 2. As indicated by (20), the summation of viscous stress $-\langle\tau^v_{13}\rangle$, turbulent stress $-\langle\tau_{13}\rangle$, wave-induced stress $-\langle\tau^w_{13}\rangle$ and wave-induced pressure $-\langle\tau^p_{13}\rangle$ should equal to the driving force u_τ^2 throughout the wave boundary layer

$$\langle\tau_{tot}\rangle = -\langle\tau^v_{13}\rangle - \langle\tau_{13}\rangle - \langle\tau^w_{13}\rangle - \langle\tau^p_{13}\rangle = u_\tau^2. \tag{104}$$

In figure 34, we plot the stress terms normalised by u_τ^2 in the two steep opposing wave cases, WOW01 and WOW04 (table 1). As shown, the normalised total stress $\langle\tau_{tot}\rangle$ equals to 1 at all heights in both cases. Quantitatively, the difference of $\langle\tau_{tot}\rangle$ between the wave surface and top of simulation domain, i.e. $|\langle\tau_{tot}\rangle(\zeta = 0) - \langle\tau_{tot}\rangle(\zeta = \lambda)|$, is 0.0022 in WOW01 and 0.0045 in WOW04, which is negligibly small and indicates

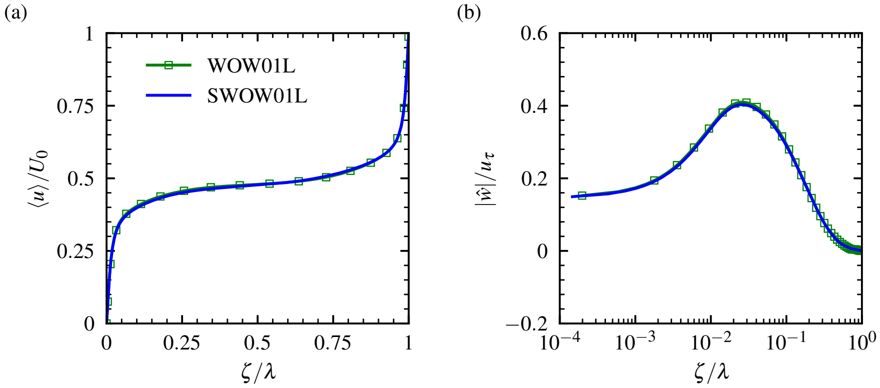

Figure 35: Comparison of (a) the mean wind speed $\langle u \rangle$ and (b) the magnitude of wave-coherent vertical velocity $|\widehat{w}|$ between case WOW01L and case SWOW01L.

the conservation of momentum in the simulation.

B Grid convergence of LES of wind opposing waves

In this appendix, we show the grid convergence in the simulation results of § 2. In figure 35, we compare the profiles of the mean wind speed $\langle u \rangle$ and magnitude of wave-induced vertical velocity $|\widehat{w}|$ between case WOW01L and case SWOW01L of the same physical parameters, with case SWOW01L at a super resolution as summarised in table 1. As shown, the results between the two cases are almost indistinguishable from each other, indicating that the grid resolution adopted in the present study is sufficient to capture the flow dynamics. Comparisons of other quantities (not plotted due to space consideration) also show grid convergence.

C Derivation of non-orthogonal linearised equations using strongly conservative LES equations

From the strongly conservative LES equations in the mapped computational curvilinear coordinate, i.e. (16) and (17), the momentum and continuity equations for the wave-induced airflow can be derived, i.e. (22) and (23), respectively, in which the curvilinear coordinate velocity U_j and the products of physical quantities and grid transformation terms in the wave-induced pressure stress $\widetilde{\tau}^p_{jk}$ and the wave-induced viscous stress $\widetilde{\tau}^v_{jk}$ make it challenging to understand the underlying physics. In this section, the linearised equations for the wave-induced airflow are derived by using the Cartesian quantities to express the leading-order terms of U_j and $\widetilde{\tau}^p_{jk}$ in § C.1, and of $\widetilde{\tau}^v_{jk}$ in §§ C.2 and C.3.

C.1 Linearisation of curvilinear coordinate velocity and wave-induced pressure stress

In this subsection, we apply the properties of the wave-induced quantities and use the Cartesian variables to express the curvilinear coordinate velocity U_j and the wave-induced pressure stress $\widetilde{\tau}^p_{jk}$ in the wave-induced momentum equation (22). In the wave following frame $\xi - ct$, the grid transformation terms, which appear in the equations of the wave-induced airflow, do not vary with time. We have

$$\eta = \overline{\eta} = \widetilde{\eta}, \tag{105}$$

$$\zeta_x = \overline{\zeta_x} = \frac{g\widetilde{\eta}_\xi}{1 - g_\varsigma\widetilde{\eta}}, \qquad \zeta_y = \overline{\zeta_y} = \frac{g\widetilde{\eta}_\psi}{1 - g_\varsigma\widetilde{\eta}}, \qquad \zeta_z = \overline{\zeta_z} = \frac{1}{1 - g_\varsigma\widetilde{\eta}}, \tag{106}$$

where η is the wave surface, and ζ_x, ζ_y, and ζ_z are the geometrical transformation terms defined in (8). Here, $\overline{(\cdot)}$ and $\widetilde{(\cdot)}$ are the phase-averaged and wave-induced quantities, respectively, defined in § 2.2.2.

To simplify the products of the velocity components and grid transformation terms, we utilize the following properties of the phase average (Finnigan, 1988),

$$\overline{f_1\widetilde{f_2}} = \overline{f_1}\widetilde{f_2}, \qquad \overline{\langle f_1\rangle f_2} = \langle f_1\rangle \overline{f_2}, \tag{107}$$

where f_1 and f_2 are two arbitrary physical quantities, and $\langle\cdot\rangle$ denotes average in time and over the (ξ, ψ) plane. It is also worth noting that the correlation between a wave-induced quantity and the surface elevation or slope does not have direct contributions to a wave-induced quantity, because

$$\begin{aligned}
\widetilde{f}\widetilde{\eta} &= (\widehat{f}\mathrm{e}^{\mathrm{i}k\xi} + \widehat{f}^*\mathrm{e}^{-\mathrm{i}k\xi})(\widehat{\eta}\mathrm{e}^{\mathrm{i}k\xi} + \widehat{\eta}^*\mathrm{e}^{-\mathrm{i}k\xi}) \\
&= 2\,\mathrm{Re}[\widehat{f}\widehat{\eta}^*] + 2\,\mathrm{Re}[\widehat{f}\widehat{\eta}\mathrm{e}^{\mathrm{i}2k\xi}], \qquad (108) \\
\widetilde{f}\widetilde{\eta}_\xi &= (\widehat{f}\mathrm{e}^{\mathrm{i}k\xi} + \widehat{f}^*\mathrm{e}^{-\mathrm{i}k\xi})(\mathrm{i}k\widehat{\eta}\mathrm{e}^{\mathrm{i}k\xi} - \mathrm{i}k\widehat{\eta}^*\mathrm{e}^{-\mathrm{i}k\xi}) \\
&= 2\,\mathrm{Re}[\mathrm{i}k\widehat{f}^*\widehat{\eta}] + 2\,\mathrm{Re}[\mathrm{i}k\widehat{f}\widehat{\eta}\mathrm{e}^{\mathrm{i}2k\xi}], \qquad (109)
\end{aligned}$$

where $\widetilde{f}$ is an arbitrary wave-induced quantity. As illustrated in (108) and (109), both $\widetilde{f}\widetilde{\eta}$ and $\widetilde{f}\widetilde{\eta}_\xi$ have two components, one with a zero wavenumber corresponding to the mean and the other corresponding to the harmonic with a wavenumber of $2k$, and thus they have no direct contributions to the wave-coherent fluctuation with a wavenumber k.

Using (105)–(107), the phase-averaged curvilinear coordinate velocity, which is defined in (16) and (17), can be represented as

$$\begin{aligned}\overline{U} &= \overline{J^{-1}u_j\frac{\partial\xi}{\partial\xi_j}} = \overline{u-c} - \overline{(u-c)g_\zeta\widetilde{\eta}} = (\overline{u}-c)(1-g_\zeta\widetilde{\eta}), && (110)\\ \overline{W} &= \overline{J^{-1}u_j\frac{\partial\zeta}{\partial\xi_j}} = \overline{(u-c)g\widetilde{\eta}_\xi} + \overline{w} = (\overline{u}-c)g\widetilde{\eta}_\xi + \overline{w}, && (111)\end{aligned}$$

where $J = \zeta_z$ is the determinant of the transformation matrix $\boldsymbol{J}$, defined in (8). The last step in deriving $\overline{U}$ and $\overline{W}$ has utilized the fact that $g = \langle g\rangle$ and $g_\zeta = \langle g_\zeta\rangle$. We can obtain the mean curvilinear coordinate velocity by averaging (110) and (111) over the (ξ,ψ) plane

$$\begin{aligned}\langle U\rangle &= \langle(\overline{u}-c)(1-g_\zeta\widetilde{\eta})\rangle = \langle u\rangle - c + 2\,\mathrm{Re}[g_\zeta\widehat{u}\widehat{\eta}^*], && (112)\\ \langle W\rangle &= \langle(\overline{u}-c)g\widetilde{\eta}_\xi + \overline{w}\rangle = \langle w\rangle + 2\,\mathrm{Re}[gik\widehat{u}^*\widehat{\eta}], && (113)\end{aligned}$$

where (108) and (109) are applied. Considering that $\widetilde{u}_i = O(ak)$, $\widetilde{\eta} = O(ak)$, and that the mean quantities are of $O(1)$, one can deduce that $2\,\mathrm{Re}[g_\zeta\widehat{u}\widehat{\eta}^*]$ and $2\,\mathrm{Re}[gik\widehat{u}^*\widehat{\eta}]$ are of $O((ak)^2)$, which are high-order corrections to the mean velocity. The wave-correlated curvilinear coordinate velocity is obtained by subtracting its mean value from its phase-averaged value,

$$\begin{aligned}\widetilde{U} &= \overline{U} - \langle U\rangle = \widetilde{u} - (\langle u\rangle - c)g_\zeta\widetilde{\eta}, && (114)\\ \widetilde{W} &= \overline{W} - \langle W\rangle = \widetilde{w} + (\langle u\rangle - c)g\widetilde{\eta}_\xi, && (115)\end{aligned}$$

where the terms related to $\widetilde{u}\widetilde{\eta}$ and $\widetilde{u}\widetilde{\eta}_\xi$ do not present because they do not contribute to the wave-induced fluctuation as illustrated in (108) and (109).

Using (105)–(109), we can express the wave-induced pressure stress $\widetilde{\tau}^p_{ij}$ by eliminating the grid transformation terms,

$$
\begin{aligned}
\widetilde{\tau}^p_{11} &= \overline{J^{-1}p\xi_x} - \langle J^{-1}p\xi_x\rangle = \overline{p(1-g_\zeta\widetilde{\eta})} - \langle p(1-g_\zeta\widetilde{\eta})\rangle = \widetilde{p}, && (116)\\
\widetilde{\tau}^p_{13} &= \overline{J^{-1}p\zeta_x} - \langle J^{-1}p\zeta_x\rangle = \overline{pg\widetilde{\eta}_\xi} - \langle pg\widetilde{\eta}_\xi\rangle = \langle p\rangle g\widetilde{\eta}_\xi = 0, && (117)\\
\widetilde{\tau}^p_{31} &= \overline{J^{-1}p\xi_z} - \langle J^{-1}p\xi_z\rangle = 0, && (118)\\
\widetilde{\tau}^p_{33} &= \overline{J^{-1}p\zeta_z} - \langle J^{-1}p\zeta_z\rangle = \overline{p} - \langle p\rangle = \widetilde{p}, && (119)
\end{aligned}
$$

where $\langle p\rangle = 0$ and $\xi_z = 0$ are applied.

To simplify the wave-induced momentum equation (22), (112)–(113) and (114)–(115) are employed to replace the mean curvilinear coordinate velocity $\langle U_j\rangle$ and the wave-induced curvilinear coordinate velocity $\widetilde{U}_j$, respectively, and (116)–(119) are used to express the wave-induced pressure stress $\widetilde{\tau}^p_{jk}$. With (114) and (115), the wave-induced continuity equation (23) can be represented as

$$
\frac{\partial\widetilde{u}}{\partial\xi} + \frac{\partial\widetilde{w}}{\partial\zeta} + \frac{\mathrm{d}\langle u\rangle}{\mathrm{d}\zeta}g\widetilde{\eta}_\xi = 0 + O((ak)^2), \qquad (120)
$$

where $O((ak)^2)$ denotes the neglected high-order contributions to the mean curvilinear coordinate velocity.

C.2 Linearisation of products of velocity derivatives and grid transformation terms

In this subsection, we show how to extract the leading-order terms in the phase-averaged products of the velocity derivatives and the grid transformation terms by employing (105)–(109). The products frequently appear in the wave-induced viscous stress $\widetilde{\tau}^v_{jk}$ in the momentum equation of the wave-induced airflow, i.e. (22) in § 2. The simplification of $\widetilde{\tau}^v_{jk}$ is further discussed in the subsequent section.

First, we simplify the phase-averaged products of the determinant of the transformation Jacobian and the velocity derivatives, i.e. $1/J \cdot \partial u_j/\partial x$ and $1/J \cdot \partial u_j/\partial z$,

$$\begin{aligned}
\overline{\frac{1}{J}\frac{\partial u_j}{\partial x}} &= \overline{\Big(\frac{\partial u_j}{\partial \xi} + \frac{\partial u_j}{\partial \zeta}\overline{\zeta_x}\Big)/\overline{\zeta_z}} = \frac{\partial \overline{u}_j}{\partial \xi} - \frac{\partial \overline{u}_j}{\partial \xi} g_\zeta \widetilde{\eta} + \frac{\partial \overline{u}_j}{\partial \zeta} g \widetilde{\eta}_\xi, && (121)\\
\overline{\frac{1}{J}\frac{\partial u_j}{\partial z}} &= \overline{\frac{\partial u_j}{\partial \zeta}\overline{\zeta_z}/\overline{\zeta_z}} = \frac{\partial \overline{u}_j}{\partial \zeta}. && (122)
\end{aligned}$$

We then simplify the phase-averaged products of the determinant of the transformation Jacobian, the streamwise derivatives of the velocity, and the transformation terms, i.e. $1/J \cdot \partial u_j/\partial x \cdot \zeta_x$ and $1/J \cdot \partial u_j/\partial x \cdot \zeta_z$, as the following

$$\begin{aligned}
\overline{\frac{1}{J}\frac{\partial u_j}{\partial x}\zeta_x} &= \frac{\partial \overline{u}_j}{\partial \xi} g\widetilde{\eta}_\xi + \overline{\frac{\partial u_j}{\partial \zeta}\frac{g^2\widetilde{\eta}_\xi^2}{1 - g_\zeta \widetilde{\eta}}} = \frac{\partial \overline{u}_j}{\partial \xi} g\widetilde{\eta}_\xi + O\Big((ak)^2 \frac{\partial \overline{u}_j}{\partial \zeta}\Big), && (123)\\
\overline{\frac{1}{J}\frac{\partial u_j}{\partial x}\zeta_z} &= \frac{\partial \overline{u}_j}{\partial \xi} + \overline{\frac{\partial u_j}{\partial \zeta} g\widetilde{\eta}_\xi + \frac{\partial u_j}{\partial \zeta}\frac{g g_\zeta \widetilde{\eta}_\xi \widetilde{\eta}}{1 - g_\zeta \widetilde{\eta}}} = \frac{\partial \overline{u}_j}{\partial \xi} + \frac{\partial \overline{u}_j}{\partial \zeta} g\widetilde{\eta}_\xi \\
&+ O\Big((ak)^2 \frac{\partial \overline{u}_j}{\partial \zeta}\Big), && (124)
\end{aligned}$$

where we replace all the grid transformation terms related to $\widetilde{\eta}_\xi \widetilde{\eta}$ and $\widetilde{\eta}_\xi^2$ with $O((ak)^2)$ by considering that η is of $O(ak)$ and g is of $O(1)$. Similarly, the phase-averaged products of the determinant of the transformation Jacobian, the vertical derivatives of the velocity, and the transformation terms, i.e. $1/J \cdot \partial u_j/\partial z \cdot \zeta_x$ and $1/J \cdot \partial u_j/\partial z \cdot \zeta_z$, can be simplified as

$$\begin{aligned}
\overline{\frac{1}{J}\frac{\partial u_j}{\partial z}\zeta_x} &= \overline{\frac{\partial u_j}{\partial \zeta}\frac{g\widetilde{\eta}_\xi}{1-g_\zeta\widetilde{\eta}}} = \overline{\frac{\partial u_j}{\partial \zeta}g\widetilde{\eta}_\xi + \frac{\partial u_j}{\partial \zeta}\frac{gg_\zeta\widetilde{\eta}_\xi\widetilde{\eta}}{1-g_\zeta\widetilde{\eta}}} = \frac{\partial \overline{u}_j}{\partial \zeta}g\widetilde{\eta}_\xi \\
&+ O\Big((ak)^2\frac{\partial \overline{u}_j}{\partial \zeta}\Big), \qquad (125) \\
\overline{\frac{1}{J}\frac{\partial u_j}{\partial z}\zeta_z} &= \overline{\frac{\partial u_j}{\partial \zeta}\frac{1}{1-g_\zeta\widetilde{\eta}}} = \overline{\frac{\partial u_j}{\partial \zeta} + \frac{\partial u_j}{\partial \zeta}g_\zeta\widetilde{\eta} + \frac{\partial u_j}{\partial \zeta}\frac{g_\zeta^2\widetilde{\eta}^2}{1-g_\zeta\widetilde{\eta}}} \\
&= \frac{\partial \overline{u}_j}{\partial \zeta} + \frac{\partial \overline{u}_j}{\partial \zeta}g_\zeta\widetilde{\eta} + O\Big((ak)^2\frac{\partial \overline{u}_j}{\partial \zeta}\Big), \qquad (126)
\end{aligned}$$

where the grid transformation terms with $\widetilde{\eta}^2$, $\widetilde{\eta}_\xi\widetilde{\eta}$, and $\widetilde{\eta}_\xi^2$ are of $O((ak)^2)$, similar to (123) and (124). In (121)–(126), the equations are expanded up to $O((ak)^2)$ to capture the dominant physical processes. In the subsequent section, (121)–(126) are employed to simplify the wave-induced viscous stress $\widetilde{\tau}^v_{jk}$ in (22).

C.3 Linearisation of wave-induced viscous stress

In this subsection, we show how to obtain the leading-order terms of the wave-induced viscous stress $\widetilde{\tau}^v_{jk}$ in (22), by employing the relationships (121)–(126) derived in § C.2. With (121), the phase-averaged τ^v_{11} is represented as

$$\overline{\tau}^v_{11} = \nu\overline{\frac{1}{J}2\frac{\partial u}{\partial x}} = 2\nu\frac{\partial \overline{u}}{\partial \xi} - 2\nu\frac{\partial \overline{u}}{\partial \xi}g_\zeta\widetilde{\eta} + 2\nu\frac{\partial \overline{u}}{\partial \zeta}g\widetilde{\eta}_\xi, \qquad (127)$$

and the wave-induced τ^v_{11} is obtained as

$$\widetilde{\tau}^v_{11} = \overline{\tau}^v_{11} - \langle\tau^v_{11}\rangle = 2\nu\frac{\partial \widetilde{u}}{\partial \xi} - 2\nu\frac{\partial\langle u\rangle}{\partial \xi}\widetilde{\eta} + 2\nu\frac{\partial\langle u\rangle}{\partial \zeta}g\widetilde{\eta}_\xi = -2\nu\frac{\partial \widetilde{w}}{\partial \zeta}, \qquad (128)$$

where $\partial\langle u\rangle/\partial\xi = 0$ and the continuity equation (120) are applied. With (123), (124), and (126), the phase-averaged τ^v_{13} is simplified as

$$\begin{aligned}\overline{\tau}^v_{13} = 2\nu\Big(\frac{\partial\overline{u}}{\partial\xi}g\widetilde{\eta}_\xi + O\Big(\nu(ak)^2\frac{\partial\overline{u}}{\partial\zeta}\Big)\Big) + \nu\Big(\frac{\partial\overline{u}}{\partial\zeta} + \frac{\partial\overline{u}}{\partial\zeta}g_\zeta\widetilde{\eta} + O\Big((ak)^2\nu\frac{\partial\overline{u}}{\partial\zeta}\Big)\Big) \\ +\nu\Big(\frac{\partial\overline{w}}{\partial\xi} + \frac{\partial\overline{w}}{\partial\zeta}g\widetilde{\eta}_\xi + O\Big((ak)^2\nu\frac{\partial\overline{w}}{\partial\zeta}\Big)\Big) \\ = \nu\Big(\frac{\partial\overline{u}}{\partial\zeta} + \frac{\partial\overline{w}}{\partial\xi}\Big) + \nu\frac{\partial\overline{u}}{\partial\zeta}g_\zeta\widetilde{\eta} + \nu\frac{\partial\overline{w}}{\partial\zeta}g\widetilde{\eta}_\xi + 2\nu\frac{\partial\overline{u}}{\partial\xi}g\widetilde{\eta}_\xi + O\Big((ak)^2\nu\Big(\frac{\partial\overline{u}}{\partial\zeta} + \frac{\partial\overline{w}}{\partial\zeta}\Big)\Big),\end{aligned} \tag{129}$$

and the wave-induced τ^v_{13} is expressed as

$$\widetilde{\tau}^v_{13} = \overline{\tau}^v_{13} - \langle\tau^v_{13}\rangle = \nu\Big(\frac{\partial\widetilde{u}}{\partial\zeta} + \frac{\partial\widetilde{w}}{\partial\xi}\Big) + \nu\frac{\mathrm{d}\langle u\rangle}{\mathrm{d}\zeta}g_\zeta\widetilde{\eta} + O\Big((ak)^2\nu\Big(\frac{\partial\widetilde{u}}{\partial\zeta} + \frac{\partial\widetilde{w}}{\partial\zeta}\Big)\Big), \tag{130}$$

where $\partial\langle u\rangle/\partial\xi = 0$ and $\langle w\rangle = 0$ are applied. Using (121) and (122), the phase-averaged τ^v_{31} and wave-induced τ^v_{31} can be expressed as

$$\overline{\tau}^v_{31} = \nu\overline{\frac{1}{J}\frac{\partial u}{\partial z}} + \nu\overline{\frac{1}{J}\frac{\partial w}{\partial x}} = \nu\frac{\partial\overline{u}}{\partial\zeta} + \nu\Big(\frac{\partial\overline{w}}{\partial\xi} - \frac{\partial\overline{w}}{\partial\xi}g_\zeta\widetilde{\eta} + \frac{\partial\overline{w}}{\partial\zeta}g\widetilde{\eta}_\xi\Big), \tag{131}$$

$$\widetilde{\tau}^v_{31} = \overline{\tau}^v_{31} - \langle\tau^v_{31}\rangle = \nu\Big(\frac{\partial\widetilde{u}}{\partial\zeta} + \frac{\partial\widetilde{w}}{\partial\xi}\Big), \tag{132}$$

where $\langle w\rangle = 0$ and $\xi_z = 0$ are applied. With (123), (125), and (126), the phase-averaged τ^v_{33} is represented as

$$\begin{aligned}\overline{\tau}^v_{33} &= \nu\Big(\frac{\partial\overline{u}}{\partial\zeta}g\widetilde{\eta}_\xi + O\Big((ak)^2\nu\frac{\partial\overline{u}}{\partial\zeta}\Big)\Big) + \nu\Big(\frac{\partial\overline{w}}{\partial\xi}g\widetilde{\eta}_\xi + O\Big((ak)^2\nu\frac{\partial\overline{w}}{\partial\zeta}\Big)\Big) \\ &+ 2\nu\Big(\frac{\partial\overline{w}}{\partial\zeta} + \frac{\partial\overline{w}}{\partial\zeta}g_\zeta\widetilde{\eta} + O\Big((ak)^2\nu\frac{\partial\overline{w}}{\partial\zeta}\Big)\Big) \\ &= \nu\frac{\partial\overline{w}}{\partial\zeta} - \nu\frac{\partial\overline{u}}{\partial\xi} + O\Big((ak)^2\nu\Big(\frac{\partial\overline{w}}{\partial\zeta} + \frac{\partial\overline{u}}{\partial\zeta}\Big)\Big),\end{aligned} \tag{133}$$

where the continuity equation (120) is utilized in the last step and the wave-induced τ_{33}^{v} is obtained as

$$\widetilde{\tau}_{33}^{v} = -\nu \frac{\partial \widetilde{u}}{\partial \xi} + \nu \frac{\partial \widetilde{w}}{\partial \zeta} + O\Big((ak)^2 \nu \Big(\frac{\partial \widetilde{w}}{\partial \zeta} + \frac{\partial \widetilde{u}}{\partial \zeta} \Big) \Big). \tag{134}$$

Equations (128), (130), (132), and (134) are employed to represent the wave-induced viscous stress $\widetilde{\tau}_{jk}^{v}$ in (22).

To conclude § C, we have linearised the mean curvilinear coordinate velocity $\langle U_j \rangle$, the wave-induced curvilinear coordinate velocity $\widetilde{U}_j$, and the wave-induced pressure stress $\widetilde{\tau}_{jk}^{p}$ in § C.1, and the wave-induced viscous stress $\widetilde{\tau}_{jk}^{v}$ has been linearised in §§ C.2 and C.3. These results are used to simplify the equations for the wave-induced airflow, i.e. (22) and (23), and the resultant linearised equations for the wave-induced airflow are (24)–(26).

D Derivation of non-orthogonal linearised equations using weakly conservative LES equations

In this section, we derive the viscous linearised equations for the wave-induced airflow from the weakly conservative LES equations in the mapped computational curvilinear coordinates, i.e. (10) and (11). Because some derivation details are similar to those in § C, we only show the key steps of the derivation in this section. The phase-averaged weakly conservative LES equations in the wave following frame read

$$
\begin{aligned}
(\overline{u}-c)\Big(\frac{\partial \overline{u}}{\partial \xi}+\overline{\zeta}_x\frac{\partial \overline{u}}{\partial \zeta}\Big)+\overline{w}\overline{\zeta}_z\frac{\partial \overline{u}}{\partial \zeta} &= -\Big(\frac{\partial \overline{p}}{\partial \xi}+\overline{\zeta}_x\frac{\partial \overline{p}}{\partial \zeta}\Big) \\
&\quad -\Big(\frac{\partial \overline{\sigma}_{11}}{\partial \xi}+\overline{\zeta}_x\frac{\partial \overline{\sigma}_{11}}{\partial \zeta}\Big)-\overline{\zeta}_z\frac{\partial \overline{\sigma}_{13}}{\partial \zeta}+Tub., \qquad (135)\\
(\overline{u}-c)\Big(\frac{\partial \overline{w}}{\partial \xi}+\overline{\zeta}_x\frac{\partial \overline{w}}{\partial \zeta}\Big)+\overline{w}\zeta_z\frac{\partial \overline{w}}{\partial \zeta} &= -\overline{\zeta}_z\frac{\partial \overline{p}}{\partial \zeta} \\
&\quad -\Big(\frac{\partial \overline{\sigma}_{31}}{\partial \xi}+\overline{\zeta}_x\frac{\partial \overline{\sigma}_{31}}{\partial \zeta}\Big)-\overline{\zeta}_z\frac{\partial \overline{\sigma}_{33}}{\partial \zeta}+Tub., \qquad (136)\\
\frac{\partial \overline{u}}{\partial \xi}+\overline{\zeta}_x\frac{\partial \overline{u}}{\partial \zeta}+\overline{\zeta}_z\frac{\partial \overline{w}}{\partial \zeta} &= 0, \qquad (137)
\end{aligned}
$$

where $\sigma_{jk}=-\nu(\partial u_j/\partial x_k+\partial u_k/\partial x_j)$ is the viscous stress and 'Tub' represents the neglected terms associated with the correlation between turbulent velocity fluctuations.

Dividing (135) by $\overline{\zeta}_z$ and applying the triple decomposition to all of the terms, we can extract the streamwise momentum equation for the wave-coherent velocity

$$
\begin{aligned}
(\langle u\rangle-c)\frac{\partial \widetilde{u}}{\partial \xi}+(\widetilde{w}+(\langle u\rangle-c)g\widetilde{\eta}_\xi)\frac{\mathrm{d}\langle u\rangle}{\mathrm{d}\zeta}+\frac{\partial \widetilde{p}}{\partial \xi} &= -\frac{\partial \widetilde{\sigma}_{11}}{\partial \xi} \\
&\quad -g\widetilde{\eta}_\xi\frac{\mathrm{d}\langle \sigma_{11}\rangle}{\mathrm{d}\zeta}-\frac{\partial \widetilde{\sigma}_{13}}{\partial \zeta}+O((ak)^2)+n.l.f. \qquad (138)
\end{aligned}
$$

where $O((ak)^2)$ denotes the neglected second and higher -order terms, and the '*n.l.f.*' represents the neglected nonlinear forcing, i.e. the correlation between turbulent velocity fluctuations and the correlation between wave-induced velocity components.

By linearising the viscous stresses $\overline{\sigma}_{11}$ and $\overline{\sigma}_{13}$ as

$$\widetilde{\sigma}_{11} = -2\nu(\frac{\partial \widetilde{u}}{\partial \xi} + g\widetilde{\eta}_{\xi}\frac{\mathrm{d}\langle u\rangle}{\mathrm{d}\zeta}) + O((ak)^2) = 2\nu\frac{\partial \widetilde{w}}{\partial \zeta} + O((ak)^2), \tag{139}$$

$$\langle \sigma_{11}\rangle = 0 + O((ak)^2), \tag{140}$$

$$\widetilde{\sigma}_{13} = -\nu(\frac{\partial \widetilde{u}}{\partial \zeta} + \frac{\partial \widetilde{w}}{\partial \xi} + g_{\zeta}\widetilde{\eta}\frac{\mathrm{d}\langle u\rangle}{\mathrm{d}\zeta}) + O((ak)^2), \tag{141}$$

where $\overline{\zeta}_z = 1 + g_{\zeta}\widetilde{\eta} + O((ak)^2)$ has been applied, we can express (138) as

$$\begin{aligned}(\langle u\rangle - c)\frac{\partial \widetilde{u}}{\partial \xi} + (\widetilde{w} + (\langle u\rangle - c)g\widetilde{\eta}_{\xi})\frac{\mathrm{d}\langle u\rangle}{\mathrm{d}\zeta} + \frac{\partial \widetilde{p}}{\partial \xi} &= \nu\Big(\frac{\partial^2 \widetilde{u}}{\partial \zeta^2} - \frac{\partial^2 \widetilde{w}}{\partial \xi \partial \zeta}\Big) \\ &+ \frac{\mathrm{d}}{\mathrm{d}\zeta}\Big(g_{\zeta}\frac{\mathrm{d}\langle u\rangle}{\mathrm{d}\zeta}\Big)\widetilde{\eta} + O((ak)^2) + n.l.f. \end{aligned} \tag{142}$$

Dividing (136) by $\overline{\zeta}_z$ and applying the triple decomposition to all of the quantities, we can extract the vertical momentum equation for the wave-coherent velocity

$$(\langle u\rangle - c)\frac{\partial \widetilde{w}}{\partial \xi} + \frac{\partial \widetilde{p}}{\partial \zeta} = -\frac{\partial \widetilde{\sigma}_{31}}{\partial \xi} - g\widetilde{\eta}_{\xi}\frac{\mathrm{d}\langle \sigma_{31}\rangle}{\mathrm{d}\zeta} - \frac{\partial \widetilde{\sigma}_{33}}{\partial \zeta} + O((ak)^2) + n.l.f. \tag{143}$$

By linearising the viscous stresses $\overline{\sigma}_{31}$ and $\overline{\sigma}_{33}$ as

$$\widetilde{\sigma}_{31} = -\nu\frac{\partial \widetilde{u}}{\partial \zeta} - \nu\frac{\partial \widetilde{w}}{\partial \xi} - \nu g_{\zeta}\widetilde{\eta}\frac{\mathrm{d}\langle u\rangle}{\mathrm{d}\zeta}) + O((ak)^2), \tag{144}$$

$$\langle \sigma_{31}\rangle = -\nu\frac{\mathrm{d}\langle u\rangle}{\mathrm{d}\zeta} + O((ak)^2), \tag{145}$$

$$\widetilde{\sigma}_{33} = -2\nu\frac{\partial \widetilde{w}}{\partial \zeta} + O((ak)^2), \tag{146}$$

we can express (143) as

$$(\langle u\rangle - c)\frac{\partial \widetilde{w}}{\partial \xi} + \frac{\partial \widetilde{p}}{\partial \zeta} = \nu\Big(\frac{\partial^2 \widetilde{w}}{\partial \xi^2} + \frac{\partial^2 \widetilde{w}}{\partial \zeta^2}\Big) + O((ak)^2) + n.l.f. \tag{147}$$

where $g_\zeta \langle u\rangle_\zeta + g\mathrm{d}\langle u\rangle_\zeta/\mathrm{d}\zeta = \mathrm{d}(g\langle u\rangle_\zeta)/d\zeta$ has been applied.

Similarly, dividing (137) by $\overline{\zeta}_z$ and applying the triple decomposition to all of the terms, we can extract the continuity equation for the wave-coherent velocity

$$\frac{\partial \widetilde{u}}{\partial \xi} + g\widetilde{\eta}_\xi \frac{\mathrm{d}\langle u\rangle}{\mathrm{d}\zeta} + \frac{\partial \widetilde{w}}{\partial \zeta} = 0 + O((ak)^2). \tag{148}$$

Equations (142), (147), and (148) are the same as the linearised equations derived from the strongly conservative LES equations, i.e. (24)–(26).

E Equations for in-phase and out-of-phase wave-induced pressure

In this section, we obtain the leading-order contributions to the in-phase and out-of-phase wave-induced pressure $\widetilde{p}$ using the linearised vertical momentum equation for wave-induced airflow, i.e. (25). The integration of (25) gives the expression for $\widetilde{p}$ at height ζ

$$\begin{aligned}\widehat{p}|_{\zeta=\lambda} - \widehat{p}|_{\zeta} = {} & \underbrace{\int_\zeta^\lambda -(\langle u\rangle - c)\frac{\partial \widetilde{w}}{\partial \xi}\mathrm{d}\zeta}_{\mathcal{A}} \\ & + \underbrace{\int_\zeta^\lambda \nu(\frac{\partial^2 \widetilde{w}}{\partial \xi^2} + \frac{\partial^2 \widetilde{w}}{\partial \zeta^2})\mathrm{d}\zeta}_{\mathcal{V}} + \underbrace{\int_\zeta^\lambda (-\frac{\partial \widetilde{\tau}_{3j}}{\partial \xi_j} - \frac{\partial \widetilde{\tau}^w_{3j}}{\partial \xi_j})\mathrm{d}\zeta}_{\mathcal{N}} + O((ak)^2),\end{aligned} \tag{149}$$

where $\mathcal{A}$, $\mathcal{V}$, and $\mathcal{N}$ represent the contributions from the advection by $\widetilde{w}$, viscous stress, and nonlinear forcing, respectively. Equation (149) indicates that $\widetilde{p}$ results from the integration of all of the stress terms in the wave boundary layer. Because the nonlinear forcing and viscous stress are important only in the vicinity of the wave surface and thus have a very thin integration thickness, $\mathcal{V}$ and $\mathcal{N}$ have the secondary effects compared with $\mathcal{A}$. Then we obtain the leading order contribution to the generation of $\widetilde{p}$ as

$$\widehat{p}|_{\zeta} \approx \int_{\zeta}^{\lambda} -(\langle u \rangle - c)\frac{\partial \widetilde{w}}{\partial \xi}\mathrm{d}\zeta, \tag{150}$$

where $\widetilde{p}|_{\zeta=\lambda} = 0$ has been applied. Taking the imaginary and real parts of (150) with respect to $\widetilde{p}$, we obtain the leading order contribution to the in-phase pressure $\mathrm{Im}[\widehat{p}]$,

$$\mathrm{Im}[\widehat{p}]\big|_{\zeta} \approx \int_{\zeta}^{\lambda} k(\langle u \rangle - c)\,\mathrm{Re}[\widehat{w}]\mathrm{d}\zeta, \tag{151}$$

and the out-of-phase pressure $\mathrm{Re}[\widehat{p}]$,

$$\mathrm{Re}[\widehat{p}]\big|_{\zeta} \approx \int_{\zeta}^{\lambda} -k(\langle u \rangle - c)\,\mathrm{Im}[\widehat{w}]\mathrm{d}\zeta. \tag{152}$$

In § 2, (151) and (152) are used to investigate the physical processes associated with $\mathrm{Im}[\widehat{p}]$ and $\mathrm{Re}[\widehat{p}]$, respectively.

F Derivation of orthogonal linearised equations

In this appendix, we derive the viscous linear model for the fast wave-induced airflow based on the conformal mapping for the coordinates,

$$\xi = x - \mathrm{i}a\mathrm{e}^{-kz}\mathrm{e}^{\mathrm{i}kx}, \qquad \psi = y, \qquad \zeta = z - a\mathrm{e}^{-kz}\mathrm{e}^{\mathrm{i}kx}. \tag{153}$$

The phase-averaged LES equations in the wave following frame are (e.g., Sullivan *et al.*, 2000)

$$\begin{aligned}
(\overline{U}_j - c)\frac{\partial \overline{u}_k}{\partial \xi_j} + \frac{1}{\rho_a}\frac{\partial}{\partial \xi_j}\Big(\frac{\overline{p}}{J}\frac{\partial \xi_j}{x_k}\Big) &= \nu\Big(\frac{\partial^2 \overline{u}_k}{\partial \xi^2} + \frac{\partial^2 \overline{u}_k}{\partial \zeta^2}\Big) + Turb., && (154)\\
\frac{\partial \overline{U}_k}{\partial \xi_k} &= 0, && (155)
\end{aligned}$$

where '$Turb.$' denotes the resolved and SGS turbulent stresses, 'J' is the determinant of transformation Jacobian matrix, and $U_k = 1/J \cdot u_j \cdot \partial\xi_k/\partial\xi_j$ is the contravariant flux velocity.

By linearising (154) and (155) about the mean wind profile, we can extract the equations for the wave-coherent air motion as

$$\begin{aligned}
(\langle U\rangle - c)\frac{\partial \widetilde{u}}{\partial \xi_j} + \widetilde{W}\frac{\mathrm{d}\langle u\rangle}{\mathrm{d}\zeta} + \frac{1}{\rho_a}\frac{\partial \widetilde{p}}{\partial \xi_j}\Big\langle\frac{1}{J}\frac{\partial \xi_j}{\partial x}\Big\rangle &= \nu\Big(\frac{\partial^2 \widetilde{u}}{\partial \xi^2} + \frac{\partial^2 \widetilde{u}}{\partial \zeta^2}\Big) + n.l.f., && (156)\\
(\langle U\rangle - c)\frac{\partial \widetilde{w}}{\partial \xi_j} + \widetilde{W}\frac{\mathrm{d}\langle w\rangle}{\mathrm{d}\zeta} + \frac{1}{\rho_a}\frac{\partial \widetilde{p}}{\partial \xi_j}\Big\langle\frac{1}{J}\frac{\partial \xi_j}{\partial z}\Big\rangle &= \nu\Big(\frac{\partial^2 \widetilde{w}}{\partial \xi^2} + \frac{\partial^2 \widetilde{w}}{\partial \zeta^2}\Big) + n.l.f., && (157)\\
\frac{\partial \widetilde{U}}{\partial \xi} + \frac{\partial \widetilde{W}}{\partial \zeta} &= 0, && (158)
\end{aligned}$$

where '$n.l.f.$' denotes the neglected nonlinear forcing, i.e. the wave-induced turbulent stress and the wave-induced fluctuations of the correlations between the components of the wave-induced velocity, and $\partial(1/J \cdot \partial\xi_j/\partial x_k)/\partial\xi_j = 0$ has been applied.

To simplify (156)–(158), we can first express the $(\xi,\, \psi)$ plane averaged contravariant flux velocity $\langle U\rangle$ and $\langle W\rangle$ using the Cartesian quantities as

$$\langle U\rangle = \langle u\rangle + O((ak)^2), \qquad \langle W\rangle = \langle w\rangle + O((ak)^2), \tag{159}$$

where '$O((ak)^2)$' denotes the neglected second- and higher- order terms.

Then, we can express the wave-induced contravariant flux velocity $\widetilde{U}$ and $\widetilde{W}$ using the Cartesian quantities as

$$\widetilde{U} = \widetilde{u}\Big\langle \frac{1}{J}\frac{\partial\xi}{\partial x}\Big\rangle + \langle u\rangle \widetilde{\frac{1}{J}\frac{\partial\xi}{\partial x}} + \widetilde{w}\Big\langle \frac{1}{J}\frac{\partial\xi}{\partial z}\Big\rangle + \langle w\rangle \widetilde{\frac{1}{J}\frac{\partial\xi}{\partial z}}, \tag{160}$$

$$\widetilde{W} = \widetilde{u}\Big\langle \frac{1}{J}\frac{\partial\zeta}{\partial x}\Big\rangle + \langle u\rangle \widetilde{\frac{1}{J}\frac{\partial\zeta}{\partial x}} + \widetilde{w}\Big\langle \frac{1}{J}\frac{\partial\zeta}{\partial z}\Big\rangle + \langle w\rangle \widetilde{\frac{1}{J}\frac{\partial\zeta}{\partial z}}. \tag{161}$$

With (160)–(161), the continuity equation (158) can be linearised as

$$\frac{\partial\widetilde{u}}{\partial\xi} + \frac{\partial\widetilde{w}}{\partial\zeta} = \frac{\mathrm{d}\langle u\rangle}{\mathrm{d}\zeta}\mathrm{e}^{-k\zeta}\widetilde{\eta}_\xi + O((ak)^2), \tag{162}$$

where $\partial(1/J \cdot \partial\xi_j/\partial x_k)/\partial\xi_j = 0$ and $\widetilde{\eta} = a\mathrm{e}^{\mathrm{i}kx}$ have been applied.

The last step in simplifying (156)–(158) is to express the terms associated with the wave-induced pressure $\widetilde{p}$ as

$$\frac{\partial\widetilde{p}}{\partial\xi_j}\Big\langle \frac{1}{J}\frac{\partial\xi_j}{\partial x}\Big\rangle = \frac{\partial\widetilde{p}}{\partial\xi} + O((ak)^2), \qquad \frac{\partial\widetilde{p}}{\partial\xi_j}\Big\langle \frac{1}{J}\frac{\partial\xi_j}{\partial z}\Big\rangle = \frac{\partial\widetilde{p}}{\partial\zeta} + O((ak)^2). \tag{163}$$

With (159)–(163), the equations for wave-coherent air motion (156)–(158) become

$$\begin{aligned}(\langle u\rangle - c)\frac{\partial \widetilde{u}}{\partial \xi} + (\widetilde{w} - (\langle u\rangle - c)\mathrm{e}^{-\mathrm{k}\zeta}\widetilde{\eta}_\xi)\frac{\mathrm{d}\langle u\rangle}{\mathrm{d}\zeta} + \frac{1}{\rho_a}\frac{\partial \widetilde{p}}{\partial \xi} &= \\ \nu\Big(\frac{\partial^2 \widetilde{u}}{\partial \xi^2} + \frac{\partial^2 \widetilde{u}}{\partial \zeta^2}\Big) &+ O((ak)^2) + n.l.f., \qquad (164)\\ (\langle u\rangle - c)\frac{\partial \widetilde{w}}{\partial \xi} + \frac{1}{\rho_a}\frac{\partial \widetilde{p}}{\partial \zeta} = \nu\Big(\frac{\partial^2 \widetilde{w}}{\partial \xi^2} + \frac{\partial^2 \widetilde{w}}{\partial \zeta^2}\Big) &+ O((ak)^2) + n.l.f., \qquad (165)\\ \frac{\partial \widetilde{u}}{\partial \xi} + \frac{\partial \widetilde{w}}{\partial \zeta} = \frac{\mathrm{d}\langle u\rangle}{\mathrm{d}\zeta}\mathrm{e}^{-\mathrm{k}\zeta}\widetilde{\eta}_\xi &+ O((ak)^2). \qquad (166)\end{aligned}$$